THESIS

DEVELOPMENT, FABRICATION AND TESTING OF THE SCANNING AND CALIBRATION SUBSYSTEMS FOR THE TROPOSPHERIC WATER AND CLOUD ICE INSTRUMENT FOR 6U CUBESATS

Submitted by

Braxton Kilmer

Department of Electrical and Computer Engineering

In partial fulfillment of the requirements

For the Degree of Master of Science

Colorado State University

Fort Collins, Colorado

Spring 2019

Master's Committee:

Advisor: Steven C. Reising

V. Chandrasekar
Christine Chiu

ABSTRACT

DEVELOPMENT, FABRICATION AND TESTING OF THE SCANNING AND CALIBRATION SUBSYSTEMS FOR THE TROPOSPHERIC WATER AND CLOUD ICE INSTRUMENT FOR 6U CUBESATS

Global observations of ice cloud particle size and ice water content are needed to improve weather forecasting and climate prediction. The interaction between ice particles and upwelling radiation at sub-millimeter-wavelengths strongly depends on ice particle size and observation frequency. Sub-millimeter-wavelength radiometry provides the capability to fill an observational gap by allowing the detection and sizing of ice particles with diameters between 50 μm and 1 mm. Atmospheric temperature and water vapor profiles can also be yielded at sub-millimeter-wavelengths.

The Tropospheric Water and Cloud ICE (TWICE) millimeter- and sub-millimeter-wave radiometer instrument is currently under development for 6U CubeSats in a joint effort among Colorado State University (lead), NASA/Caltech Jet Propulsion Laboratory, and Northrop Grumman Corporation. The TWICE radiometer instrument is designed to provide global measurements of cloud ice, as well as temperature and water vapor profiles in the upper troposphere/lower stratosphere. The TWICE radiometer instrument has 16 frequency channels near 118 GHz for temperature profiling, near 183 and 380 GHz for water vapor profiling, and centered on 240, 310, 670, and 850 GHz quasi-window channels for ice particle sizing.

The TWICE radiometer instrument uses a conical scanning strategy to observe the Earth's atmosphere and surface. The complete TWICE scan is designed to sweep out a 200° arc once per second, and the scan direction reverses every second interval. The TWICE scanning system is designed to fit inside a 6U CubeSat in terms of volume and mass, while meeting the torque and acceleration requirements of the scanning radiometer instrument. A stepper motor and gearbox mechanism were selected for the TWICE scanning system. Precisely placed position sensors, in combination with stepper motor step calculation, provide sufficient angular position data, in place of a traditional encoder. The TWICE scanning system has been tested, and angular position analysis has been performed.

The TWICE instrument performs end-to-end, two-point radiometric calibration by observing an ambient temperature calibration target and cosmic microwave background reflector during each conical scan. The ambient calibration target is designed to enable simultaneous blackbody measurements at all TWICE millimeter- and sub-millimeter-wave channels. Calibration target design parameters, including size, geometry, thermal and electromagnetic properties, have been chosen to meet the performance requirements of the ambient target and to minimize temperature gradients. Reflection coefficient measurements have been performed in the millimeter to sub-millimeter wavelength range of the TWICE channels. Thermal analysis of the ambient calibration target has been performed using ANSYS software. The resulting ambient calibration target design meets functional requirements as well as size and weight constraints to fit into a 6U CubeSat.

The TWICE radiometer instrument employs several subsystems that need to communicate during nominal operation. An interface board was designed to meet the communication needs of and provide power regulation for the various interfacing subsystems of the instrument. The interface board is responsible for controlling the scanning subsystem of the radiometer instrument, performing temperature data acquisition for the radiometer instrument front end and the ambient calibration target, routing signals to and from the control and data handling subsystem of the radiometer instrument, and regulating power to the on-board computer. The interface board has been manufactured and its performance has been tested.

ACKNOWLEDMENTS

I would like to thank Prof. Steven Reising for guiding and supporting my research and Master's Thesis. Additionally, I would like to thank Prof. V. Chandrasekar and Prof. Christine Chiu for their support with my research and education, and for serving on my graduate committee.

I would also like to thank Dr. Yuriy Goncharenko, Dr. Mehmet Ogut and Jared McKneely for their past and continued support with my research and professional success. Furthermore, I would like to thank the past and current members of the Microwave Systems Laboratory at Colorado State University (CSU) including Renish Tomas and Samantha Williams.

I would like to extend thanks to all of the members of the NASA TWICE IIP-13 project at the NASA/Caltech Jet Propulsion Laboratory (JPL) and the Northrop Grumman Corporation (NGC). I would like to thank Dr. Pekka Kangaslahti, Dr. Erich Schlecht, Dr. Anders Skalare, Dr. Richard Cofield, and Joelle Cooperrider at JPL, as well as Dr. William Deal and Dr. Alex Zamora at NGC.

Additionally, I would like to extend thanks to all of the members of the NASA TEMPEST-D Earth Venture project including Dr. Wesley Berg, Prof. Christian Kummerow, and Ann Bathchelor at CSU, as well as Dr. Todd Gaier, Dr. Sharmila Padmanabhan, Dr. Shannon Brown and Dr. Boon Lim at JPL, and Matt Pallas at Blue Canyon Technologies for their support in my research and education.

Finally, I owe my deepest gratitude to my friends and family who have endlessly supported my efforts at CSU and who have encouraged my passion for science and technology.

DEDICATION

To my friends and family for their love and support

TABLE OF CONTENTS

LIST OF FIGURES

Chapter I Introduction

1.1 Scientific Motivation

The water and energy cycle of the Earth's atmosphere play a vital role in the Earth's climate. Research of these critical processes is needed to better understand how a changing climate will affect life on Earth. Specifically, data regarding water vapor content and cloud ice are sought out at a global scale [1].Water vapor is a strong contributor to the greenhouse effect in the Earth's atmosphere and its concentration is largely modulated by temperature. Other temperature modulating constituents in the Earth's atmosphere can amplify the role that water vapor plays in the greenhouse effect [2].

The hydrological cycle has been shown to also have a dependence on the development of high altitude ice particles. Ice clouds located in the upper troposphere and lower stratosphere regulate shortwave and longwave energy flow through the Earth's atmosphere by way of a greenhouse-versus-albedo effect [3]. High altitude ice clouds reflect shortwave radiation back into space while also trapping longwave radiation inside of the Earth's atmosphere. This balance is largely determined by the microphysical properties of the ice clouds, including crystal shape and optical thickness. Models such as the global circulation model help to determine a consensus regarding cloud fraction and precipitation. However, they still contain a fair degree of uncertainty in the measurement of ice water content and ice water path [4]. The study of the microphysical processes that dictates the behavior of ice clouds and other hydrological systems can be achieved with advent of millimeter- and sub-millimeter-wave (MSMW) radiometry.

Up until recently, the use of MSMW has been limited to the current state of technology. A lack of spaceborne sensor components and instruments that can perform scientific measurements at the MSMW range has resulted in missed opportunities to study atmospheric phenomenon at these frequencies [5]. MSMW radiometer instruments can be miniaturized while still maintaining reliable amplification with the advent of indium phosphide (InP) high electron mobility transistors (HEMT) technology [6], [7]. These miniaturized MSMW instruments allow for the ability to perform Earth science at these frequency bands on a CubeSat platform. More specifically, smaller MSMW instruments allow for the development of Earth science missions on SmallSats, reducing the cost and risk of traditional Earth observing satellites.

The Tropospheric Water and Cloud ICE (TWICE) instrument utilizes InP HEMT to perform spaceborne measurements of the Earth's atmosphere. The TWICE radiometer frequencies are placed near atmospheric absorption lines at 118 GHz for temperature sounding, and 183 GHz and 380 GHz for water vapor sounding. Four direct detection receivers centered at 240 GHz, 310 GHz, 670 GHz, and 850 GHz will be used to observe ice particle size and ice water content. The TWICE instrument is designed to meet the specific power, mass, and size constraints needed to operate on a 6U CubeSat.

1.2 Overview of CubeSats

TWICE serves as a platform for Earth observing MSMW radiometer technology can be demonstrated. SmallSats, or more specifically CubeSats like that of TWICE, provide alternatives to larger traditional satellites. Significantly reduced size, mass, and power consumption allow for cheaper and timelier spaceborne missions, aiding in both scientific and technological advancement [8]. CubeSats were developed by Robert Twiggs and Jordi Puig-Suari in 1999 [9]. These satellites were designed to fit within the standardized shape and size of a Poly-Picosatellite Orbital Deployer (P-POD), a launch interface developed at California Polytechnic State University [10]. Each standardized cube, or 1U, of a CubeSat is approximately 10 cm x 10 cm x

11 cm which allows up to 3 to fit into a P-POD. The dimensions of a P-POD are approximately 10 cm x 10 cm x 34 cm, a total of 3U [8].

Figure 1: A picture of the Radiometer Assessment using Vertically Aligned Nanotubes (RAVAN), a 3U CubeSat [11]**.**

The concept of a Cubesat was originally proposed to meet an educational need for students. The idea being that students would be able to design, develop, test, and even deploy satellites that at a very low cost and risk [10]. However, CubeSats have quickly become a platform for scientific and high-tech inquiry. CubeSats have fallen within the scope of federal space and defense agencies like that of NASA or the U.S. Department of Defense (DoD) [8]. For instance, recent missions like the Temporal Experiment for Storms and Tropical Systems Technology –

Demonstration (TEMPEST-D) developed under the purview of NASA's Earth Science Technology Office lead by principal investigator Prof. Steven C. Reising, allows new technology to be tested on a spaceborne mission. A fully realized TEMPEST mission would provide the first ever temporally – resolved observations of cloud and precipitation processes at a global scale [12].

Figure 2: A picture of a 6U CubeSat deployment from a NanoRacks dispenser [13].

CubeSats also differ from more traditional satellites by taking flight in a unconventional way. Due to their small size and low mass, several CubeSats can be launched at once, often hitching a ride on many different types of rockets and payloads like a resupply mission to the International Space Station (ISS), for instance. TEMPEST-D is an example of such a scenario [14].

There are several different ways that a CubeSat can make it to space. A common way to support a CubeSat mission is with the NASA's CubeSat Launch Initiative (CSLI). CSLI provides an attractive option to orbit as NASA will both provide a launch vehicle and cover the cost of launch in exchange for a scientific report of the CubeSat mission (this option was utilized by TEMPEST-D). CSLI provides 5 different mission models to support a CubeSat mission. Each of these different deployment models are described in detail in [8].

Figure 3: A picture of CubeRRT (left) and TEMPEST-D (right) immediately after deployment from a NanoRacks deployer [15].

1.3 Limitations of CubeSats

CubeSats, in general, have stringent standards, meaning that the instruments they carry must adhere to the limits of the platform. As previously mentioned, the envelope and mass of a CubeSat is strictly defined. These standardized definitions are what allow the CubeSat platform to operate with such low cost and risk; making them both highly desirable and highly available. Due to the lack of real-estate, power sources, like solar panels, are also restricted, meaning power consumption of the various subsystems of an on-board instrument must be meticulously determined.

As an example, consider the TWICE 6U CubeSat instrument. By virtue of utilizing a 6U CubeSat platform, the TWICE instrument, in addition to spacecraft avionics, and power sources like solar panels, must fit within an envelope of 12 cm x 24 cm x 36 cm, and must not exceed a mass of 12 kg. This can pose some significant design challenges in regard to placement and orientation of the radiometer instrument, the location of the calibration subsystem, and operation of any moving parts. In this work, these challenges will be identified and discussed in detail.

1.3 Objectives of IIP-13

IIP-13 was established with a set of goals that meet the needs of current Earth science issues. ESTO states that selected IIP projects must research, develop, and demonstrate new measurement technologies. Each project must provide work to enable new Earth observation measurements as well as reduce size, cost, risk, and development time of Earth observing instruments. To meet these goals, the TWICE project will develop, fabricate, and test MSMW radiometer instruments for atmospheric measurement. TWICE performs global observations at a variety of local times while also reducing the size, mass, and power consumption of MSMW technology [16]. The TWICE instrument will help to advance the technology readiness level (TRL) of the new and existing technology, making them available for spaceborne applications.

NASA's Earth Science Technology Office (ESTO), TWICE was selected in 2013 as a part of an Instrument Incubator Program (IIP-13). The TWICE project is led by Principal Investigator Prof. Steven Reising at the Colorado State University (CSU) Microwave Systems Laboratory (MSL) along with Co-Investigators Dr. Pekka Kangaslahti at the NASA/Caltech Jet Propulsion Laboratory (JPL) and Dr. William Deal at the Northrop Grumman Corporation (NGC).

1.4 Thesis Description and Organization

Chapter II will discuss the fundamental principles of passive microwave and MSMW radiometer including Planck's law and blackbody theory. This chapter will also discuss the fundamental concepts of atmospheric radiometry in the microwave and MSMW frequency range. The topics of atmospheric sounding and scattering will be introduced.

Chapter III will discuss TWICE scanning strategy, including the structural design of the TWICE instrument and its 6U CubeSat chassis. Furthermore, different scanning techniques will be investigated. Lastly, this section will include a study of the TWICE scanning requirements and a characterization of the TWICE acceleration and inertial properties.

Chapter IV will include a detailed discussion of the design and testing of the TWICE scanning system. This chapter will include the selection process of the motor and gearbox scanning mechanism, as well as the efforts taken to interface the two parts of the scanning mechanism. This chapter will also include positon testing and analysis of the TWICE scanning system.

Chapter V is a short review of common radiometers and their calibration techniques. Specifically, Dicke switching and noise injection radiometers will be discussed including their calibration mechanisms and their general resolution. Total power radiometers and their calibration systems and associated resolution will also be covered. A comparison between direct detection and heterodyne radiometers will be presented in this chapter last.

Chapter VI will provide a detailed discussion of the design and selection process of the TWICE ambient calibration target. Material return loss testing will be covered, as well as material thermal simulation and thermal cycling testing. Ambient calibration target thermal monitoring systems are discussed, as well as placement and deployment.

Chapter VII will detail the design and selection of the TWICE interface board. Every interface board component is discussed in detail. Resolution calculation is presented that is used to select an appropriate ADC for thermistor acquisition.

Chapter II Passive Microwave Remote Sensing

2.1 Blackbody Theory

All forms of matter above a temperature of absolute zero (0 K) radiate energy. This fundamental principal is the basis of radiometry. Radiometry is the study and measurement of the energy, or power, radiated by a source over a particular band of the electromagnetic (EM) spectrum [17]. The amount of power radiated by a source can be quantified by an equation known as Planck's law. Simply put, Planck's law describes the density and direction of the power being radiated by a source, as well as over which frequencies the radiated power is most concentrated. Planck's law is shown in Equation II.1.

$$B_\nu(\nu, T) = \frac{2h\nu^3}{c^2}\frac{1}{e^{\frac{h\nu}{k_B T}} - 1} \tag{II.1}$$

Where h is the Planck constant (J•s), c is the speed of light in vacuum (m/s), k_b is the Boltzmann constant (J/K), T is temperature (K), and ν is frequency (Hz) [18]. Equation II.1 can be expressed in several different ways, for example in terms of wavelength or wavenumber. Different variations of Plank's law are often used to accommodate the nomenclature of different areas in radiometry. In any formulation, Plank's law gives a measure of how much power is being produced in terms of spectral radiance. The units of spectral radiance differ depending on how the quantity is defined. For example, if Planck's law is written in terms of frequency, like in Equation II.1, the SI units are W/sr/m^2/Hz, or if in terms of wavelength they are W/sr/m^2/m. The concept of radiance is a critical aspect of radiometry for it quantifies the amount of detectible power radiating from a source. In other words, radiance not only measures how much power is being radiated by a source but also measures the density and direction of the power being radiated [17].

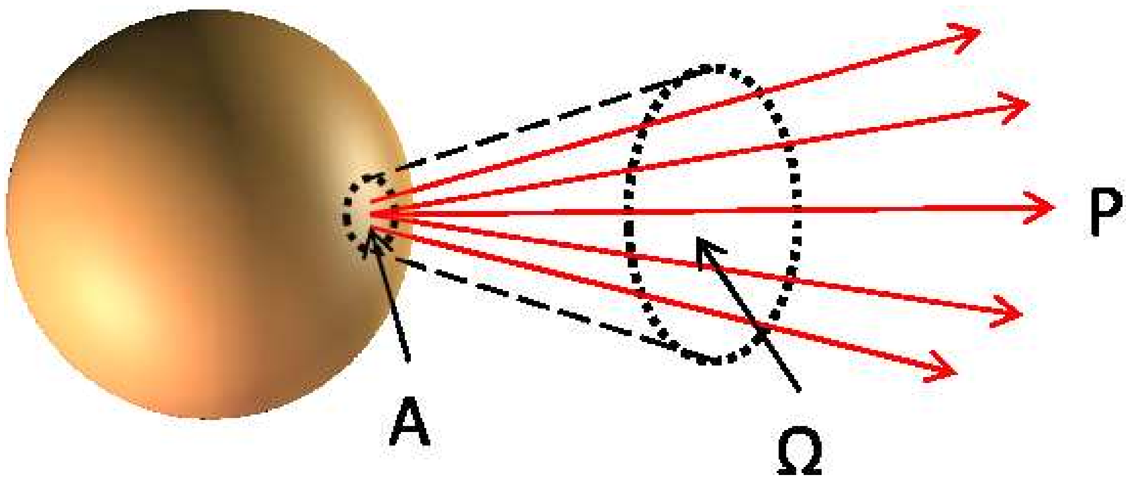

Figure 4: An illustration of how radiance is defined.

Consider an illustration of this concept in Figure 4, where the source is an ideal radiator in the shape of a sphere. Figure 4 illustrates how power (P) radiated from area (A), through solid angle (Ω) defines the radiance (R) for a particular portion of a radiating body, $R = P/(A\Omega)$.The radiance of a source can be increased by increasing the amount of power radiated, or by restricting the area and solid angle through which it radiates. The converse of the previous statement is also true by similar logic. It is also important to note that radiance is conserved along its path of propagation [17]. This makes sense considering that, aside from time and space, radiance is measure of energy, which is a conserved quantity. Radiance is a useful concept to understand when working with radiometers for it gives one the ability to quantify the power received by a radiometer within a footprint or snapshot.

It is important to note the dependency of Planck's law on the temperature of the radiating source. An illustration of this dependency is shown in Figure 5. Note that as temperature increases, so too does the magnitude of the spectral radiance. A higher temperature also shifts the frequency at which the magnitude of the spectral radiance is the largest. As the temperature of the radiating body decreases, the total amount of energy it radiates also decreases.

In essence, a passive radiometer detects the energy radiated by a source and coverts that detected energy into a measureable output signal. A fundamental understanding of Planck's law is important when determining a relationship between the signal that a radiometer outputs and the radiated energy that a radiometer detects. For instance, if a radiometer is looking at very hot object, the signal that is produced at the output will be relatively large. A more detailed description of how detected energy is propagated through a radiometer system will be described in a later section.

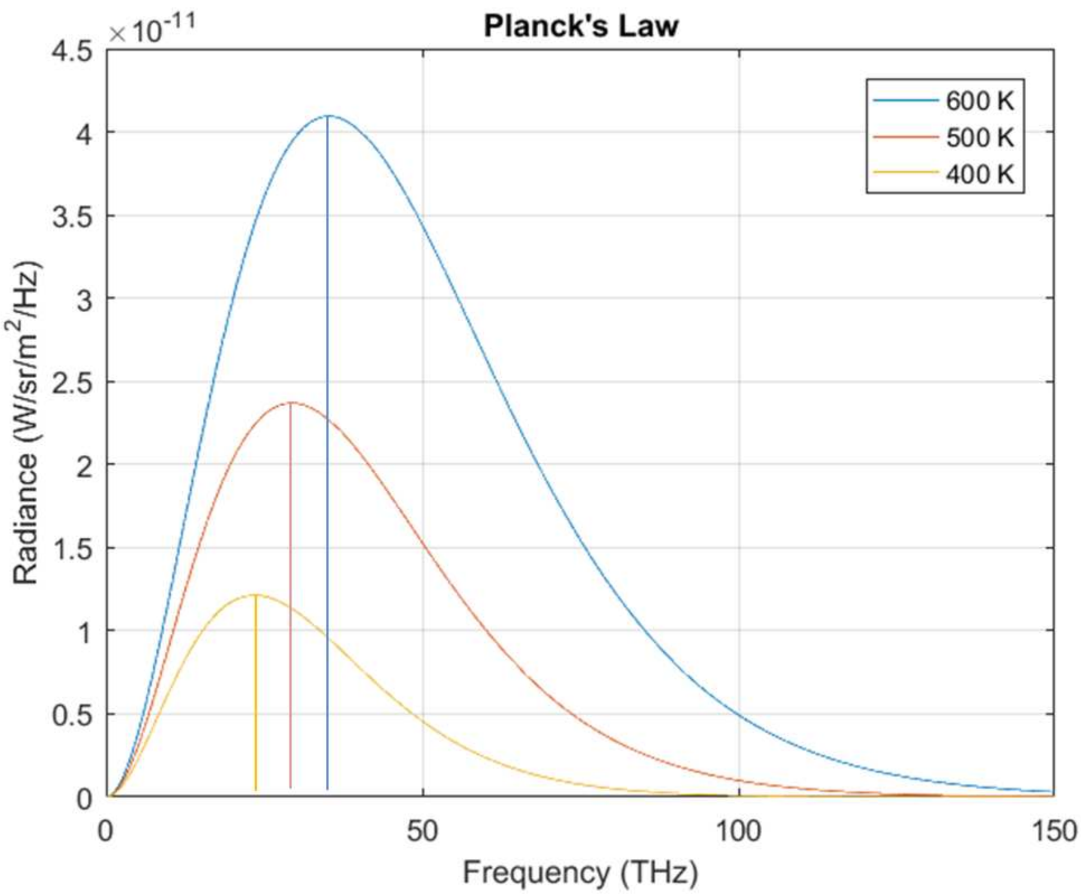

Figure 5: A plot illustrating the dependency of temperature and frequency on the magnitude and shape of spectral radiance as defined by Planck's law.

2.2 Emission, Absorption, and Brightness Temperature

In a perfect, theoretical universe, a body with a temperature above absolute zero will radiate energy with 100% efficiency at all temperatures and frequencies. A body that holds these unique and theoretical properties is known as a blackbody [18]. Blackbodies are also able to absorb any arbitrary amount of radiated energy with 100% efficiency, meaning that no amount of incident energy will be reflected. To this end, if a person were to observe a perfect blackbody within the visible spectrum they would only see a black object, void of all visible reflections. It is this concept that gives blackbodies their name. However, objects in the real world do not actually emit radiation with 100% efficiency. Real bodies emit and absorb radiation with varying amounts of efficiency that is highly dependent on both the physical temperature of the body and the frequency of the radiation being emitted or absorbed. It can be noted though that there is another unique type of body known as a grey body. Grey bodies absorb and radiate energy in an identical way to a blackbody; however, they do so with less than 100% efficiency. The ability, or efficiency, of a radiating body to emit radiation according to its physical temperature is determined by a value known as emissivity, ε. In general, emissivity is defined as

$$\varepsilon = \frac{I(\nu, T_{app})}{B(\nu, T_{phys})} \tag{II.2}$$

Where $I(\nu, T_{app})$ is the radiance of an arbitrary radiating body at some apparent temperature T_{app} and frequency ν, and $B(\nu, T_{phys})$ is the radiance of a perfect blackbody, as shown in Equation II.1, at the at a physical temperature T_{phys} and frequency ν. Emissivity is given as a value between 0 and 1, where 0 describes an object that is a perfect reflector and 1 describes a perfect emitter.

Another unique characteristic of emissivity is that it also describes an objects ability to absorb radiation. At a very high, conceptual level it is well known that energy cannot be created or destroyed. This concept plays an important part in the radiation of energy from a source. Consider a perfect blackbody radiating energy at thermal equilibrium, barring any convective or conductive processes, the energy that the perfect blackbody radiates must come from somewhere. A perfect blackbody must abide by the principles of energy conservation, meaning that in order to radiate energy the blackbody must also absorb energy. More to the point, the blackbody must absorb the same amount of energy that it radiates in order to remain at equilibrium. By virtue, of conservation of energy emissivity must equally describe both the efficiency of an object to emit and absorb radiation. This equivalency is known as Kirchhoff's law of absorption for objects under thermal equilibrium,

$$\varepsilon = \alpha \tag{II.3}$$

where α is the absorptivity. For the sake of this work, we will assume that thermal equilibrium is satisfied at all times. The equivalency between the emission and absorption of a source is fundamental to many aspects of passive MSMW radiometry, which will be discussed in a later section.

Brightness temperature is unique and convenient way to describe the ability of an object to emit radiation. In words, brightness temperature, often shown as T_b, is the temperature at which a radiating source appears to be according to its measured spectral radiance, i.e. it is equivalent to T_a in Equation II.2. It can be expressed mathematically as seen in Equation II.4.

$$T_b = \frac{h\nu}{k}\left(ln\left[1 + \frac{2h\nu^3}{I(\nu, T_{app})c^2}\right]\right)^{-1} \tag{II.4}$$

Where the constants and variables shown are as previously described. Note that brightness temperature is found by simply solving Planck's law of a non-blackbody object for T. Considering that there is no such thing as as perfect blackbody, a radiometer will always measure radiance of an object according to its brightness temperature, not its physical temperature. The concept of brightness temperature is very useful for scientists that analyze radiometer data and is also useful for radiometer calibration.

2.3 Approximation of Planck's Law

When possible, engineers and scientist will approximate Planck's law to simplify calculations and decrease the computational time needed to process data or perform simulations. This simplification comes in the form of the Rayleigh-Jeans approximation, which states that under the condition that $h\nu \ll kT$, Planck's law can be reduced to Equation II.5.

$$B(\nu, T) = \frac{2\nu^2 k}{c^2} T \tag{II.5}$$

Where the constants and variables shown are as previously described. Note that in this formulation, $B(\nu, T)$, in Equation II.5, is linearly proportional to the temperature of the source. This approximation can be easily derived by performing a Taylor series expansion of the exponential term in Planck's law. This simplification also has effects on the definitions of emissivity and brightness temperature. Recall Equation II.2 and substitute the numerator and denominator with approximated versions, like shown in Equation II.6.

$$\varepsilon = \frac{\frac{2\nu^2 k}{c^2} T_b}{\frac{2\nu^2 k}{c^2} T} \tag{II.6}$$

Equation II.6 will reduce to Equation II.7.

$$\varepsilon = \frac{T_b}{T} \tag{II.7}$$

This means that within the Rayleigh-Jeans approximation emissivity, and by proxy absorptivity, is equal to the quotient between the brightness temperature of an object and its physical temperature. This approximation also allows one to define brightness temperature as the product of an object emissivity and physical temperature. These approximations greatly increase the ease at which data analysis can be done on radiometer data. However, it is very important for one to be conscious of the conditions in which this approximation can be used. It will be seen in a later section that the Rayleigh-Jeans approximation cannot be used at all TWICE frequencies, and therefore, Planck's law must be used in full.

2.4 Atmospheric Radiometry Techniques

The scope of the section, and this paper at large, does not include a detailed description of the fundamental processes of radiation in the atmosphere. In order to give a basic understanding and justification for why the radiometers on the TWICE instrument are used, a high level explanation regarding temperature and humidity sounding, as well as ice particle sizing will be given.

2.4.1 Radiative Transfer Equation

To fully understand what the TWICE radiometers will be observing, one must first consider how radiation is transferred through the Earth's atmosphere. EM radiation emitted from an arbitrary source must travel through the atmosphere before it can be detected an Earth observing satellite. Along the path of radiation, countless numbers of atoms and molecules, ice particles, rain drops, etc., absorb and reemit or scatter the EM radiation. Through this process, the amount of radiation being observed along a particular path can become attenuated or even grow in magnitude. To begin quantifying this phenomenon, consider Lambert's law of extinction, shown in Equation II.8.

$$dI_v = -\sigma_{ext} I_v ds \tag{II.8}$$

Equation II.8 states that a change in intensity, dI_v, is equal to the product of the extinction coefficient, σ_{ext}, incident intensity, I_v, and the path through which the radiation is traveling, ds. This is also represented in Figure 6.

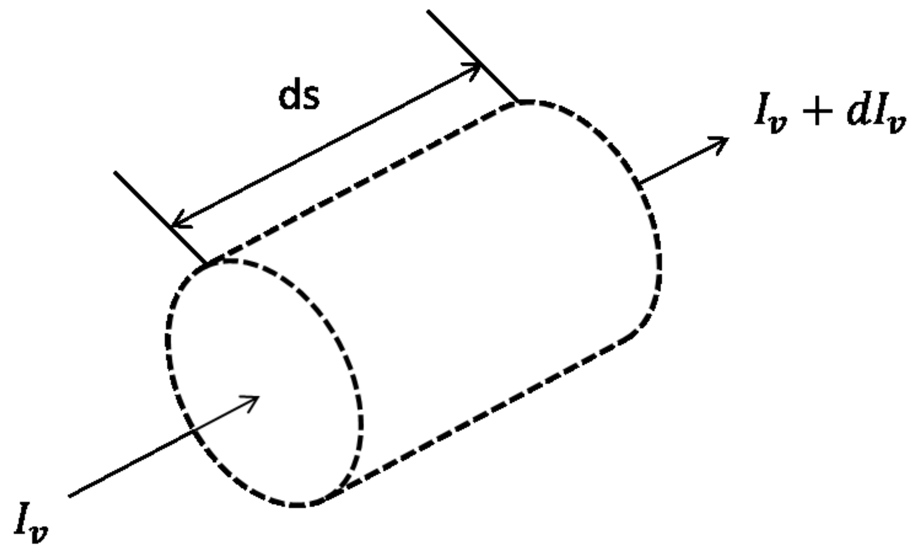

Figure 6: An illustration of Lambert's law of extinction

The extinction coefficient can be described in Equation II.9 as the sum of the extinction that EM radiation will experience resulting from both absorption and scattering.

$$\sigma_{ext} = \sigma_{abs} + \sigma_{sct} \tag{II.9}$$

While the atmosphere can attenuate radiation traveling through it, it can also act as a source which can add to the intensity of the propagating radiation. In order to simplify how the atmosphere can act as a source of emission, the absorption term of the extinction coefficient is considered. Rearranging Equation II.8 and adding in a source term gives Equation II.10.

$$\frac{dI_v}{ds} = \sigma_{abs}[I_v - B_v] \tag{II.10}$$

This is known as the Schwarzchild equation, where B_v is the emission term that follows Planck's law. Note that modeling the emission term as a function of Planck's law, B_v, requires that the atmosphere be in thermal equilibrium. Within the scope of this work it is assumed that the atmosphere is in thermal equilibrium and that only the absorption term of the extinction coefficient is considered. To better suit the downward looking nature of satellite observation, we can make the assertion that $ds = {}^{dz}/_{\mu}$, where $\mu = \cos(\theta)$, θ being the solar incidence angle. By making this substitution and integrating both sides, Equation II.11 is found.

$$I_v = I_{v0}\tau_0 + \int_0^{\infty} B_v(z)\frac{\sigma_{abs}(z)}{\mu}\tau(z)dz \tag{II.11}$$

Generally, Equation II.11 is known as the radiative transfer equation, written in terms of transmission, for a non-scattering atmosphere. Where I_{v0}, is the intensity of the original source, τ_0 is the transmission of the entire atmosphere, $B_v(z)$ is the emission term of the emitting layer along the path of radiation, and $\tau(z)$ is the transmission term of the atmosphere above the emission layer [19]. For a scattering atmosphere, the general extinction coefficient is used and a new term must be introduced that describes the scattering behavior of the radiation of interest. The scattering behavior is determined by several different parameters including frequency of the radiation and size of the scatterer. This can be very difficult to model, and is outside the scope of this work.

2.4.2 Sounding

Sounding, in the field of passive radiometry, is the process of detecting signals along strong absorption or emission bands. These sounding signals radiate at defined frequencies and are unique to a single atmospheric constituent. For example, the TWICE passive radiometer instrument utilizes 3 sounding radiometers centered at approximately 118 GHz, 183 GHz, and 380 GHz. Each of these sounding radiometers utilizes 4 different frequency channels. The 183 GHz and 380 GHz channels are used to detect emissions from water molecules in the atmosphere and therefore are appropriately called humidity sounders. The 118 GHz channel detects emissions from homonuclear oxygen molecules in the atmosphere. These oxygen emissions are highly dependent on the physical temperature of the gas, and therefore these channels are called temperature sounders. In many ways the presence of water vapor, and its emissions can contaminate the ice particle sizing channels on the TWICE instrument. However, introducing sounding channels that can profile temperature and water vapor within the same pixel help to remove contamination.

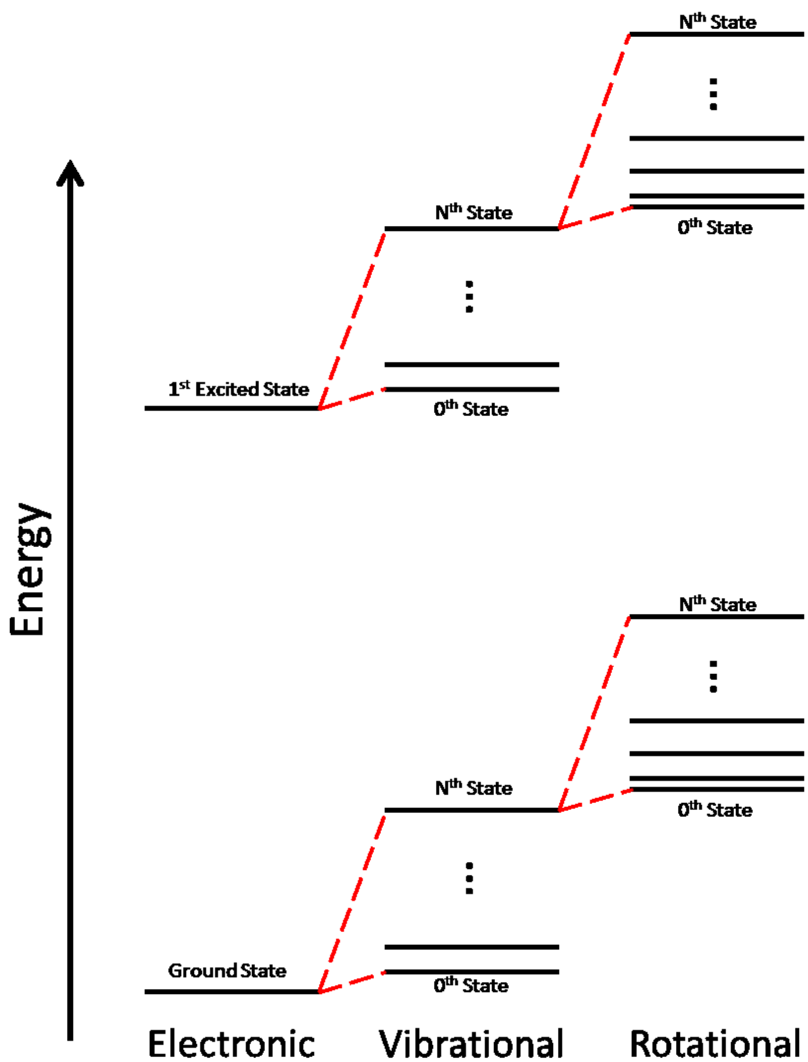

Figure 7: A depiction of the general energy structure for state transitions for an arbitrary molecule.

Radiation emitted from atmospheric constituents can have different origins including emission due to rotation, vibration, or electron energy transitions. Each of these radiation mechanisms adhere to the laws of quantum mechanics meaning that the electromagnetic radiation they produce is described by Planck's law. For example, consider the sounding frequencies used by TWICE. Due to the relative size of the wavelength and the low amount of energy carried at these frequencies, compared to say IR or UV radiation, they often correspond with rotational transitions. A general structure of these state transitions can be seen in Figure 7. Rotational transitions make up the finer structure shown in Figure 7 and require the least amount of energy to achieve, compared to electrical transitions, which require the most.

In short the TWICE passive radiometer sounders detect the energy emitted from rotational transitions in water and homonuclear oxygen molecules. Passive radiometers used for sounding are generally used to determine the vertical profile of the constituents they are observing. In the case of TWICE, the 183 GHz and 380 GHz channels are used to determine the vertical profile of water vapor in the atmosphere, and the 118 GHz channel is used to determine the vertical profile of temperature. Due the strong absorption and emission at the sounding frequencies of water vapor and oxygen, radiometers which are designed to detect signals right on the sounding frequencies will typically only see the very top of the atmosphere. This is because the atmosphere appears to be very opaque right at these particular frequencies. However, if a radiometer was designed to operate at a frequency slightly off from a sounding frequency, for example 180 GHz for water vapor, the atmosphere would appear to be slightly more transparent, allowing the radiometer to detect radiation that is being emitted from deeper within the atmosphere. This technique of using a radiometer that operates right at a sounding frequency along with consecutive radiometers that operate at frequencies that are increasingly farther from the sounding frequency allow scientist to view the atmosphere at discrete levels, thus providing them with a vertical profile. This can be seen for the two water vapor sounding frequencies in the TWICE instrument in Figure 8.

In order to perform sounding, weighting functions must be defined. Weighting functions help to identify the layers at which most of the observed radiation is coming from for a particular frequency. Put simply, weighting functions describe how the transmission term, $\tau(z)$, changes as function of changing altitude, z, seen in Equation II.12. In many cases, the weighting function will have units of invers kilometers, noting that the transmission term is unit-less; plotting Equation II.12 as a function of altitude results in a plot similar to Figure 8.

$$W(z) = \frac{d\tau(z)}{dz} = \frac{\sigma_{abs}(z)}{\mu}\tau(z) \tag{II.12}$$

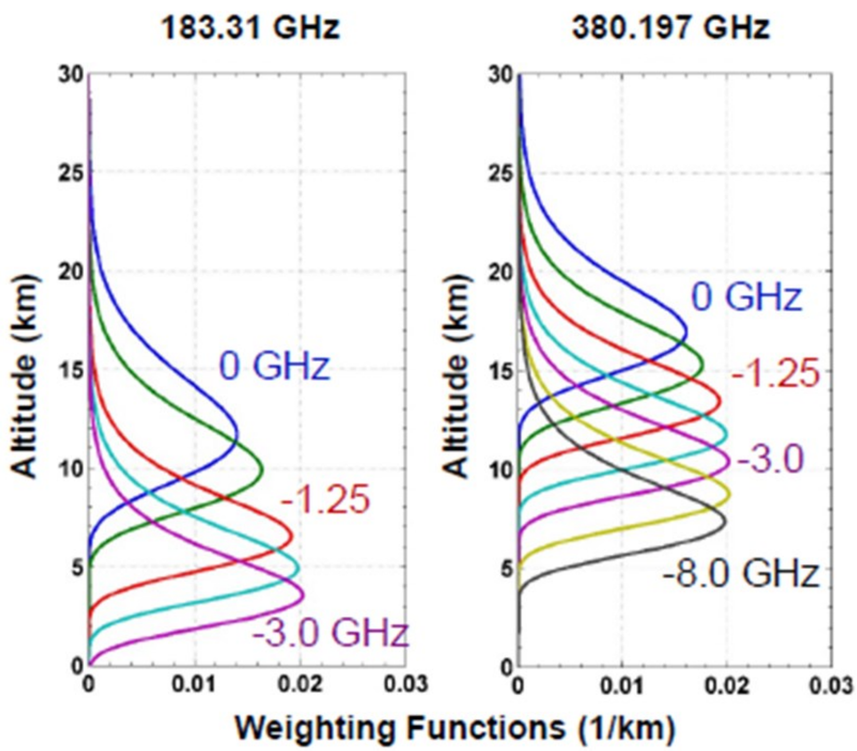

Figure 8: Plots showing the relative emissive weight of several atmospheric layers for the TWICE 183 GHz and 380 GHz sounding radiometers [16]. The 380 GHz absorption line is stronger than the 183 GHz line, emitting radiation from higher in the atmosphere.

Physically, atmospheric sounding, or the ability to observe different layers of the atmosphere, is made possible by a phenomenon known as pressure broadening. By way of quantum mechanics, it would seem that radiation emitted from an atom or molecule would be very unique and discretized. That is to say, for a single atom or molecule every transition, like those shown in Figure 7, requires an exact amount of energy to achieve. In the case of emission, an atom or molecule falling from one energy state to another will emit a very specific amount of energy at a specific frequency. If the energy requirements are not exactly met, a transition will not occur. For example, one of the rotational state transitions that allow water molecules to emit radiation only occurs at precisely 183.31 GHz. However, as seen in Figure 8, the TWICE radiometers are able to measure radiation emitted by water vapor at frequencies around 180.31 GHz. This spreading out of quantum energy is the result of pressure broadening.

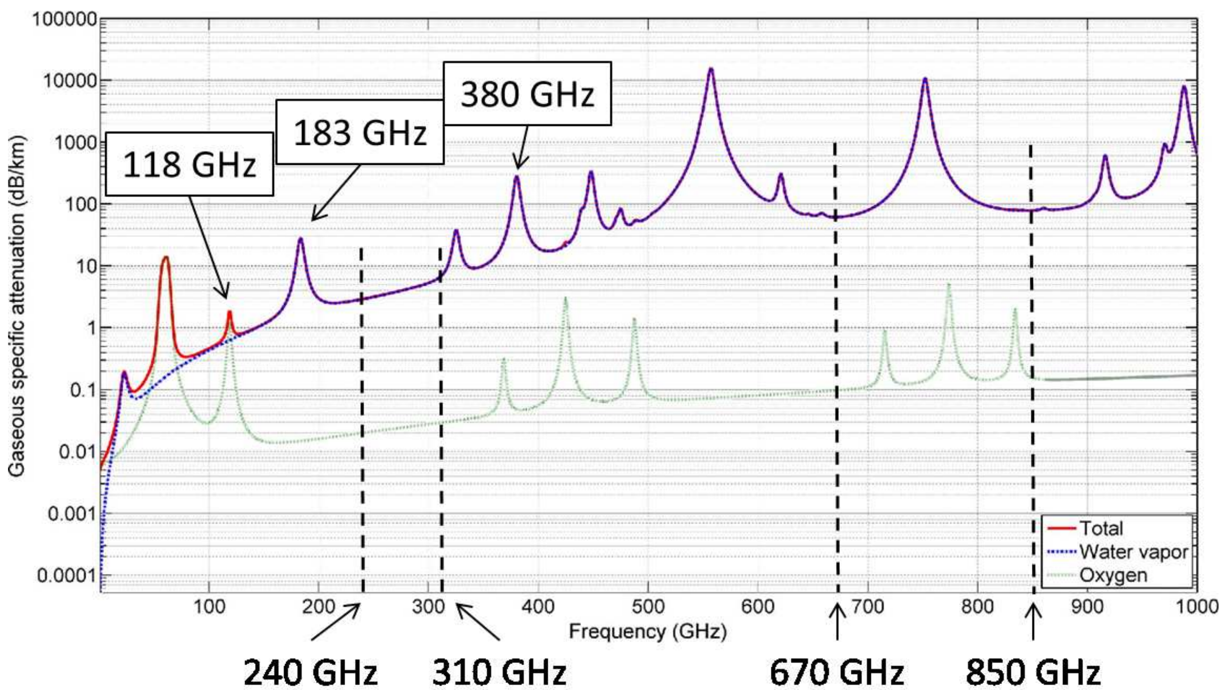

Figure 9: A plot showing atmospheric attenuation, i.e. absorption, for the GHz frequency range. Attenuation is shown for atmospheric water vapor and oxygen, as well as the sum total of the two constituents [20].

For cases of single atoms or molecules, the absorption or emission of radiation must be exact. However, Earth viewing microwave radiometers do not observe single constituents; rather they observe the numerous atoms and molecules that make up the Earth's atmosphere. These countless atoms and molecules do not have space to move freely, but instead constantly bump into one another exchanging energy. It is these kinetic interactions that cause atoms and molecules to absorb and emit microwave radiation at energies and frequencies slightly off from the nominal spectral line.

2.4.3 Scattering

In conjunction with sounding, the TWICE instrument also uses direct detection radiometer channels at 240, 310, 670, and 850 GHz. Unlike the TWICE sounding channels, these frequencies have not been chosen with regard to strong absorption for a particular atmospheric constituent. Instead, these frequencies are purposely selected to lie as far off of absorption lines as possible. The purpose of these channels is to observe how radiation coming from the Earth's surface or lower atmosphere is effected by constituents in the upper atmosphere, specifically ice particles. Figure 9 provides an illustration of where, in frequency space, the aforementioned direct detection radiometer channels are place with respect to the TWICE sounders [20]. Observing the evolution of radiation through the Earth's atmosphere requires that the observing frequencies not be sensitive to the emissions of any atmospheric constituent. In the GHz range, the strongest sources of emission come from water vapor and oxygen. In Figure 9 it can be seen that each of the ice particle sizing channels are placed between absorption peaks. The space between absorption peaks are known as windows. Windows are areas in the electromagnetic spectrum that are poorly absorbed by the atmosphere. The ice particle sizing frequencies are located in areas where the amount of absorption is still fairly large, even though these frequencies lie off of strong absorption lines. These windows exist only relative to the strong lines of absorption around them, and as a result are called quasi-windows. Because the absorption, and therefore emission, of these quasi-window channels are not affected by the presence of any particular atmospheric constituent, they are very useful for studying how radiation is scattered in the Earth's atmosphere.

Simply put, scattering is the process of a particle redirecting EM radiation. A particle is defined by its relative size to the EM radiation it will be interacting with. For example, molecules in the atmosphere tend to be proportional in size to visible wavelengths, particularly the color blue. In the millimeter- and sub-millimeter-wave region, scattering particles tend to be ice and water droplets. Continuing on this track, even the entire Earth can act as a scattering particle, given a large enough wavelength. The size of the scattering particle, relative to wavelength, will determine how the interacting EM radiation will be redirected. The type of scattering experience by EM radiation can be categorized into Rayleigh, Mie, and Geometric. These classifications can loosely be defined by a value known as the size parameter, which is given by Equation II.13.

$$x = \frac{2\pi r}{\lambda} \tag{II.13}$$

In Equation II.13, r is the radius of the interacting particle, and λ is the wavelength of the incident radiation. In the case of Rayleigh scattering, $x \ll 1$, the size of the particle is much less than the wavelength of the incident radiation. Mie scattering is considered when the size of the particle is approximately the same size as the incident radiation, or $x \approx 1$. Geometric scattering occurs when the particle is much bigger than the incident radiation, or $x \gg 1$. These conditions can be summarized in Figure 10. The likelihood that radiation will be scattered towards a particular direction is ultimately determined by the size parameter, but can be quantified by a value known as the phase matrix, $\boldsymbol{P}(\theta)$. The phase function describes a cloud of probable directions that incident radiation will be scattered into, and is a function of scattering angle as shown in Equation II.14.

$$cos(\theta) = \mu\mu' + (1-\mu^2)^{\frac{1}{2}}(1-\mu'^2)^{\frac{1}{2}}\cos(\varphi - \varphi') \tag{II.14}$$

Where EM radiation incident from angle (μ', φ') is scattered into angle (μ, φ). Equation II.15 states that the integral of the phase matrix over all space is equal to 1, meaning that the total probability of incident radiation being scattered in any arbitrary in any direction is 100% [21].

$$\frac{1}{4\pi}\int P(\theta)d\Omega = 1 \tag{II.15}$$

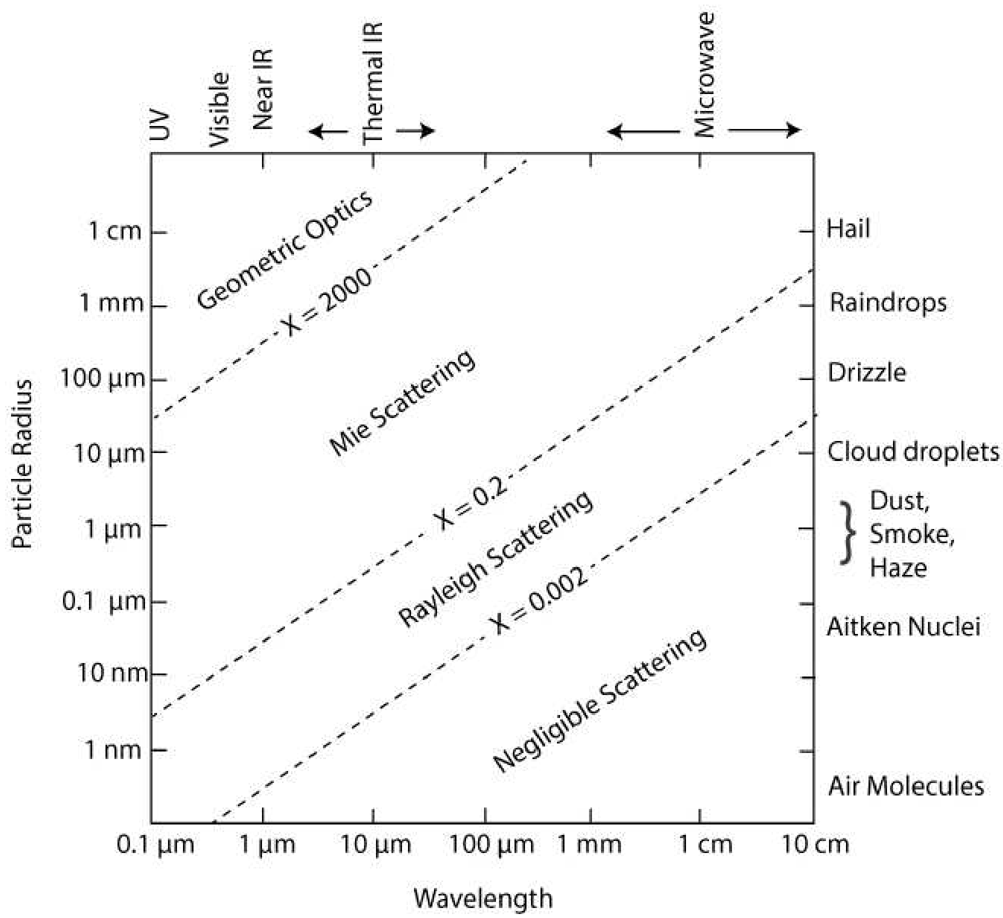

Figure 10: A graph showing the relationship between wavelength, particle size, and type of scattering [22].

The phase function is generally represented by a two-dimensional polar plot indicating which directions are most likely for the incident radiation to be scattered. An example of these plots can be seen in Figure 11 [23]. Figure 11 shows how the phase function evolves with a changing size parameter. Rayleigh scattering is often characterized by an equal amount of forward and backward scattering (A). As the size parameter grows, the amount of forward scattering greatly increases and the amount of backward scattering greatly decreases (B – D). As this trend continues, practically all of the incident radiation is scattered in a forward direction converging to what is known as geometric scattering. Another way to think about geometric scattering is to consider a rainbow, which is formed as a result of visible light undergoing geometric scattering within droplets of rain.

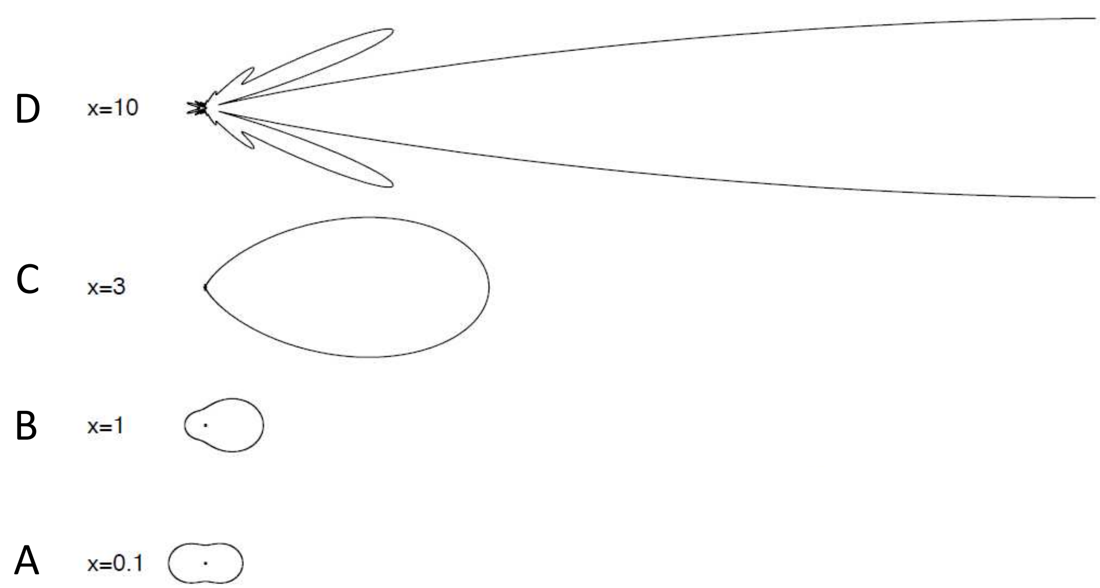

Figure 11: Increasing size parameter results in an increased amount of forward scattering [24].

The concepts of scattering in the atmosphere are very helpful when trying to determine particle size by way of remote sensing. One common method of estimating particle size with remotely sensed data is known as optimal estimation (OE). In layman's terms, OE is a type of algorithm that utilizes numerous different simulations with slightly different input parameters. Most importantly, these input parameters include particle type and size, as well as several other characterizing values. Each simulation produces a set of calculated brightness temperatures that would be observable at the top of the atmosphere for a given frequency. These simulated brightness temperatures are then compared to the brightness temperatures measured by the remote sensing instrument. A cost function analysis is then performed to determine how closely the simulated and the actual brightness temperatures match. The process is repeated over and over again until a minimum cost function value has been reached. Once the cost function has been minimized, it is estimated that the particle characteristics used to run the simulation match the characteristics of the particles that produced the brightness temperatures observed by the radiometer instrument. The aforementioned simulations make use of the radiative transfer equation that was discussed in Section 2.4.1, however, these simulations require that the radiative transfer equation be modified to include scattering.

TWICE is expected to be able to detect brightness temperature changes due to high altitude ice particles between the sizes of 100 to 1000 μm. Previous missions have shown to be sensitive to particles outside of this range. For example, CloudSat's 94 GHz radar is sensitive to particles larger than approximately 600 μm, whereas the Moderate Resolution Imaging Spectroradiometer is sensitive to particles smaller than approximately 50 μm. However, measurements show that number density of ice particles tends to peak for sizes between 100 to 1000 μm. Other instruments are currently in development that are sensitive to this range of ice particles sizes, for example the Ice Cloud Imager (ICI) in development by the European Space Agency.

Chapter III The TWICE Scanning Strategy

3.1 TWICE Instrument and Chassis Structure

The TWICE radiometer instrument is designed to fit within a 6U CubeSat. However, due to its optical design, TWICE employs a relatively open configuration, shown in Figure 12. The entire TWICE instrument must be scanned during nominal operation. This is largely due to the differing optical properties of the individual radiometer receiver blocks. This forces the front of the 6U CubeSat frame, as well as the calibration system to be very open. Figure 12 points out the two different targets used for calibration. Notice both their placement and differing structure. The TWICE calibration process requires that each of the radiometers regularly observe both a hot and a cold point of reference. Where, in this context, "hot" and "cold" are defined relative to each other. Under nominal conditions, the temperature of the hot target, which is called the ambient calibration target, should be approximately 300 K, and the cold target, called the CMB reflector, should be approximately 3 K. What is important, however, is the location of the calibration targets. Because the calibration targets are placed to the sides of the 6U CubeSat frame, the entire instrument must rotate far enough so that it is able to observe the targets with minimal contamination from radiation below the targets. The unobstructed azimuthal space between the calibration targets is used by the TWICE primary reflector to receive radiation from the Earth. This radiation is represented by the yellow ray in Figure 12.

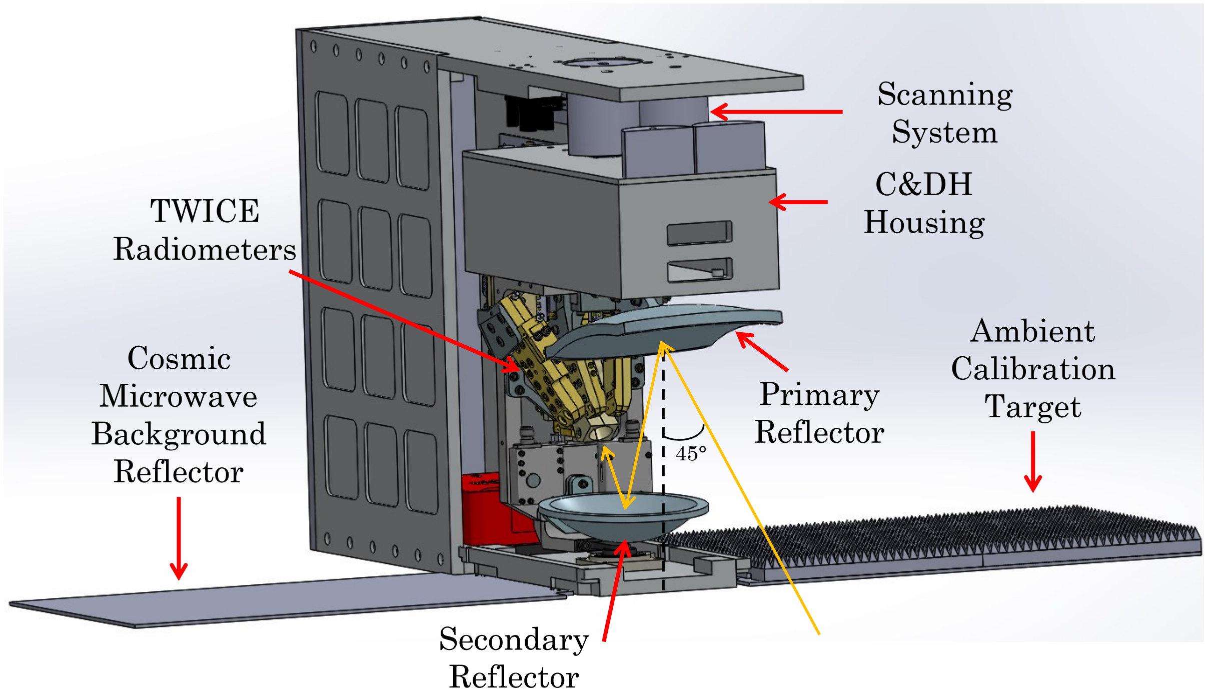

Figure 12: A CAD model of the TWICE instrument and 6U CubeSat frame.

Towards to the top of the TWICE 6U CubeSat frame is a scanning mechanism, pointed out in Figure 12. This scanning mechanism is designed to perform the scanning of the TWICE instrument and must be able to control the angular velocity at which the instrument is rotated. The scanning mechanism is attached to what is referred to as the control and data handling (C&DH) housing. This housing, apart from protecting the circuit boards responsible for regulating power to and collecting data from the TWICE radiometers, connects the scanning mechanism to the rest of the TWICE instrument.

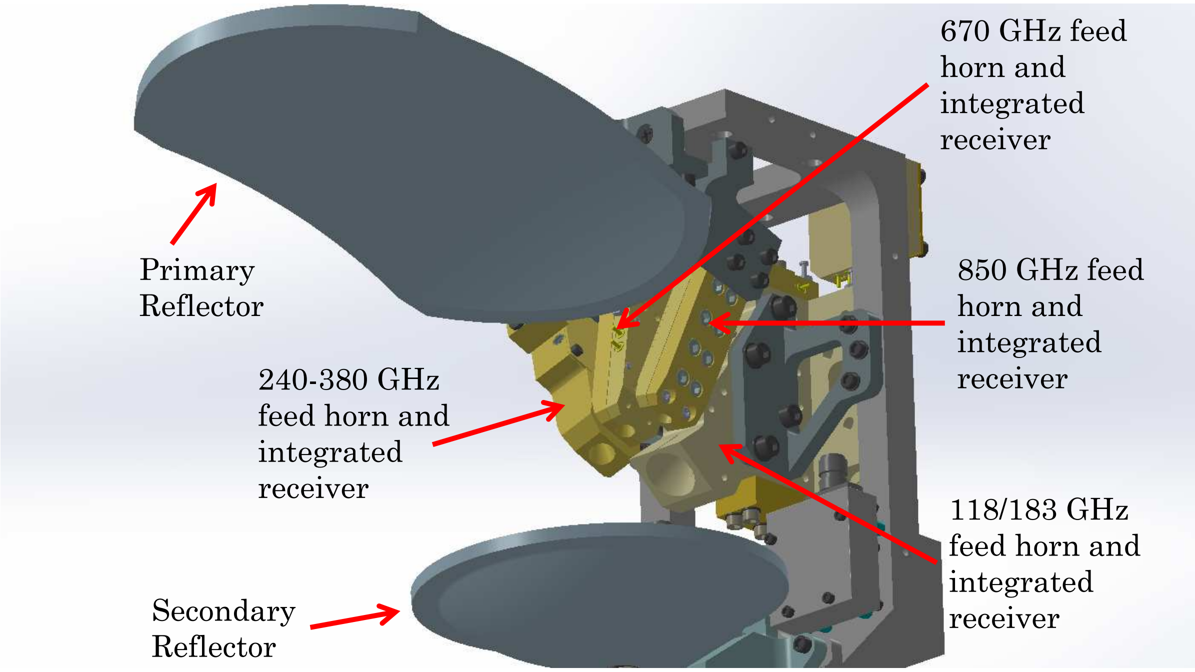

Figure 13: A zoomed in view of the TWICE radiometer instrument.

The enclosed area behind the instrument is used to store various control and interface boards, as well as the space craft power supply and attitude control system. A closer look at the scanning radiometer instrument can be seen in Figure 13.

The placement of each of these structural components contribute to the scanning strategy employed by the TWICE instrument. From Figure 12 it is understood that the TWICE radiometer instrument is incapable of scanning continuously in one direction, this is due to the chassis walls that are needed to house and support the spacecraft vitals. In place of continuously scanning in one direction, TWICE must implement an oscillatory scanning technique, rotating the radiometer instrument back and forth between observing the “hot” and “cold” targets, with Earth observation in between. Figure 14 shows the moving and stationary part of the TWICE 6U CubeSat

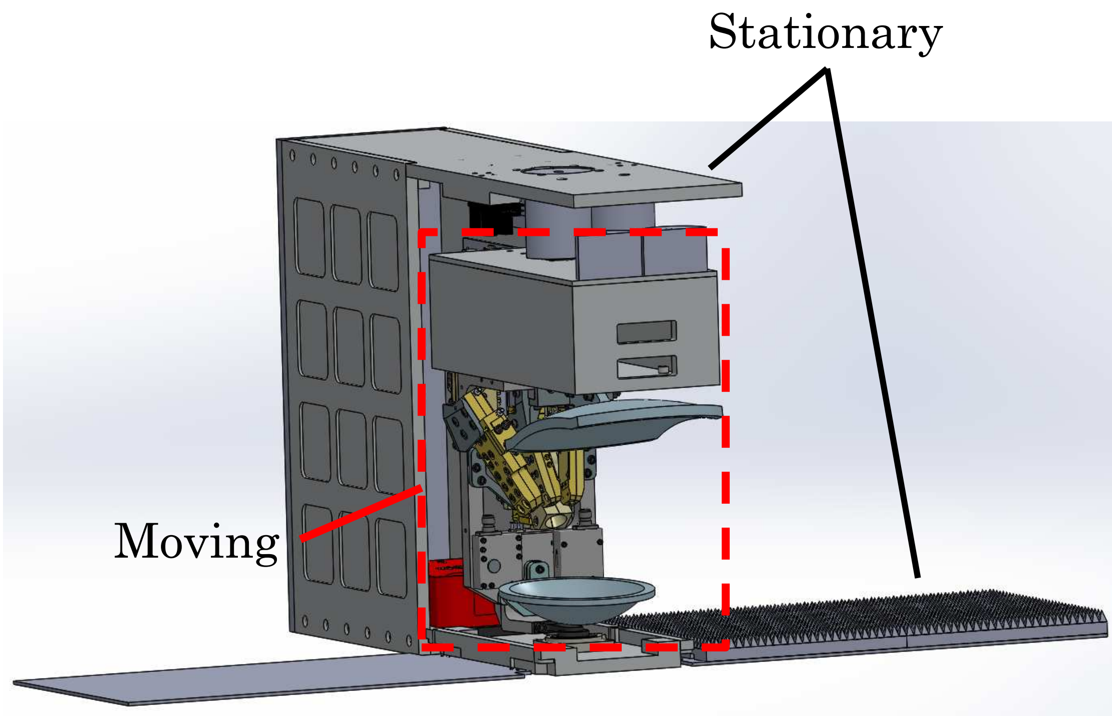

Figure 14: The TWICE radiometer instrument makes up approximately one third of the total size and mass of the entire 6U CubeSat vehicle.

3.2 Scanning Techniques

There are several different ways of observing the Earth's surface with a spaceborne instrument. These different methods are referred to as scanning techniques and are generally used to help increase the amount of the Earth's surface observed for a single orbit. Some of these techniques are shown in Figure 15. Figure 15 (A) shows a technique known as conical scanning, which is the technique utilized by the TWICE radiometer instrument. Conical scanning is characterized by maintaining a constant angle of incidence on the Earth's surface. To achieve a constant incidence angle, the instrument must be scanned in such a way that the instrument footprint traces out a circle on the Earth's surface. Maintaining a constant incidence angle is very useful for polarized or window channel radiometers where polarization of observed radiation is often a function of incidence angle. Conical scanning also helps to maintain a constant footprint resolution throughout the entire scan, which is helpful when processing radiometer observation data. However, conical scanning can pose some issues in terms of mechanical design. For example, in some cases, like that of TWICE, the only way to perform conical scanning is by rotating the entire radiometer instrument. This can prove to be very problematic in regard to power consumption and spacecraft stability.

Another scanning technique is known as cross track scanning, shown in Figure 15 (B). Unlike conical scanning, cross track scanning does not maintain a constant angle of incidence or foot print resolution. While this type of scanning can prove to be more computationally difficult during data processing, it can utilize a simpler mechanical design. Cross track scanning instruments, like TEMPEST-D, can often be simplified by only rotating a single mirror aiding mechanical design and minimizing the power consumption of the scanning motor. Cross track scanning instruments also tend to have a much wider swath width, allowing them to make observations out to the horizon [25].

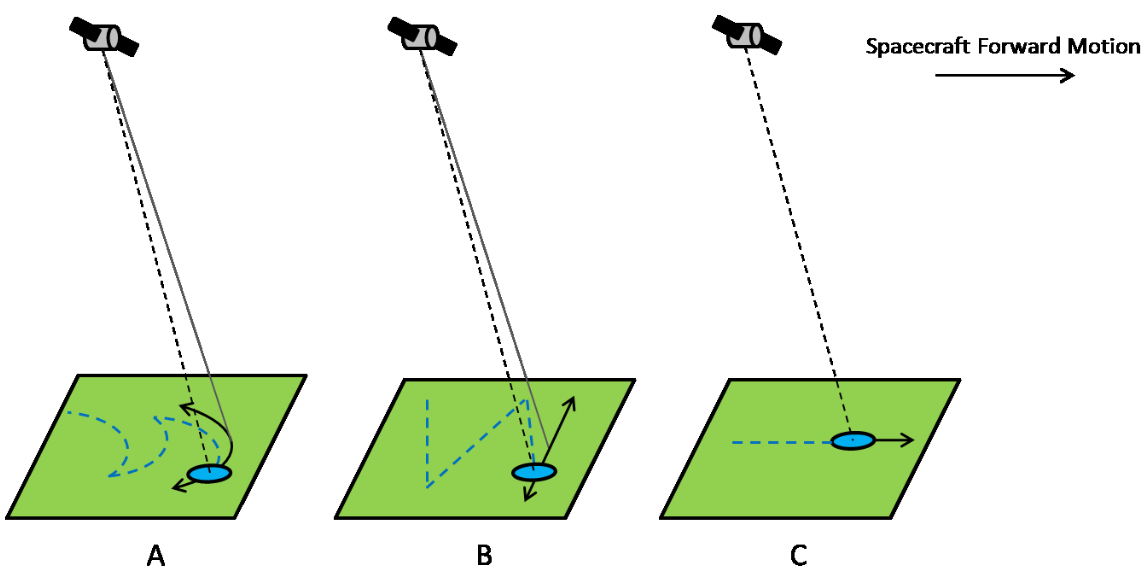

Figure 15: Earth observing instruments can view the Earth with a conical scanning technique (A), a cross track scanning technique (B), or a push broom technique (C).

Push broom scanning, Figure 15 (C), is a technique that does not scan the instrument at all. This technique is characterized by an instrument that is always nadir looking and relies on the motion of the satellite orbit to propagate the instrument footprint. This technique is commonly accompanied by an instrument with a large number of stationary radiometers that maximize mechanical reliability, but also reduce data reliability. This idea also points out a large flaw with the push broom technique. Conical and cross track scanning instruments are able to utilize an end-to-end calibration system on board the spacecraft, whereas push broom type instruments cannot. Being able to calibrate a radiometer instrument on orbit is very useful and helps to increase data reliability.

3.3 The TWICE Scanning Design and Characteristics

The development of the TWICE scanning system requires a firm knowledge of the scanning characteristics of the rotating radiometer instrument. That is to say, parameters like acceleration, torque, and moment of inertial will all contribute the scanning system design and stability during operation. In the following sections, acceleration and velocity requirements, as well as torque requirements will all be calculated for the TWICE scanning instrument. The results of these calculations will help to determine what type of scanning system will be used in the final TWICE design.

3.3.1 TWICE Scanning Requirements

Based on the general TWICE frame and instrument structure, as well as the fact that TWICE must be conically scanned, one can begin to piece together a scanning design. It is understood that to maintain high data quality for calibration and Earth observation, the TWICE radiometers must have uncontaminated views of both the calibration targets and the Earth scene. In this sense, uncontaminated means without radiation from any source other than what is being viewed by the radiometers. During calibration, the radiometers should observe a target that is uniform in both temperature and emission of radiation. However, because the primary mirror is always looking towards the direction of the Earth, the observation of the calibration target can be susceptible to stray upwelling radiation from the Earth's atmosphere. To mitigate any contamination from the Earth scene, it is vital that the TWICE radiometers only observe the calibration targets during times of calibration. Likewise, during times of Earth observation, the TWICE radiometers must mitigate any unwanted radiation from any source other than the Earth's atmosphere. By far the most common source of contamination when observing the Earth scene will come from either of the calibration targets. As the TWICE instrument scans, there will be transition zone where both the calibration target and the Earth scene will be partly visible, rendering data from this zone unusable. Figure 16 shows a simple depiction of where the TWICE radiometers can minimize any unwanted radiation for calibration and Earth observation during a nominal scan. In the figure, the 118 GHz channel footprint is used, due do to the fact that the 118 GHz channel has the largest footprint in both the near field and the far field. It is assumed that if contamination can be minimized for the largest footprint, then the higher frequency radiometers, with smaller footprints, should meet this condition as well.

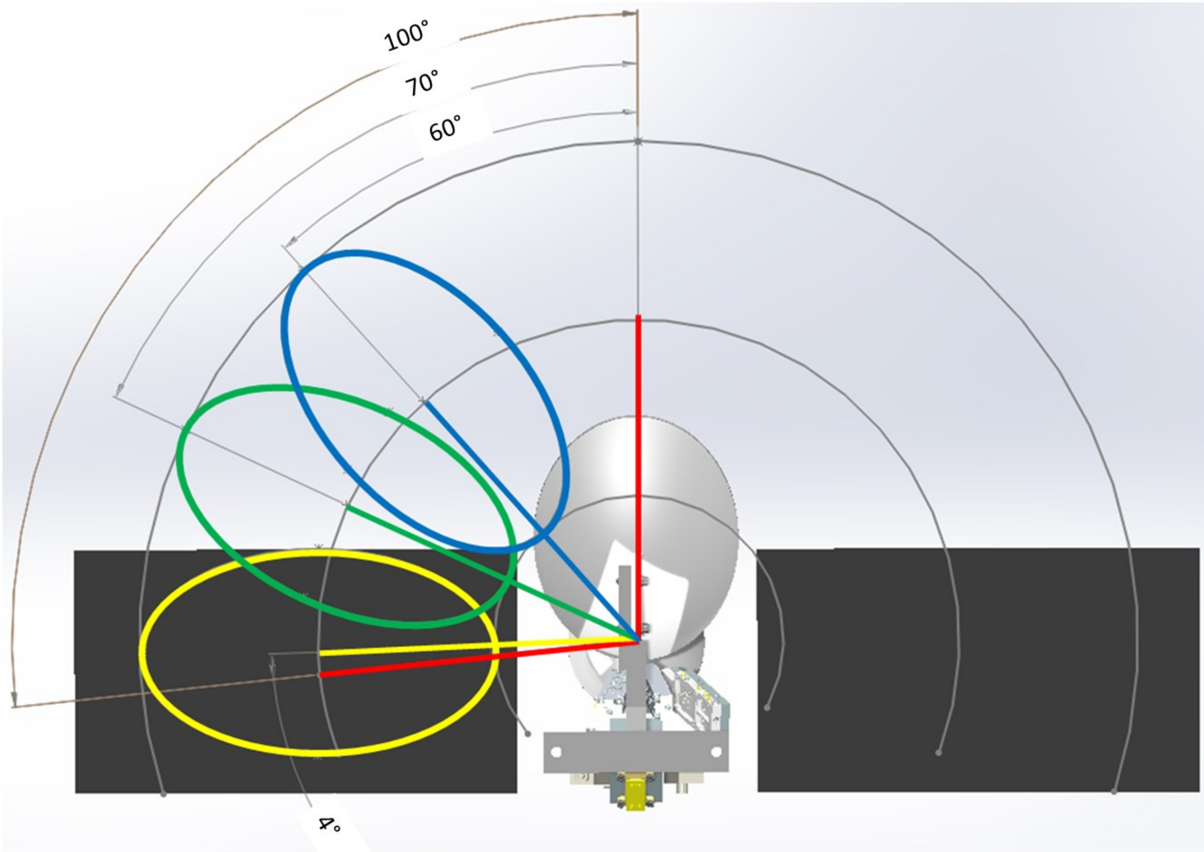

Figure 16: Placement of the TWICE 118 GHz channel 3 dB near field footprint size at three specific points during a nominal scan.

In Figure 16, the yellow footprint represents the location at which all of the TWICE radiometers will be able to observe a calibration target without any contamination from the Earth scene. The blue footprint represents the location at which all of the TWICE radiometers will be able to observe the Earth scene without any contamination from a calibration target. The green footprint depicts a location where the TWICE radiometers are contaminated by either a calibration target or the Earth scene.

As previously mentioned, TWICE makes use of a conical scanning technique. This design was chosen in part by the fact that TWICE uses both polarized and window channels which are sensitive to incidence angle on the Earth's surface. Maintaining constant footprint resolution across the entire TWICE scan also helps with data processing and interoperating ice particle size.

Furthermore, TWICE performs oscillatory scanning which means the TWICE instrument will undergo phases of acceleration and deceleration, and change its scanning direction at the end of each deceleration phase. Building upon the aforementioned structural configuration and contamination analysis, TWICE is designed to scan over a 200 degree arc, where that total arc is segmented into sections designated for specific instrument operations. These sections include regions for acceleration, deceleration and constant velocity, which correspond to specific instrument tasks such as calibration or Earth scene observation. The size of the calibration and Earth scene arcs has been optimized to maximize swath width of the instrument when observing the Earth's surface. Figure 17 shows the total scanning arc as well as the allocated instrument tasks for each arc segment. In order to maintain data quality for both calibration and Earth scene observation, the zone in which calibration will be possible is only 4 degrees. This is followed by a section where both the calibration target and the Earth scene will be visible to the TWICE radiometers, rendering the data collected unusable. Once all of the radiometer footprints have cleared the edge of the calibration target, approximately 40 degrees from the beginning of the scan, the next 120 degrees will be considered the section for Earth scene observation. Once the radiometer footprints reach the edge of the next calibration target, there will again be a section of unusable data and a section for calibration.

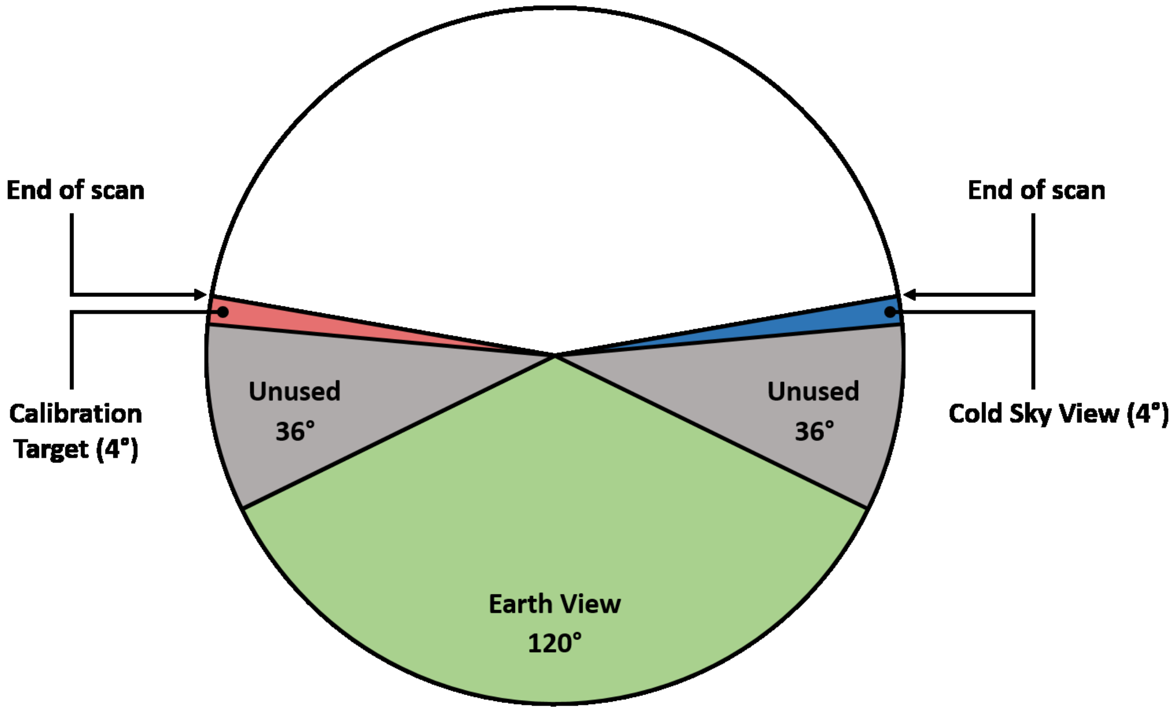

- Total time to scan 200° = $T_{acceleration} + T_{scene} + T_{deceleration} = 1\ s$
- $T_{scan\ revisit} = 1\ s$

Figure 17: An illustration summarizing the TWICE scanning strategy.

Because the TWICE instrument will undergo an oscillatory scanning motion, each of the sections shown in Figure 17 must also be used for acceleration, deceleration, or constant velocity. It was determined that when the TWICE radiometers are observing the Earth scene that the instrument must be scanning at a constant velocity. This determination ensures that sampled pixel on the Earth's surface is contiguously located next to the previous sampled pixel. Assuring constant velocity in the middle of the TWICE scan means that the instrument must accelerate and decelerate at the edges of the scan. Note that it is not required that the instrument be scanning at a constant velocity during times of calibration. As a result, this allows the TWICE calibration targets to be placed at the sides of the 6U CubeSat frame, where the instrument scan will start and stop. This also allows the section where there is unusable data to be used to accelerate the instrument up to the needed velocity for Earth scene observation.

Once the command to begin scanning has been given, the instrument will then accelerate through a 40 degree arc until it has reached its intended nominal Earth scene velocity. During acceleration, the TWICE instrument will perform calibration by observing either a "hot" ambient calibration target or "cold" cosmic microwave background reflector target, shown in Figure 12. Once the instrument has exited the acceleration phase, it will begin rotating at a constant velocity, sweeping out 120 degrees. During this time the TWICE instrument will be performing Earth scene observations. At the end of the constant velocity phase the instrument will then begin the deceleration phase. Similar to the acceleration phase, the instrument will decelerate through a 40 degree arc until it reaches the end of the scan where the rotational motion of the instrument will be completely stopped. Within the last approximately 4 degrees of the declaration section, the instrument will again perform calibration. Once the instrument has reached the end of the scan, and has come to a complete stop, it will then change direction and begin the same scanning procedure in the opposite direction. This process is designed to repeat once every second, meaning that each full scan is one second long, and the revisit time, i.e. the time it takes for the instrument to return to forward looking view, is also one second.

3.3.2 TWICE Acceleration Characteristics

To ensure that the TWICE radiometer instrument will always meet the one second scanning requirement, a minimum rotational acceleration must be determined. Equation III.1 shows that the sum of the time needed for acceleration, constant velocity, and deceleration is equal to the total time of a single scan, t_s. To maintain an inertial symmetry, that is to say to maintain an equal amount of force to accelerate and decelerate the scanning instrument, the time required for acceleration is equal to the time required for deceleration, shown in Equation III.2.

$$t_s = t_{ac} + t_{cnst} + t_{dec} \tag{III.1}$$

$$t_{ac} = t_{dec} \tag{III.2}$$

By way of rotational kinematic equations shown in Equations III.3, III.4, III.5, each of the undetermined time segments in Equation III.1 can be accounted for.

$$\theta_{ac} = \frac{1}{2}\alpha t_{ac}^2 \tag{III.3}$$

$$\theta_{cnst} = \omega t_{cnst} \tag{III.4}$$

$$\omega^2 = 2\theta_{ac}\alpha \tag{III.5}$$

Where α is angular acceleration, θ_{ac} is the arc allocated for acceleration and deceleration, ω is angular velocity, and θ_{cnst} is the arc allocated for constant velocity. Equations III.3 and III.4 are solved for t_{ac} and t_{cnst} respectively, and plugged into Equation III.1. Next, because the speed at which the instrument will be scanning during the constant velocity section is still undetermined, Equation III.5 is solved for ω and plugged in to Equation III.4, which is plugged into Equation III.1. The resulting equation is seen in Equation III.6.

$$t_s = 2\sqrt{\frac{2\theta_{ac}}{\alpha}} + \frac{\theta_{cnst}}{\sqrt{2\theta_{ac}\alpha}} \tag{III.6}$$

Solving Equation III.6 for α yields Equation III.7,

$$\alpha = \left(\frac{2\sqrt{2\theta_{ac}} + \frac{\theta_{cnst}}{\sqrt{2\theta_{ac}}}}{t_s}\right)^2 \tag{III.7}$$

Referring to Figure 17, one is able to assign a value to each of the variables in Equation III.7 and calculate a minimum acceleration of approximately 17 rad/s/s. At this rate of acceleration, the expected constant velocity value across the Earth scene arc is approximately 4.87 rad/s, or 46 RPM.

3.3.3 TWICE Inertial Scanning Characteristics

The TWICE scanning system should be programmable and robust, allowing for several different values for acceleration and constant velocity. Early on in development, it was realized that the scanning mechanism should consume a minimal amount of power, while also minimizing its mass and volume. Due to the oscillatory nature of the TWICE scanning strategy, the scanning mechanism will also have a minimum output torque requirement. In order to better identify what kind of scanning mechanism will be used, a moment of inertia (MoI) calculation was performed on the scanning portion of the TWICE instrument.

The scanning portion of the TWICE instrument, also referred to as the moving part, makes up approximately one third of the total mass of the TWICE 6U CubeSat vehicle. Note a zoomed in picture of the moving part can be seen in Figure 13. It is understood that the torque requirements for the scanning mechanism will be determined by the MoI of the moving part, where MoI about the scanning axis can be defined by Equation III.8 for finite mass elements or Equation III.9 for continuous and variable bodies of mass.

$$I = \sum_{n=1}^{i} m_i r_i^2 \tag{III.8}$$

$$I = \int_V \rho(r) r^2 dV \tag{III.9}$$

Where r is the linear distance from the axis rotation, m_i is a point mass, and $\rho(r)$ is the density of an object as a function of distance from the axis of rotation. MoI is the rotational analog of mass in a linear system, and effectively describes the amount of angular force, torque, needed to accelerate an object. To calculate the MoI of the TWICE moving part, the SolidWorks CAD software was used. By determining the material properties of each of the individual components that make up the TWICE scanning instrument, an approximate mass can be calculated.

SolidWorks also allows one to calculate the location of the center of mass for all of the individual components. Next, the distance of the center of mass from the axis of rotation is calculated, and Equation III.8 is applied. The calculated MoI for the TWICE scanning instrument is approximately 0.00377 kg-m^2.

The final preliminary task that must be completed before selecting a scanning mechanism suitable to rotate the TWICE instrument is a torque calculation. Combining the rotational acceleration analysis from the previous section with the MoI analysis of this section leads to the determination of the torque required to scan the TWICE radiometer instrument. Torque can be calculated with Equation III.10

$$\tau = I\alpha \tag{III.10}$$

Where τ is torque, I is MoI, and α is rotation acceleration. As a result, the torque required to scan the TWICE radiometer instrument is approximately 0.064 N-m.

Chapter IV Design and Testing of the TWICE Scanning System

4.1 Considerations for the TWICE Scanning Mechanism

It is evident that the TWICE scanning mechanism will be made up of a type of electric motor in conjunction with a gearbox. The electric motor can be of many different types including brushless and brushed DC motors, or stepper motors. In regard to what kind of motor will be selected, as well as if there is a need for a gearbox, parameters such as power consumption, size, and control must be considered.

The selected scanning mechanism, i.e. electric motor with a gearbox, will be the ultimate interface between the moving and stationary parts, as it will be connected to both, and is responsible for scanning the moving part. The scanning mechanism will connect the top plate of the TWICE 6U CubeSat chassis and the C&DH housing. The housing is then connected to the rest of the scanning radiometer instrument. Figure 18 shows the amount of space available for the TWICE scanning mechanism. It is obvious that the space allocated for the scanning mechanism is relatively small, less than 1U. Note that in Figure 18, the measured vertical space is from the top face of the C&DH housing to the exterior top face of the top plate of the TWICE 6U CubeSat chassis. Measuring between these two points allows for a bit of extra space while also ensuring that the scanning mechanism stays within the 6U CubeSat envelope. In addition to the scanning system that will be placed above the scanning instrument, TWICE will also utilize a support bearing placed below the scanning instrument. This support bearing will relieve some of the stress on the scanning system associated with scanning and supporting the radiometer instrument. This support bearing can be seen in Figure 12.

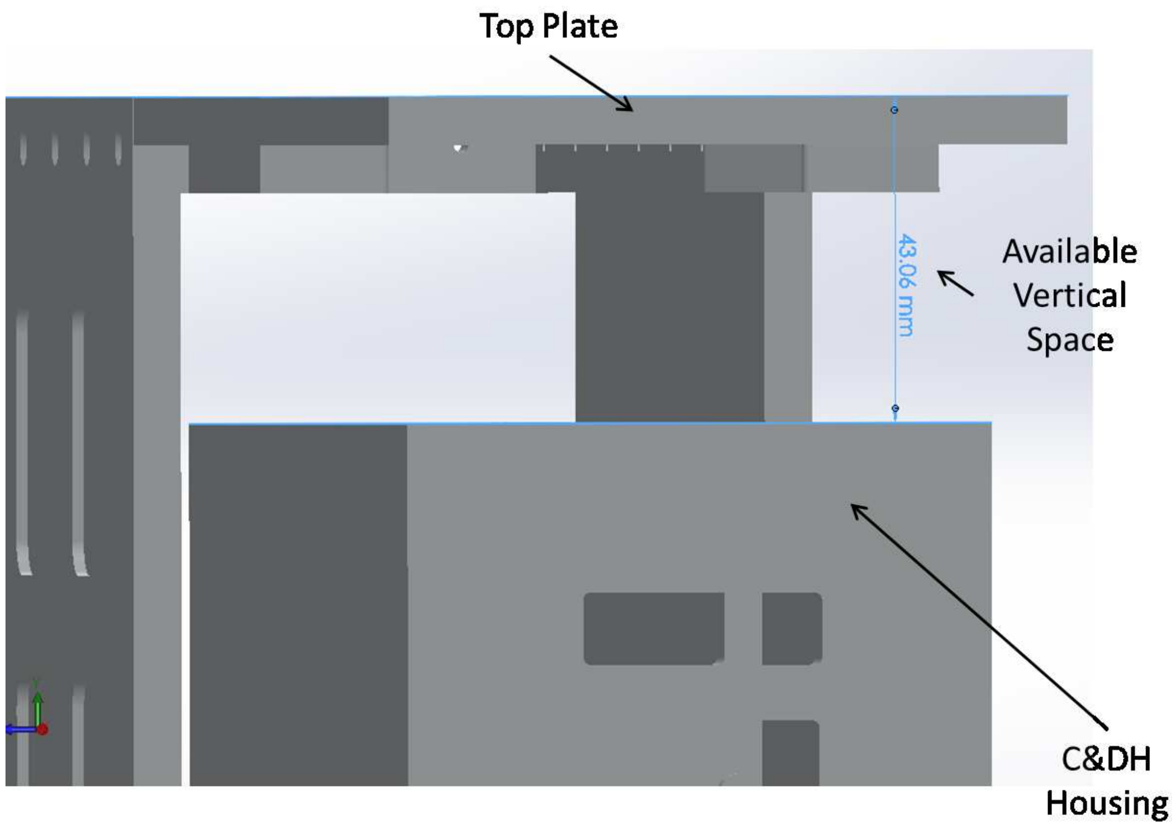

Figure 18: A close up of the available vertical space allocated for the TWICE scanning mechanism.

Power consumption will also play a major role in designing a scanning mechanism for the TWICE instrument. Relative to all of the other TWICE subsystems, the scanning mechanism will by far consume the most power. However, that is not to say efforts to minimize the power consumption should be ignored. It is noted that the amount power required to scan the TWICE radiometer instrument will be increased given that the instrument will need to oscillate back and forth, compared to a continuous scanning technique. An additional parameter comes to mind when evaluating the power characteristics for the scanning mechanism's electric motor: power density. Power density is basically the amount of power deliverable to the rotating payload per unit volume. This value should be optimized so that the power to size ratio is relatively large.

Lastly, the control method required by the selected scanning mechanism should be considered. It is imperative that the angular position of the scanning mechanism be known at all times. The TWICE scanning strategy requires that specific positions be known, e.g. end of the scan or transition from the acceleration phase to the constant velocity phase. It is also very important to locate every radiometer pixel with an angular position so that the data can be processed and geolocated on the Earth's surface. In addition to controlling and knowing the position of the scanning mechanism, the hardware and software needed for operation must also be considered.

By way of comparison, it was determined that a unique solution be used for the TWICE scanning mechanism. Due to its relatively low cost, high torque output, high power density, and small size, a stepper motor was selected. A stepper motor requires a fair bit of hardware and software to operate, namely a microcontroller and a motor driver, and the code to operate those two pieces of hardware. However, unlike other electric motor types, a stepper motor does not need an encoder to track the angular position of the payload it is rotating. Instead a stepper motor can simply count the number of steps it has moved and combine that with the number of degrees in each step. Another feature of stepper motors includes microstepping. Microstepping is basically the process of reducing the number of degrees in each step, allowing the stepper motor to rotate more precisely and consume less power. In an effort to further minimize power consumption while still maintaining high torque output, it was decided that a gearbox be used in conjunction with the stepper motor. A gearbox will allow for a smaller motor to be used while maintaining a high torque output, saving both power and space [26], [27].

4.2 Selection and Design of the TWICE Scanning Mechanism

Given the acceleration and torque requirements of the scanning system, a scanning system can be designed. However, before directing efforts towards the entire scanning system, a motor and gearbox combination must be selected. In the following sections this combination is referred as a scanning mechanism. Neither the stepper motor nor the gearbox was designed by CSU, rather custom assemblies were purchased from proprietary vendors. The following sections detail both the selection of these components and describe the efforts taken to interface these components for nominal operation.

4.2.1 Stepper Motor Design and Operation

To better understand the process of selecting the most appropriate stepper motor for the TWICE instrument, one should understand how a stepper motor works. In words a stepper motor is a type of brushless DC motor that utilizes a permanent magnet rotor with precisely positioned electromagnet stators. The electromagnet stators are polarized by way of inductive currents through wire coils wrapped around each of the stators. Once the stators have been polarized, they remain in that that specific polarization so long as the DC current in their wire coils remains unchanged. This means if one were to simply supply a constant DC current to a stepper motor, the rotor would move by one step and remain locked in place until the current was removed. However, modulating the current through the stator's wire coils in specific sequence will force the rotor to move [26], [27]. A simple depiction of this can be seen in Figure 19.

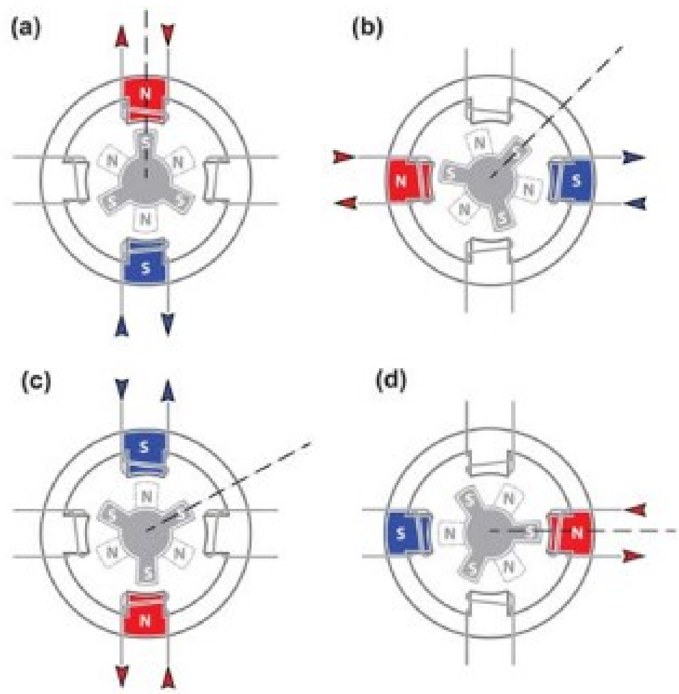

Figure 19: Adjusting the polarity of the individual stators of the stepper motor push and pull the rotor in a rotational motion .

A microcontroller is often used to control the flow of current to and from each of the stators. The microcontroller is programmed to output a series of simple square pulses that then travel to a motor driver. Logic highs initiate a flow of current into the stator's wire coils. Producing a constant stream of pulses will rotate the motor at a constant speed. Adjusting the frequency of the pulses will cause the stepper motor to accelerate or decelerate. Upon receiving a series of stepped pulses from the microcontroller, the motor driver converts the incoming signals by amplifying them, and adjusting the phase and direction of adjacent pulses. At the reception of each pulse, the motor driver will initiate a flow of current to a specific set of stators, adjusting flow back and forth to change the stator polarization.

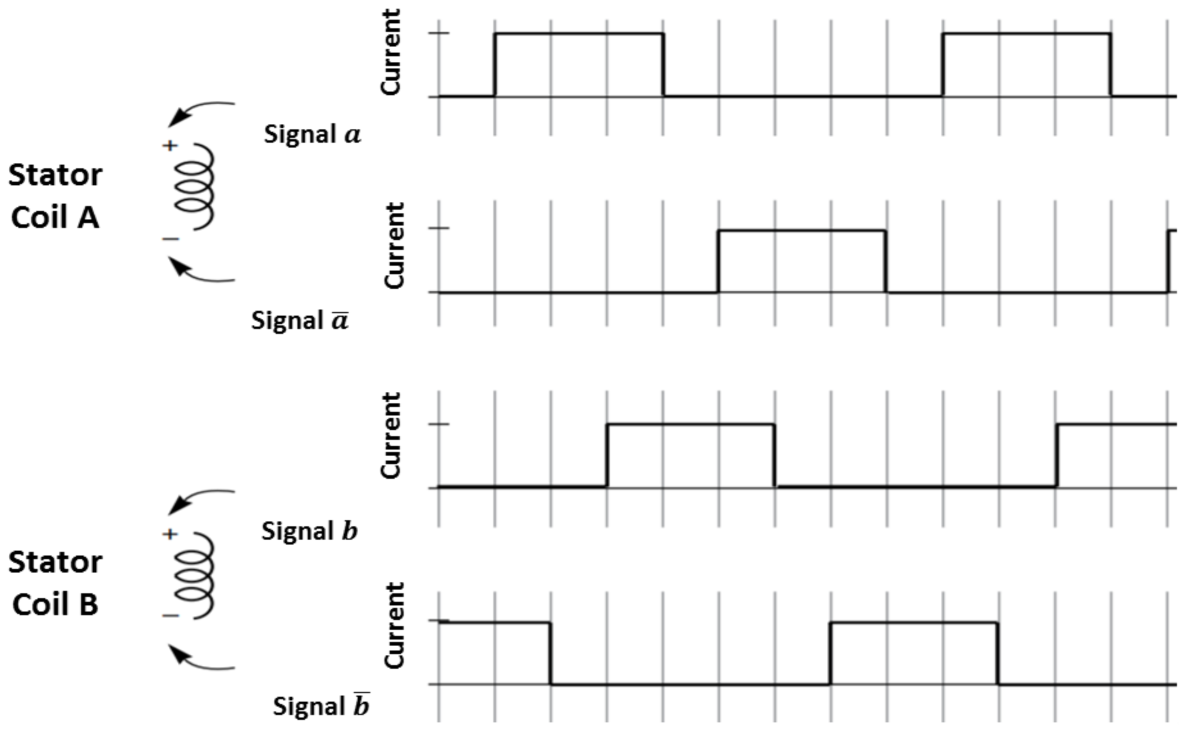

Figure 20: A time series plot showing the phase and direction of amplified step pulses sent from the motor driver to the stepper motor stators [28].

Figure 20 shows a drawing of a stator wire coil where the top and bottom of the coil are labeled as + and – respectively. The + and – symbols do not represent polarity, thus it is not intended to portray a negative current. In the figure, current flows into the stator coils from either the top or the bottom (+ or -). As a result, the magnetic field produced by the coils will change polarity, depending on the direction of the current. Combining signals a and $\bar{a}$ together, as well as signals b and $\bar{b}$, a sinusoidal flow of current is produced in the coils, shown in Figure 21. During the microstepping process, the motor driver simply adjusts the amplitude and phase of the driving step pulses so that more pulses are required to make up a single, full magnitude step. An example of microstepping is seen in Figure 22. The process of microstepping creates smaller and smaller sections by which a single step is made up of. Microstepping allows the stepper motor to run more smoothly, but also reduces the torque output for each step.

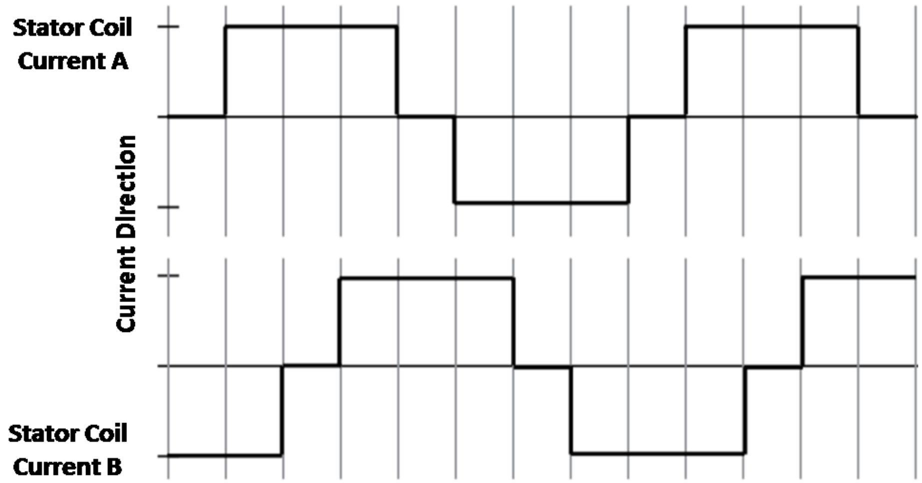

Figure 21: The overall effect of the square pulses sequenced by the motor driver creates a sinusoidal flow of current within the stator's wire coils [28].

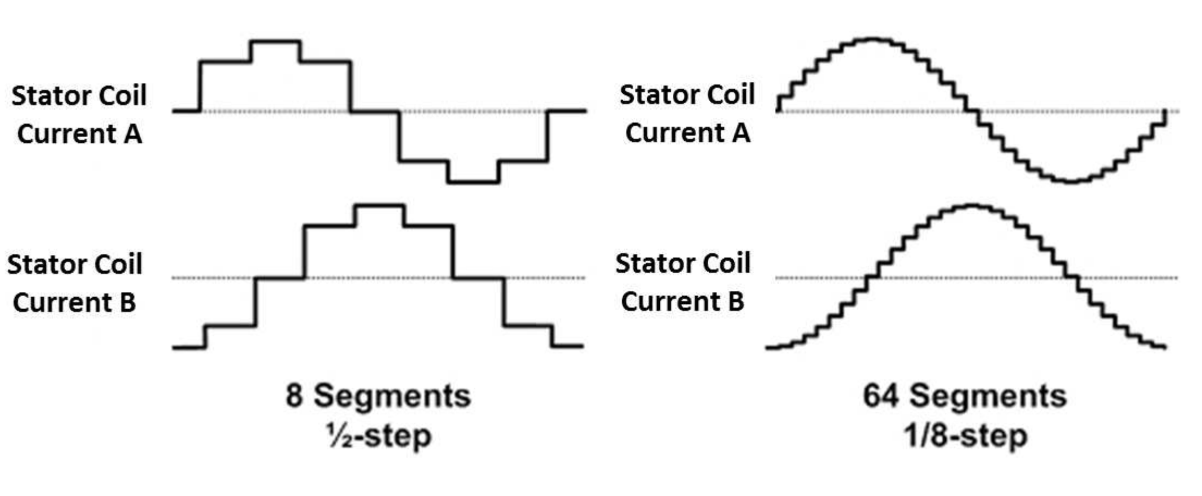

Figure 22: Dividing a full motor step in to several small parts allows the stepper motor to operate more smoothly but reduces its torque output [29].

4.2.2 Selection of the TWICE Stepper Motor

Once the minimum torque requirements of the TWICE scanning instrument were determined, a custom motor could be designed. Almost all of the motor design and manufacturing was done at Lin Engineering, located in Morgan Hill, California. Lin Engineering is a company that specializes in the design and production of stepper motors, and is able to design a stepper motor based on torque and power requirements. It was realized that there would not be an individual motor available that would be able to supply enough torque on its own while also fitting within the space allocated for the scanning mechanism. Motors that were able to provide upward towards 0.064 N-m also required too much power and space to operate for the TWICE system. As a result, it was determined that the stepper motor would need to operate with a gearbox in order to meet all of the inertial and power requirements of the TWICE system. Given the torque requirements, Lin Engineering provided a custom stepper motor design that would need to be used in conjunction with a 30:1 gearbox. The Lin Enineering 3709V-19 stepper motor was selected for use on the TWICE instrument. Because the stepper motor will be used in conjunction with a gearbox, its output speed and torque must be converted with respect to the gear ratio. This means that the motor will need to spin at approximately 1380 RPM in order to output flange of the gearbox to rotate at 46 RPM. The minimum torque that the motor should output at this speed is approximately 0.00213 N-m. While Figure 23 does not extend out to 1380 RMP (23 RPS), it has been quoted from Lin Engineering that the 3709V-19 stepper motor should be able to provide at least 0.00706 N-m at this speed. In addition to its kinematic features, this stepper motor only consumes up to 3 W of power and has a height of 20.8 mm. Recall that with a total allocated space of 43.06 mm, up to 22.26 mm were still available for the needed gearbox. Each full step of the custom motor is precisely 0.9 degrees. Figure 23 shows a torque curve provided by Lin Engineering for the 3709V-19 stepper motor [30]. With a custom stepper motor designed, a suitable gearbox would need to be selected. As with the stepper motor, the driving parameter for the selection of the 30:1 gearbox was its vertical height. With size in mind, attention was turned to the Harmonic Drive strain wave gearboxes. The main advantage of using a Harmonic Drive gearbox with the TWICE stepper motor is that it is very compact and capable of providing high gear ratios. Strain wave gearboxes work in a different way than traditional gear assemblies. Instead of using rigid cogs with interlocking teeth, the strain wave technique utilizes flexible and rigid splines that can all be telescoped within one another. As a result, the overall size of the gearbox is greatly reduced without compromising performance [31]. The Harmonic Drive CSF-5-30-1U-CC-F 30:1 gearbox was chosen for use with the Lin Engineering stepper motor. With a vertical height of only 17 mm, approximately 5.26 mm were still available within the space allocated for the TWICE scanning mechanism.

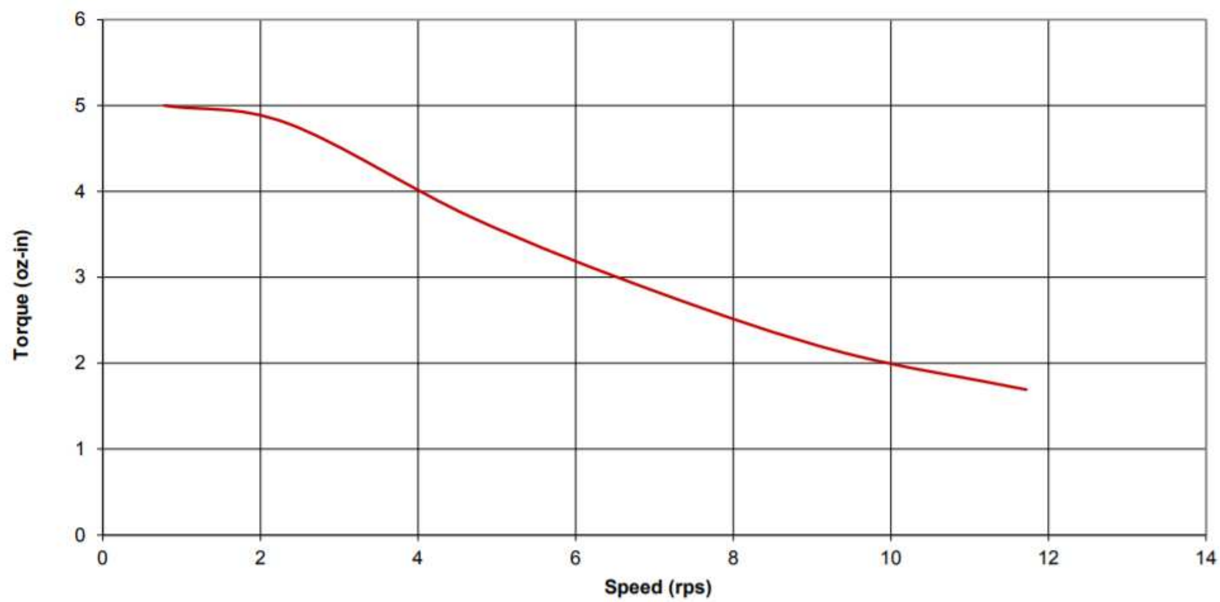

Figure 23: A torque curve provided by Lin Engineering for the 3709V-19 stepper motor, where 1 oz-in = 0.00706 N-m.

4.2.3 Design of Custom TWICE Scanning Mechanism

During the selection of the stepper motor and its accompanying gearbox, it was realized that the standard 3709V-19 stepper motor could not directly interface with the Harmonic Drive gearbox. As a solution, a custom motor shaft and an interfacing plate would need to be fabricated.

The standard 3709V-19 stepper motor comes with shaft extending approximately 20.1 mm in length from the front face of the motor. This, of course, will not work considering that the

Harmonic Drive gearbox is only 17 mm in vertical height. The diameter of the standard 3709V-19 rotor is approximately 5 mm, where the shaft input to the Harmonic Drive gearbox is only 3 mm. Lastly, the Harmonic Drive gearbox uses a set screw to anchor the motor shaft to its spline assembly. Given that the standard 3709V-19 rotor is cylindrical in shape, the effectiveness of the set screw will be diminished. To address all of the issues with the 3709V-19 motor shaft, a custom shaft was designed, shown in Figure 24.

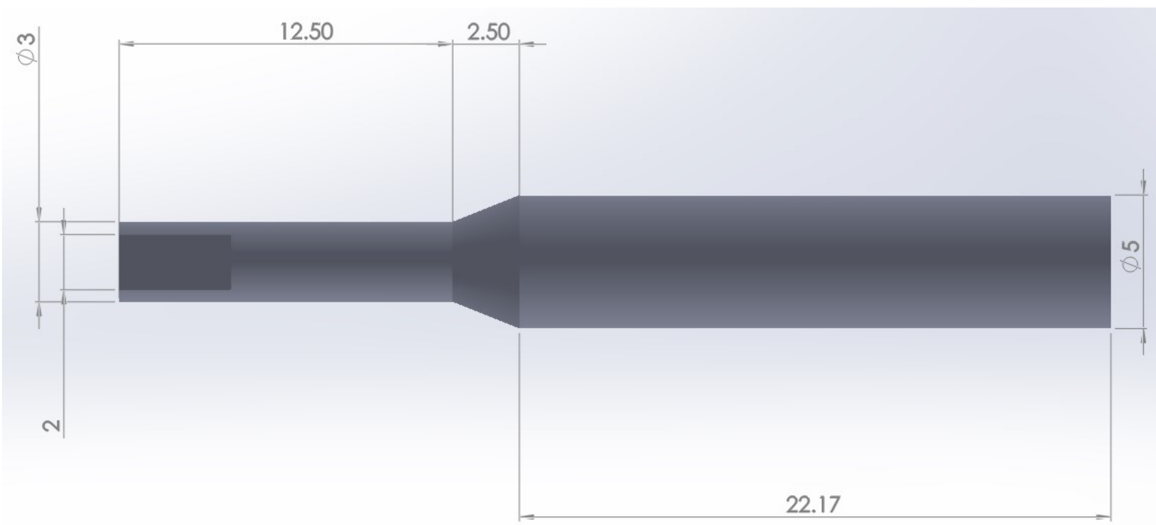

Figure 24: A CAD model of the custom motor shaft used in the 3709V-19 stepper motor. All units are in millimeters.

To accommodate the use of the Harmonic Drive gearbox, the end of the motor shaft would need to be tapered off to the correct diameter of 3 mm. However, the diameter of the rotor must be 5 mm within the motor to maintain the appropriate torque output. The tapered region, 2.5 mm long, would remain within the front face of the motor. The length of the motor shaft protruding from the front face of the motor was reduced to 12.5 mm, where it could safely be inserted in to the input flange of the Harmonic Drive gearbox. Lastly, a 2 mm wide flat face was included on the end of the custom motor shaft to allow the set screw within the Harmonic Drive gearbox to safely anchor the motor shaft to the interior spline assembly.

Interface issues still exist between the Lin Engineering stepper motor and the Harmonic Drive gearbox. As seen in Figure 25 and 26, the general size difference between the stepper motor and the gearbox prevents the two from correctly interfacing with one another. The determined solution to this issue was to design and fabricate an interface plate that would be able to hold both the stepper motor and the gearbox to a single point. The interface plate will need to contain the protruding front faces of both the stepper motor and gearbox, as well as fill the space between the motor and gearbox faces. Bore holes will also need to be made within the interior face of the interface plate so that the gearbox can be fixed to it. Once the gearbox is fixed to the interface plate, the motor can then be interfaced with the gearbox and attached to the interface plate.

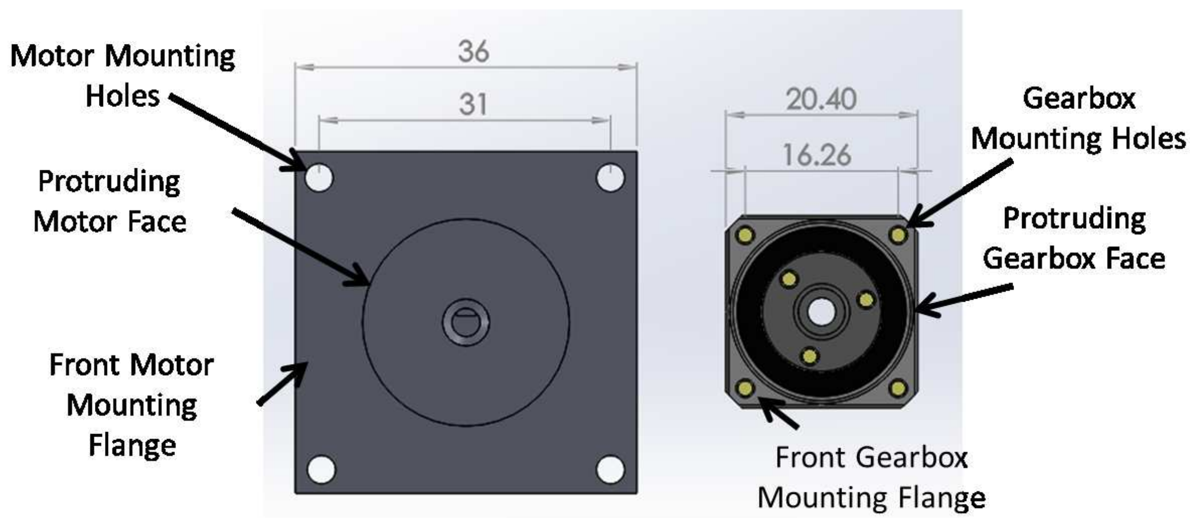

Figure 25: CAD Models of the Harmonic Drive gearbox and the Lin Engineering stepper motor.

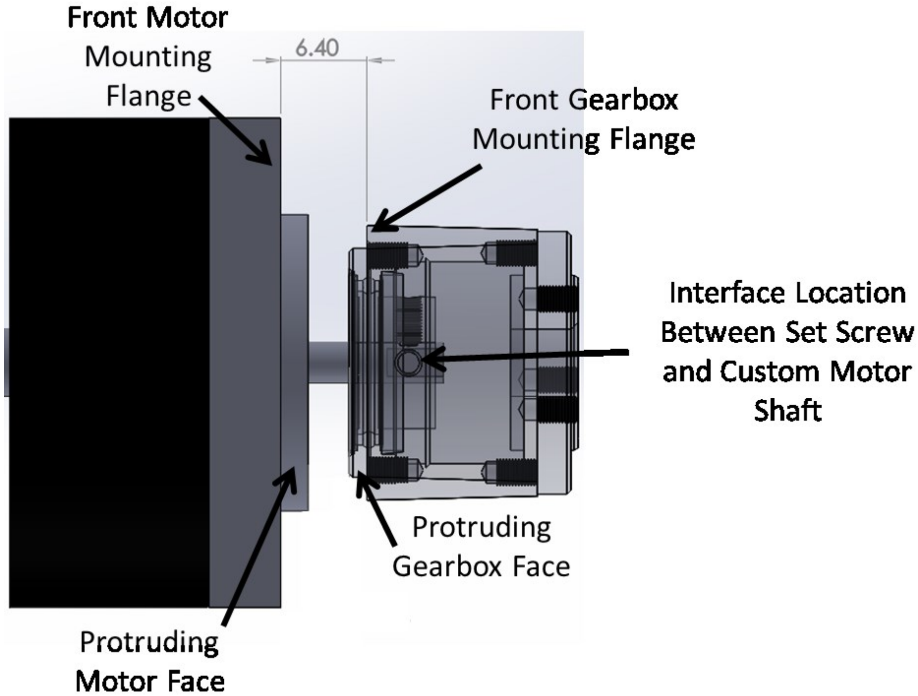

Figure 26: CAD Models of the Harmonic Drive gearbox and the Lin Engineering stepper motor. The size difference and location of mounting holes prevents the two mechanisms from correctly working together.

The stepper motor mounting holes are 3 mm in diameter, whereas the gearbox mounting holes are only 2.3 mm in diameter. The diameter of the protruding motor face is 22 mm and that of the gearbox protruding face is 17 mm. In its ideal configuration, that is where the flat face of the custom shaft is collocated with the set screw of the gearbox, distance between mounting faces is 6.4 mm. The structural design of the plate used to interface the stepper motor and gearbox is shown in Figure 27. The interfacing plate was made with counter bores so that the front mounting flange of the motor could sit flush with the motor side face of the plate. Counter bores around the gearbox mounting holes allow the screws used for fixing the gearbox to the interfacing plate to sit below the bottom of the protruding motor face counter bore. These counter bores ensure that both the front mounting flange of the motor and the gearbox are able to sit entirely flush against either face of the interfacing plate.

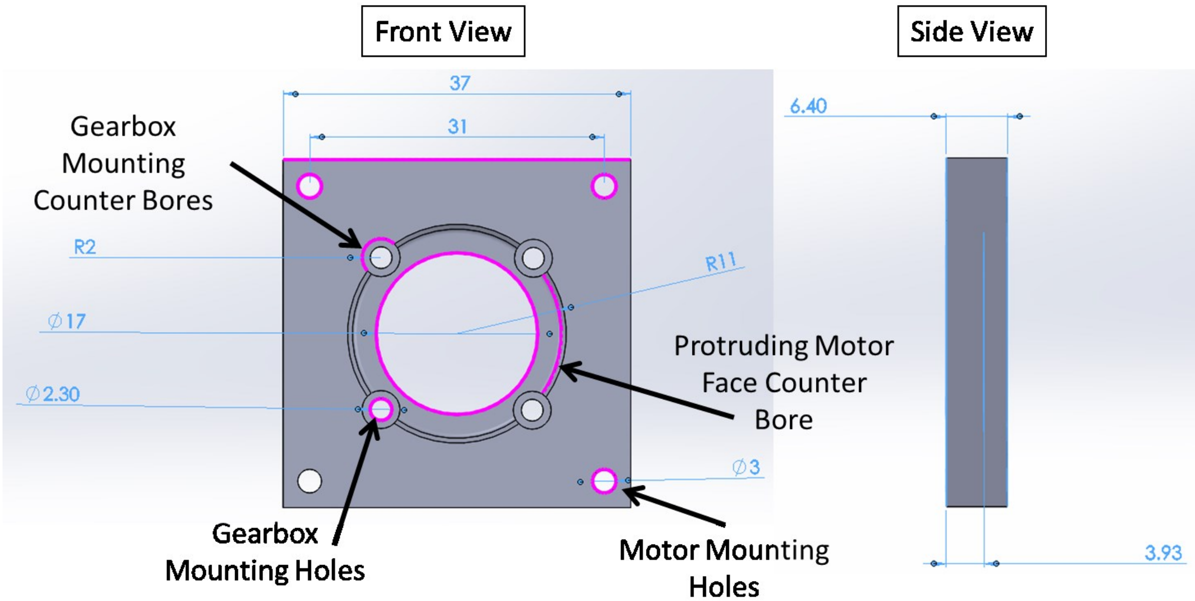

Figure 27: A CAD Model of the plate used to interface the Lin Engineering stepper motor and the Harmonic Drive gearbox.

Upon receiving all of the needed parts for the scanning mechanism, custom stepper motor, gearbox, and a fabricated interfacing plate, assembly could begin. Assembly of the scanning mechanism is simple; however, it must be done in a particular way to ensure a proper interface between the stepper motor and the gearbox. First, the front mounting flange of the gearbox must be mounted to the bottom flange of the interfacing plate, seen in Figure 28. Note that in Figure 28 only the spline assembly of the Harmonic Drive gearbox is mounted to the interfacing plate. The strain wave generating portion of the gearbox is mounted to the custom shaft of the stepper motor with the internal set screw, seen in Figure 29.

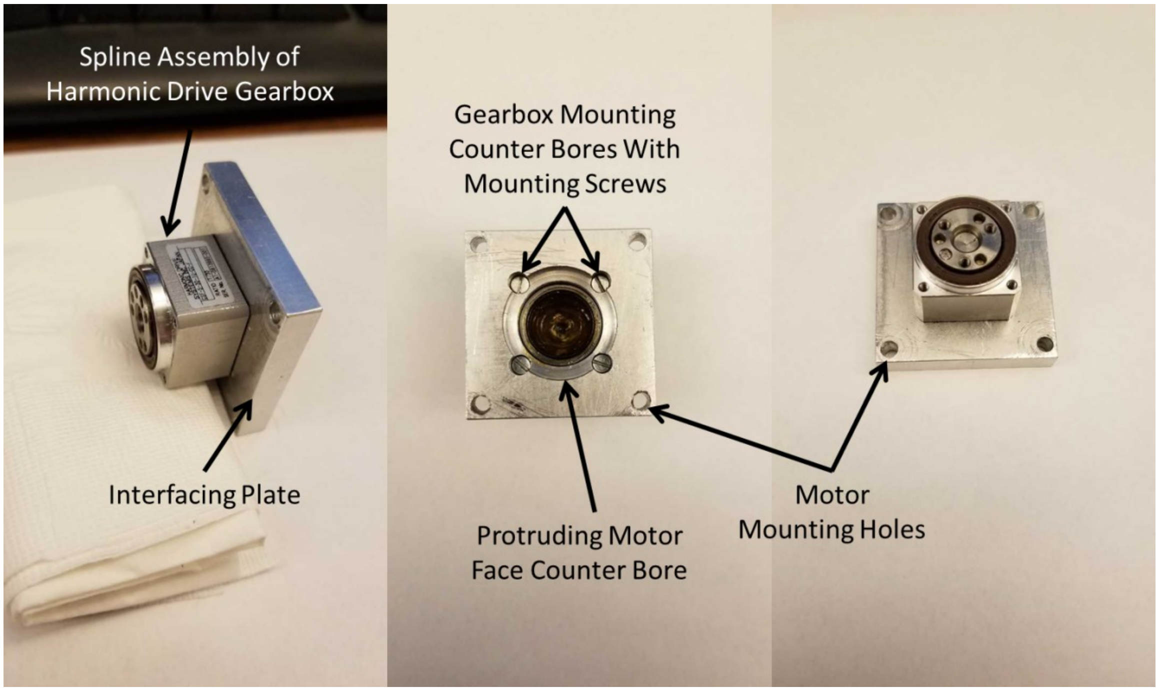

Figure 28: Pictures showing the mounting configuration of the Harmonic Drive gearbox with the interfacing plate.

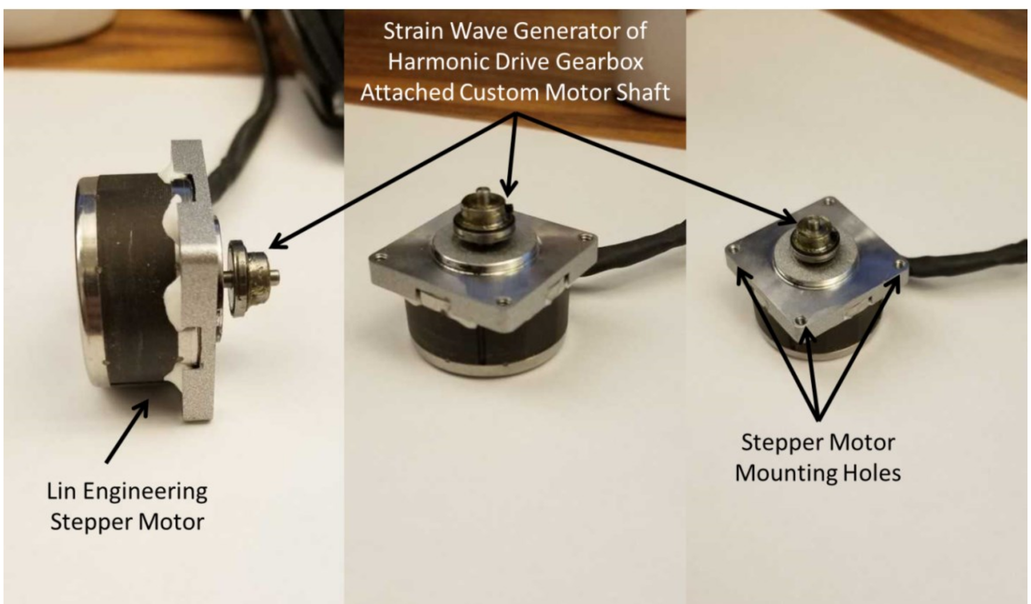

Figure 29: Pictures showing the assembly of the Harmonic Drive strain wave generator with the custom shaft of the Lin Engineering stepper motor.

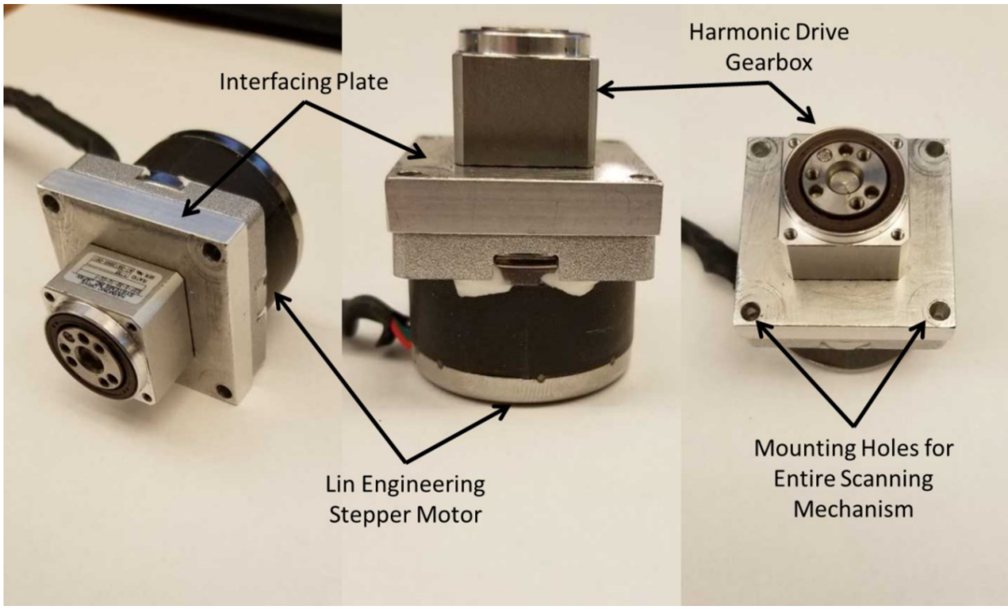

Figure 30: Pictures showing the final assembly of the TWICE scanning mechanism.

With strain wave generator fixed to the custom motor shaft, the two parts of the whole TWICE scanning mechanism can be attached together. The final motor and gear box assembly, with the interfacing plate is shown in Figure 30. The strain wave generator of the Harmonic Drive gearbox can be taken in and out of the spline assembly when needed. However, it should be noted that removing the strain wave generator from the spline assembly reduces the amount of grease inside of the Harmonic Drive gearbox, and should be avoided if possible. Because of the relatively loose connection between the strain wave generator and the spline assembly, it is possible for grease to leak out of the gearbox during operation. While this will not be a problem for a spaceborne mission, it can pose a risk during benchtop testing or flight campaigns.

4.3 Design and Testing of the TWICE Scanning System

The advantageous nature of using a stepper motor as part of the TWICE scanning mechanism allows the scanning system to operate without an encoder. Where an encoder would traditionally collect scan position data, the TWICE scanning mechanism makes use of the stepper motor's discretized steps to calculate the motors position. By knowing how many step pulses are sent to the motor driver, as well as the speed at which they are sent, combined with knowledge of individual step size, the positon of the scanning TWICE instrument can be known at all times.

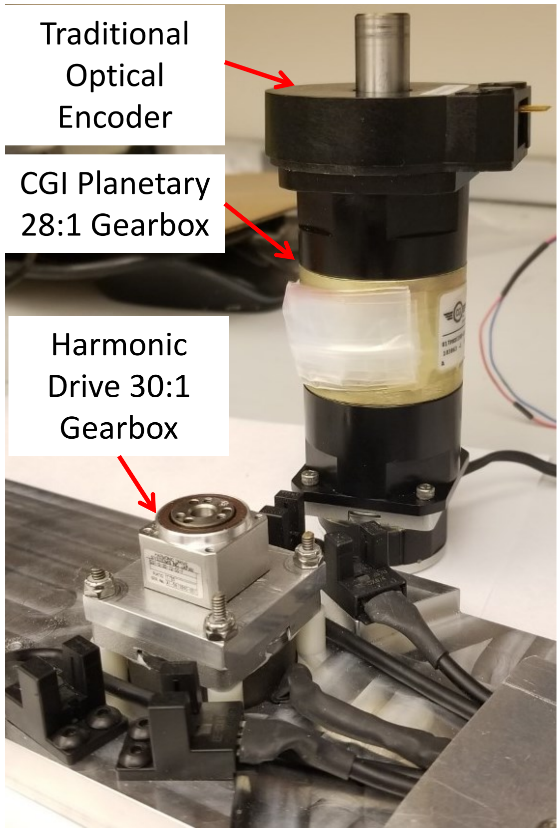

Figure 31: Pictures showing a size comparison between the TWICE scanning system and a traditional planetary gearbox and optical encoder system.

To test how well the position calculation strategy works compared to a traditional encoder, an experiment with the TWICE stepper motor was designed. In this experiment, the TWICE stepper motor was integrated with a traditional 28:1 planetary gearbox with an encoder fixed to its output flange, shown In Figure 31 and Figure 32. This experiment was designed to mimic the inertial conditions of the TWICE scanning instrument. A load disk was fabricated with approximately the same MoI as the TWICE scanning instrument. A 28:1 gearbox was selected to mimic the gear ratio used in the final TWICE scanning mechanism. Note the size comparison shown in Figure 31. The combination of a common planetary gearbox with a traditional encoder is much larger in vertical height than what is allocated for the TWICE scanning system. Note that the encoder used for comparison is fixed to the output flange of the planetary gear box. Placing the encoder in this position provides the best position accuracy of the MoI equivalent load.

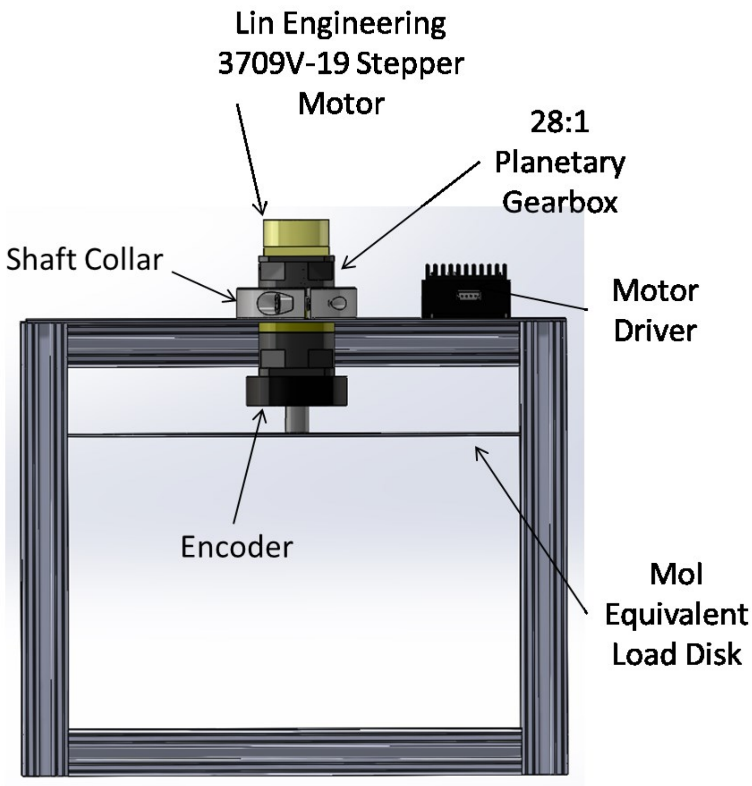

Figure 32: An illustration of the test set up used to compare calculated motor position with position measured by a traditional encoder.

The experiment would be performed as follows. The motor and gearbox assembly would operate so that it scans the load disk back and forth as intended in the final TWICE scanning design. Position data of the disk would be collected from the encoder, while at the same time position data would be calculated by way of step data from the microcontroller controlling the stepper motor. A comparison between the encoder position data and the calculated position data are shown in Figure 33. Figure 33 is made up of 2 different sections, where each section is made up of 3 parts. Section one, shown to the left of the plot represents a full scan from the beginning of the scan, through 200 degrees to the end of the scan. The end of the scan for section one is marked with the "Direction Change" label. As can be seen, the first and last 40 degrees of the scan are dedicated to acceleration and deceleration respectively. Between acceleration and deceleration is a part designated for constant velocity. At the top of this plot, or where the "Direction Change" occurs, the motor then performs another full scan, this time from the 200 degree mark back to zero. In the second section of the scan, the acceleration and deceleration parts happen in reverse. From the figure, it is easy to see that the difference between encoder measured position and the step calculated position is minimal. For a closer look, consider Figure 34.

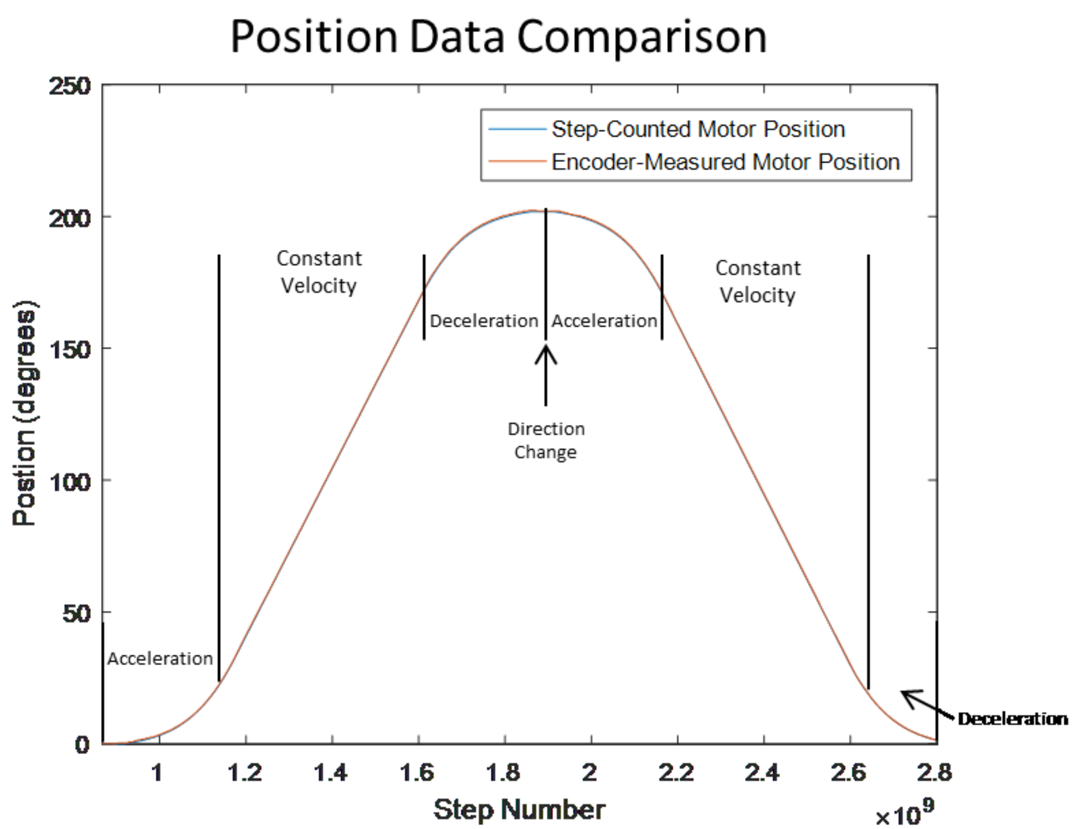

Figure 33: A Plot comparing the position data collection techniques between a traditional encoder and by way motor step computation.

Figure 34 shows the difference between the encoder measured position and the step calculated position for each point during both full scans, i.e. from 0 degrees to 200 degrees and 200 degrees to 0 degrees.

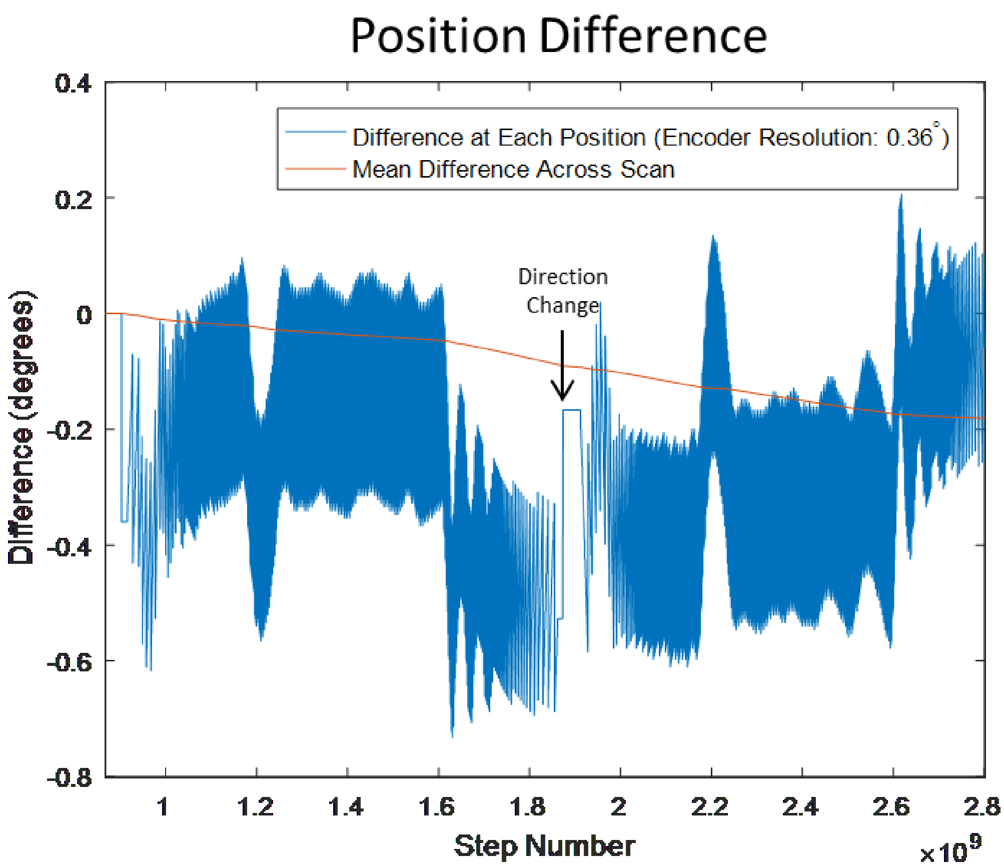

Figure 34: A Plot comparing the position data collection techniques between a traditional encoder and by way motor step computation.

It is obvious that during times of acceleration and deceleration, the magnitude of the position difference grows to unacceptable values, approximately 0.75 degrees. However, during the constant velocity portion of the scan, the position difference does not change much on average. Analyzing the average position difference over two scans, from 0 degrees to 200 degrees and 200 degrees to 0 degrees, it is seen that difference can grow up to 0.2 degrees in magnitude. Considering that a single full step of the 3709V-19 stepper motor is only as small as 0.9 degrees, it seems that an average position difference of 0.2 degrees should not be of any significance. However, note that with a 30:1 gear ratio, the actual position change per step is 0.03 degrees. It is also expected that this average position difference will grow over the course of numerus scans.

To mitigate this issue, a fixed position marker system is employed. There are 4 points along the 200 degree scan that can be routinely referenced to ensure that the calculated position of the stepper motor correctly represents the actual position of the scanning load. These positions are at the beginning and end of each scan, as well as the beginning and end of the Earth scene arc. By placing reference sensors at the beginning and end of each scan, the calculated stepper motor position can be updated to ensure that one full scan is always 200 degrees and that the beginning of each scan always starts at zero degrees. From Figure 34, it is obvious that the largest and most uncertain position difference occurs during times of acceleration and deceleration. Position differences in these zones tend to accumulate up to the point at which the constant velocity phase is reached and the scanning instrument is observing the Earth scene. Therefore, to correct any accumulated difference during times of acceleration, and to ensure that the bounds of the Earth scene are always known, position sensors are placed at the beginning and end of the Earth scene arc. The locations of the position sensors can be seen in Figure 35.

In words, the algorithm for correcting differences between the calculated stepper motor position and the actual scanning load position is as follows. At the beginning of a single scan, the position sensor 1 (Figure 35) will be tripped resetting the current position calculation to zero degrees by default. Upon accelerating through the 40 degree acceleration arc, position sensor 2 will be tripped. Because the exact location of position sensor 2 is known, tripping the sensor will set the stepper motor calculated position to 40 degrees. The instrument will then scan with constant velocity through the Earth scene arc until it trips position sensor 3. Position sensor 3 is placed at exactly 120 degrees from the being of the scan and marks the end of the Earth scene arc. While the accumulation of position difference is minimal during the constant velocity phase of the scan, the position 3 sensor will reset the current calculated motor position to 120 degrees. From this point, the motor will be decelerating until it reaches position sensor 4. Upon reaching position sensor 4 all of the scanning instruments motion will be stopped. From here, the motor will be instructed to change direction and begin the exact same process in the opposite direction. However, upon changing direction, the function of each position sensor is flipped.

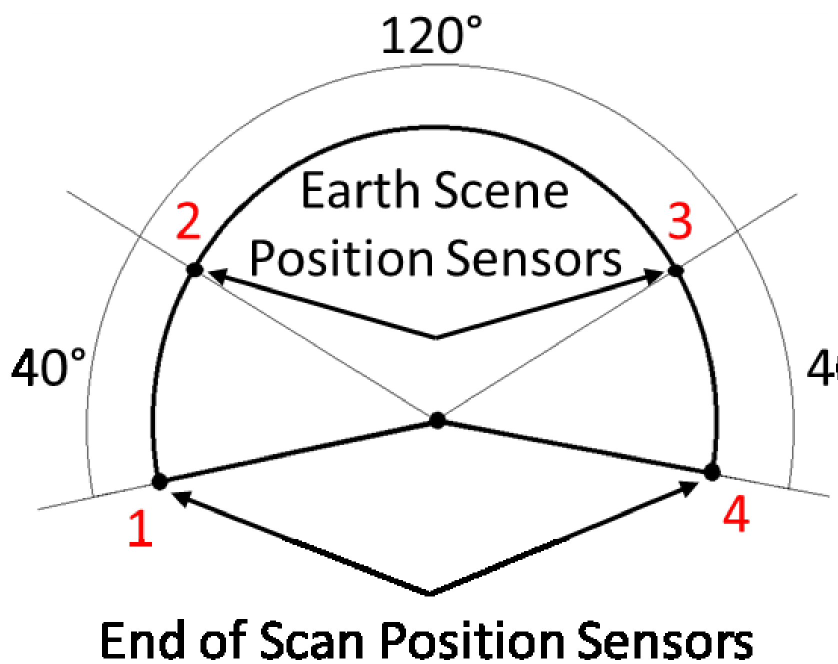

Figure 35: An illustration of where each position sensor is placed along the TWICE scan.

Figure 36 shows an example of the position sensor strategy in use. As seen in the figure, the amount of position error accumulated over the course of several scans can grow to as much as 0.6 degrees in magnitude, with as much as 1 degree of spread between individual scans. This amount of uncertainty can be problematic during data analysis and geolocation. However, by utilizing the Earth scene position sensors the amount of position difference, and difference spread, is greatly reduced. From the experiment performed in Figure 34, the amount of position difference experienced only grows to as large as 0.2 degrees, with a spread on the order of 0.1 degrees, and an average position difference of 0 degrees.

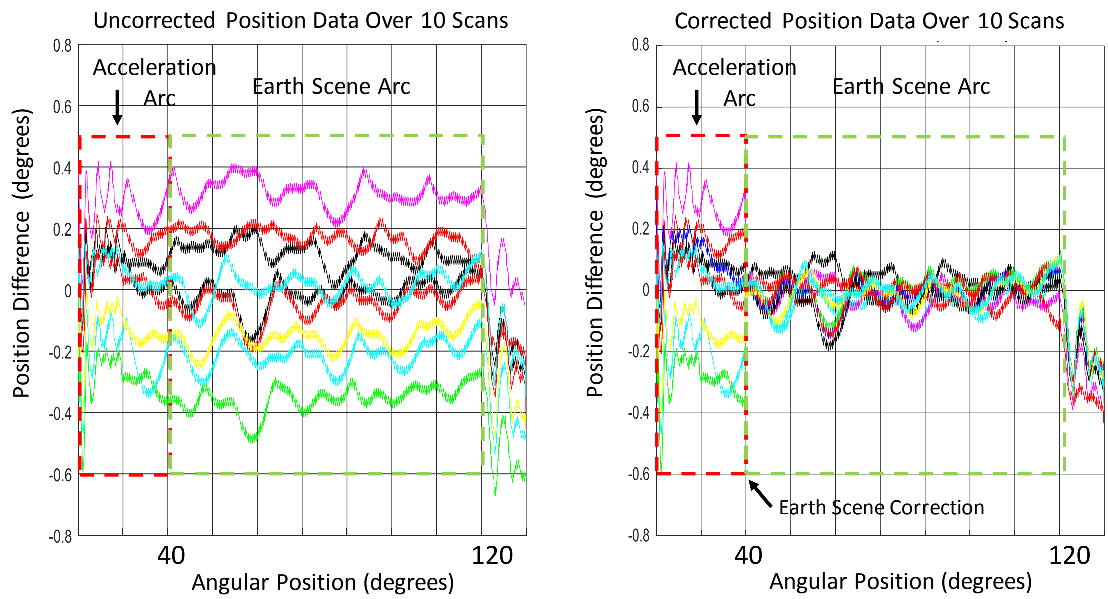

Figure 36: Performing a position calculation correction at specific points along the scan minimizes accumulated position difference.

Further analysis has been done by mapping out the position of each step along the scan and comparing expected step count values with what is calculated during nominal operation. Performing this double difference method reduces the amount of position difference during the Earth observation portion of the scan to as low as 0.03 degrees, which is on the order of a single step size after the 30:1 gearbox reduction. On the surface of the Earth a position difference of 0.03 degrees translates to approximately 0.22 km. The 850 GHz radiometer creates the smallest cross track footprint on the Earth's surface at 3.1 km. It is noted that the position difference detected during nominal operation will not affect the accuracy of footprint position.

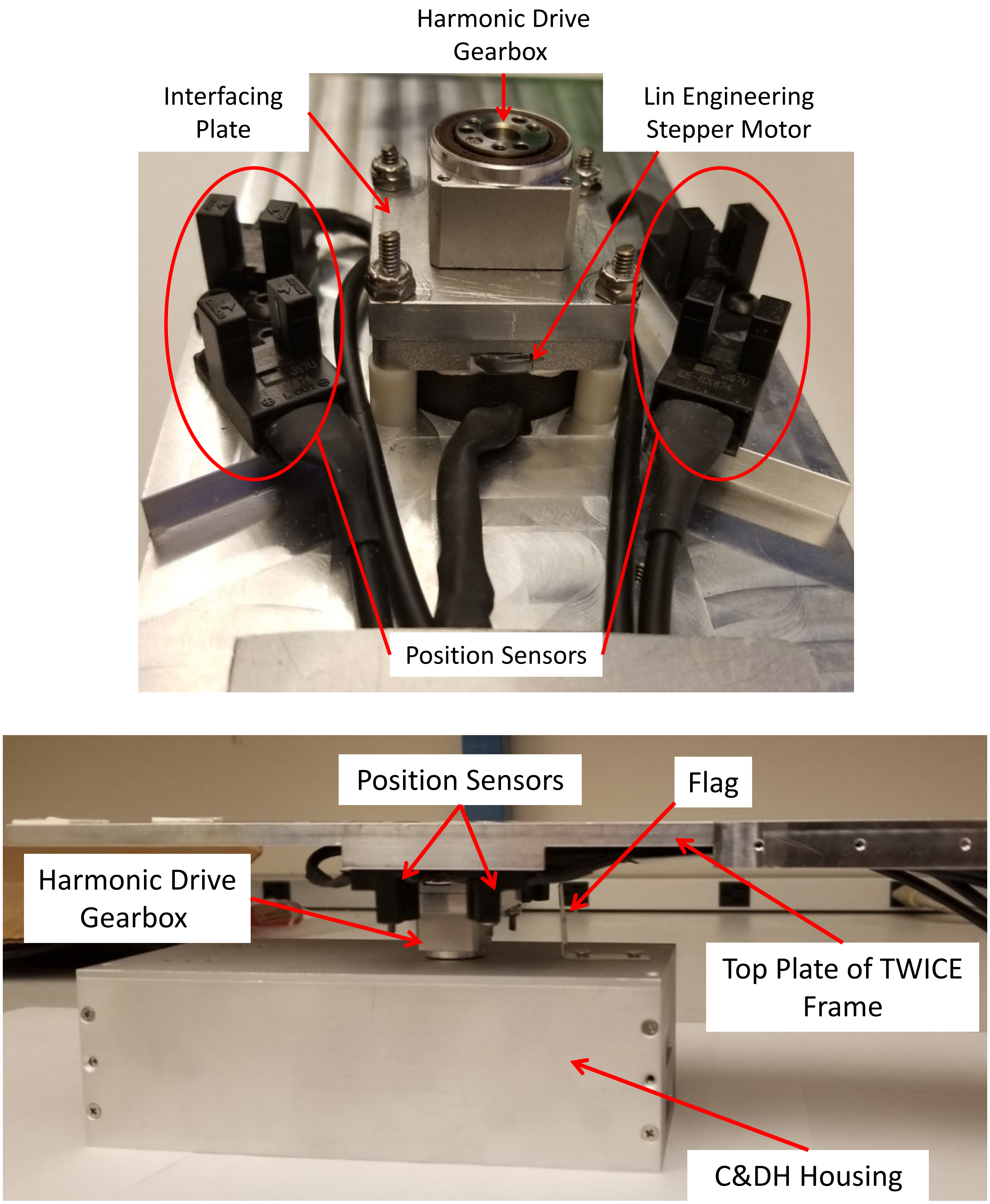

Figure 37: Assembly of the final TWICE scanning system.

Mechanically, the implementation of the position sensor system is straight forward. At each of the determined points, positions 1 through 4 in Figure 35, a simple photogate sensor can be placed. The final scanning system assembly is shown in Figure 37.

Chapter V Passive Radiometer Calibration Techniques

5.1 Calibration Methodology

Radiometers used in the TWICE instrument are considered to be linear systems, meaning that the input of the radiometer is linearly related to its output. Generally speaking, the radiometers discussed in this work consist of four major components: a low noise amplifier (LNA), a band pass filter, a detector diode, and an integrator. Different types of radiometers can build upon this configuration by including other components that help to determine the unique behavior of the four main components. When viewing an ambiguous scene, like that of the Earth's atmosphere, the radiometer instrument produces an output voltage which changes as a function of the observed radiated energy. The ultimate goal of calibration is to characterize a radiometer so that a measured output voltage can be interpreted into a known observation scene. As will be discussed, calibration also plays a very important role in minimizing the effect of instabilities in the system. Without calibration, data received from a radiometer would be largely unreliable for scientific analysis. Radiometer calibration can take many different forms, and can be performed both inside and outside of the instrument itself. In particular, TWICE uses an external, end-to-end calibration strategy that will be discussed in further detail later in this chapter.

Radiometric calibration can be performed in many different ways. The most fundamental categories of calibration are considered to be internal and external. Both internal and external calibration requires two known points of reference. As mentioned in previous sections, these known points are typically known as "hot" loads and "cold" loads. The main difference between internal and external calibration is how and where the different calibration points are acquired. In the following sections internal and external calibration will be briefly discussed. It is very important to note that the derivations given in this section are made with the Rayleigh – Jeans approximation. The radiometers discussed in this section utilize a squared-law detector diode, which allow the output voltage to be linear to the input power of the radiometer system. Thus, by way of this approximation, the resulting formulations may not necessarily be applicable in all contexts. A more general approach to the radiometer transfer equation and a discussion on the inaccuracies of the Rayleigh – Jeans approximation will be given in a later section.

5.1.1 Internal Calibration

Internal calibration is achieved by making use of a known noise source within the radiometer itself. For example, Dicke switching or noise injection radiometers can be considered internally calibrated systems. Internal calibration can prove to be more precise than external calibration, however, at a price of increasing the number of assumptions in the calibration process. In general, internally calibrated systems exclude many critical parts of a radiometer system.

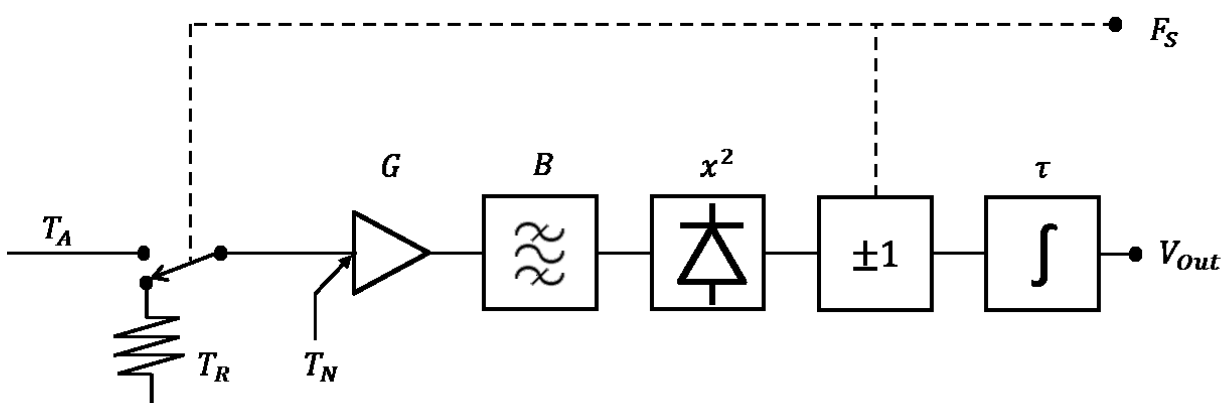

Figure 38: A block diagram of an internally calibrated Dicke Switching radiometer.

In Figure 38 a block diagram of an internally calibrated Dicke switching radiometer is shown. Notice that the calibration source for the radiometer takes placed behind the antenna. This means that the radiometer antenna, along with any optics required to focus the scene into the antenna, cannot be directly measured. Exterior parts of a radiometer system can be determined mathematically, however, such a method will require many assumptions. An example of an internally calibrated radiometer can be found in the High Frequency Airborne Microwave and Millimeter-Wave Radiometer (HAMMR) instrument. Note, however, that HAMMR utilizes a noise injection technique in addition to a Dicke switching radiometer [32]. As discussed, a Dicke switching radiometer periodically references a known resistive load while it operates. The noise temperature of this resistive load can be calculated by the following equation.

$$P = kT_R B \tag{V.1}$$

Where P is the power produced by the resistive load, k is Boltzmann's Constant, and B is the bandwidth of the band pass filter. Solving this simple relation for T_R will allow one to determine the expected noise temperature to be detected from the Dicke switching reference load at the output of the radiometer. Once the noise temperature of the reference load is known a relationship can be derived that determines the expected output from the radiometer. Consider the following equations.

$$V_1 = G(T_A + T_N) \tag{V.2}$$

$$V_2 = -G(T_R + T_N) \tag{V.3}$$

Where V_1 and V_2 are the output voltages when the Dicke switching is observing the antenna and the reference load respectively, G is the gain of the entire radiometer system, T_A is the noise temperature of the antenna, T_R is the noise temperature of the reference load, and T_N is the arbitrary noise temperature acquired throughout the radiometer. Note that the reason Equation V.3 has a negative sign is due to the architecture of a Dicke switching radiometer. Adding these equations together will eliminate T_N.

$$V_{out} = V_1 + V_2 = G(T_A - T_R) \tag{V.4}$$

While the Dicke switching will allow one to remove the arbitrary noise accumulated from the internal radiometer components, it does not allow one to determine the antenna noise temperature T_A. Noise injection sources, like that used in HAMMR, can help one determine the antenna noise temperature. In the case of HAMMR, the noise source is produced by a noise diode. For a more in depth look at the noise injection strategy used in HAMMR see [32].

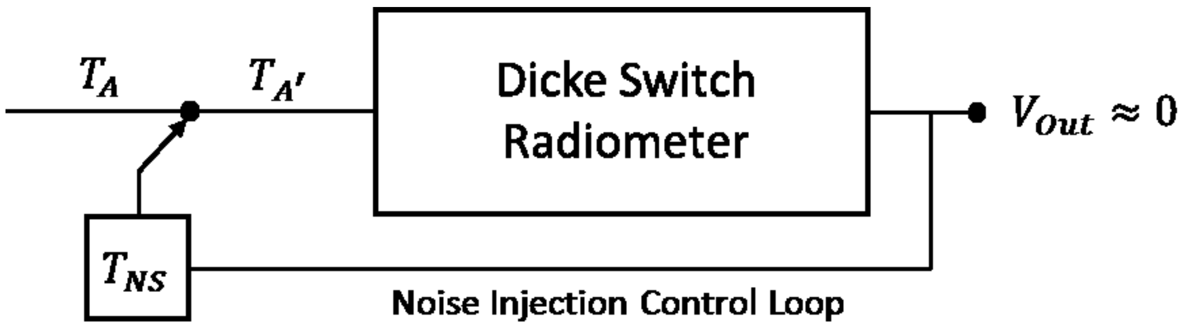

Figure 39: A noise injection radiometer is the same as a Dicke Switching radiometer, however, with the addition of a noise injection system.

Consider the block diagram shown in Figure 39. The noise injection radiometer is an advanced type of Dicke switching radiometer where a noise diode connected to control loop is inserted into the design. This control loop monitors the incoming antenna noise temperature and adjusts the output of the noise diode so that the output voltage is always approximately zero. Given this configuration, the following relations can be made.

$$V_{out} = G(T_{A'} - T_R) \tag{V.5}$$

Where,

$$T_{A'} = T_A + T_{NS} \tag{V.6}$$

T_A is again the noise temperature of the antenna, and T_{NS} is the noise temperature of the noise diode. The function of the noise injection radiometer is to determine the antenna temperature by way of minimizing the output of the radiometer. The control loop used in this radiometer technique will adjust the noise temperature of the noise diode so that the output of the radiometer is always approximately zero. Thus, the following can then be shown.

$$V_{out} = G(T_{A'} - T_R) = 0 \tag{V.7}$$

Plugging in $T_{A'}$,

$$G(T_A + T_{NS} - T_R) = 0 \tag{V.8}$$

Therefore,

$$T_A = T_R - T_{NS} \tag{V.9}$$

The antenna noise temperature can be mathematically determined, and ultimately an estimation for the total radiometer gain, G, can also be made. Internally calibrated radiometers are convenient in the fact that the calibration mechanisms can be built into the radiometer itself. However, this convenience comes at the price of precision in the calibration process. Because the antenna noise temperature must be calculated, the behavior of the antenna cannot be exactly known. The same holds true for any exterior parts that are involved in translating the observed scene to the radiometer. While it is not uncommon to assume that the materials used in the optics of a radiometer system are almost perfectly reflective, i.e. their emissivity is almost zero, it may not always hold true given the context in which the radiometer will be used. Internal calibration also reduces the radiometers sensitivity. Reducing the sensitivity, or resolution, of a radiometer means that it will lessen the ability of the radiometer to detect small changes in the observed scene. The following is a derivation of the radiometric resolution of a Dicke switching or a noise injection radiometer. The following relationships give the radiometric resolution with respect to the observed scene or known noise source. Note that there is temperature uncertainty for both the antenna noise temperature and the reference load noise temperature.

$$NE\Delta T_1 = \frac{T_A + T_N}{\sqrt{B\frac{\tau}{2}}} \tag{V.10}$$

$$NE\Delta T_2 = \frac{T_R + T_N}{\sqrt{B\frac{\tau}{2}}} \tag{V.11}$$

In Equations V.10 and V.11, all variables are the same, and τ is the integration time of the integrator. It is important to notice that for a Dicke switching or noise injection radiometer the integration time is divided by a factor of 2. This is due to the architecture of the Dicke switching system, where the Dicke switching radiometer separates its integration process between both the observed scene and the reference load. By way of the basic principles of uncertainty analysis, these two relationships are added in quadrature. In doing so, the total uncertainty becomes the following.

$$\Delta T = \sqrt{\frac{2(T_A + T_N)^2 + 2(T_R + T_N)^2}{B\tau}} \tag{V.12}$$

T_R is can be chosen to be approximately the same magnitude as the expected temperature of the antenna, T_A, therefore the reference noise temperature and the antenna noise temperature can be interchanged with each other. Replacing T_R with T_A gives,

$$NE\Delta T = 2\frac{T_A + T_N}{\sqrt{B\tau}} \tag{V.13}$$

The resolution of a noise injection radiometer can be found by simply replacing T_A with $T_{A'}$ [33].

5.1.2 External Calibration

Unlike that of internal calibration, external calibration takes place entirely outside of the radiometer. This type of calibration requires a different set of parameters and techniques than internal calibration. One type of radiometer that exclusively requires external calibration is known as total power radiometer. A total power radiometer, seen in Figure 40, contains only the four main components needed for a radiometer. The TWICE radiometer instrument makes use of total power radiometers for all of its channels. Total power radiometers, like those used in TWICE, do not have any systems in place to preform internal calibration, therefore requiring them to be calibrated by external means. Even radiometers designed to have the ability to internally calibrate also make use of external calibration to fully characterize the instrument. For instance, TWICE and HAMMR use external calibration, however, HAMMR uses external calibration in addition to internal calibration.

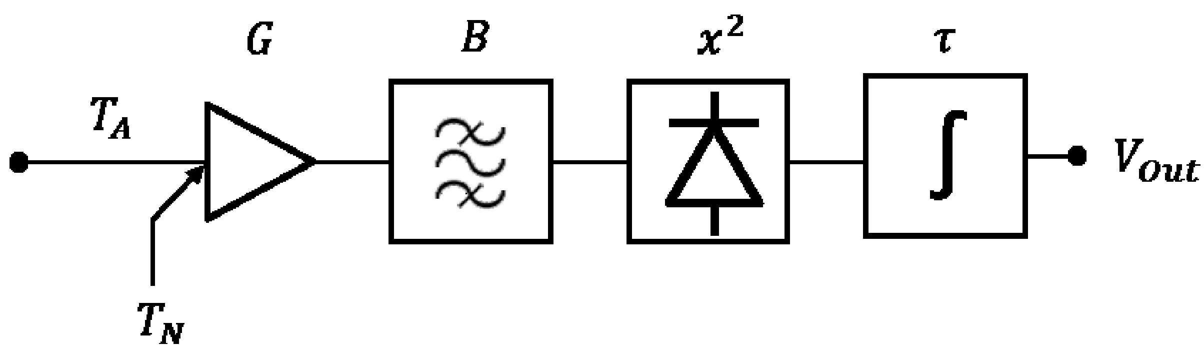

Figure 40: A total power radiometer only makes use of the 4 main radiometer components: a LNA, a band pass filter, a detector diode (squared law for this case), and an integrator.

Consider a slightly modified version of Equation V.2.

$$V_{Out} = G(T_A + T_N) \tag{V.14}$$

Where T_A is the antenna temperature, G is the gain of the radiometer system, V_{Out} is the output of the radiometer as measured in voltage or counts, and T_N is the system noise temperature of the radiometer system. Unlike a Dicke switching or noise injection radiometer, a total power radiometer has no way of determining its antenna noise temperature, system temperature, or radiometer gain on its own. Luckily, due to the linearity of a radiometer, an external two point system can be used to determine, or extrapolate, many unknown parameters. In general, external calibration consists of 2 individual and well characterized targets for total power radiometers to observe. It is best practice to utilize two targets that are as far apart in temperature as possible, creating a “cold” and “hot” target, where the temperature of the scene of interest, say the Earth’s atmosphere, falls within these two temperatures. This is illustrated in Figure 41. It should be noted that the temperature different between the “cold” and “hot” target should be as large as possible. Observations that lay outside the range of temperatures used for calibration are subject larger uncertainties than observations that fall within this range. It is understood that the antenna noise temperature of the radiometer is equal to the brightness temperature of the scene the radiometer is observing. If one is able to characterize the temperature of the targets the total power radiometer will observe, they will be able to safely assume that the antenna temperature of the radiometer is equal to the brightness temperature of the target. As a result, the radiometer system will have a known input and a known output for two unique points, leaving only the system noise temperature and the total radiometer gain as unknowns.

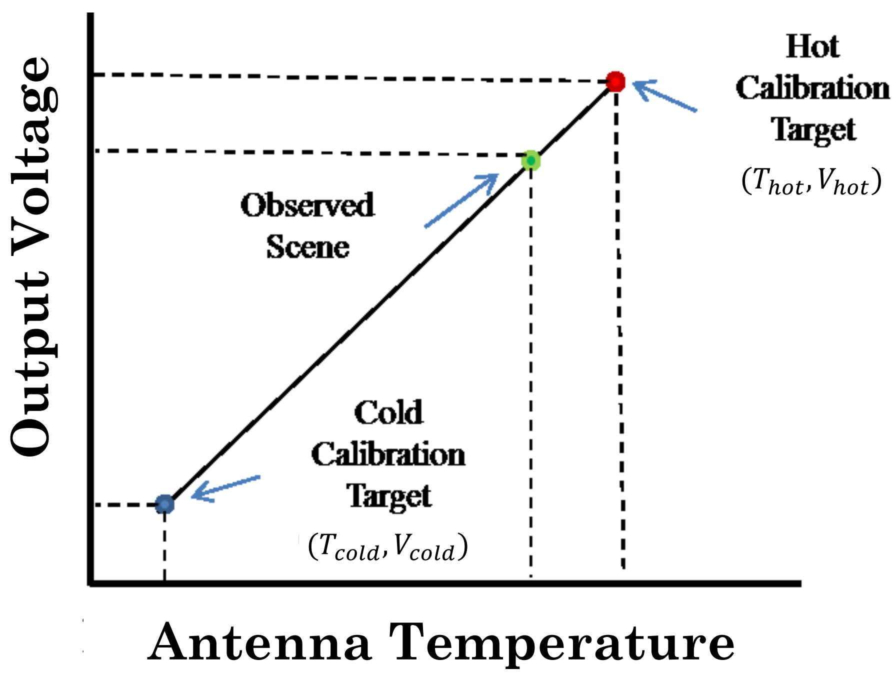

Figure 41: An illustration of the external calibration technique.

With two unique equations, one can solve for the two unknowns. System noise temperature and total radiometer gain can be solved, and are shown in Equations V.15 and V.16.

$$T_N = \frac{V_{cold}T_{hot} - V_{hot}T_{cold}}{V_{hot} - V_{cold}} \tag{V.15}$$

$$G = \frac{V_{hot} - V_{cold}}{T_{hot} - T_{cold}} \tag{V.16}$$

Where T_{hot} and T_{cold} represent the hot and cold antenna temperatures respectively, and V_{hot} and V_{cold} represent the radiometric output of the cold and hot antenna temperatures respectively. Once the total radiometer gain and system noise temperature have been calculated, one can simply draw a line between the cold and hot calibration points, shown in Figure 41. When viewing an arbitrary scene, all the total power radiometer is able to produce is an output voltage. However, with this known output voltage, one can utilize the linear radiometer calibration curve to obtain an antenna temperature. Again, because the antenna temperature is the same as the brightness temperature of the scene being observed, brightness temperature can be directly measured given an output voltage from the radiometer.

External calibration is, in theory, simpler than internal calibration. However, in practice external calibration is more difficult. External calibration generally requires the use of moving parts within the instrument system in order to observe the two different targets. This type of calibration also requires a very good knowledge of the temperature and radiation characteristics of the calibration targets, as well as the directivity characteristics of each radiometer utilizing this calibration strategy. Monitoring these variables can be a difficult task, especially on a CubeSat where power and space is at a premium. For space born missions, the cosmic microwave background (CMB) is often used as the "cold" target. The CMB is a very stable and well understood scene, decreasing the amount of uncertainty of the "cold" target. However, the "hot" calibration target is almost always made up of some kind of radio absorbing material (RAM). This RAM can be made into any kind of complex geometry to accommodate the restrictions of the radiometer instrument, however, its thermal characteristics are difficult to track. The temperature and emissivity of a RAM must be known in order to perform calibration. The emissivity of a RAM can be determined before the start of a campaign or mission, but the temperature of the RAM will generally fluctuate, and requires constant monitoring.

Although the mechanical complexity of an externally calibrated radiometer system is greatly increased, i.e. scanning over calibration targets or temperature monitoring of the calibration targets, it comes with the advantage of increased radiometer resolution. Recall that for internally calibrated radiometers that the integration time, or time in which the radiometer is observing a pixel, is divided between the scene of interest and a reference load. For an externally calibrated system, the radiometer is always observing the scene of interest. As a result, the resolution of an externally calibrated, total power radiometer is twice that of an internally calibrated system, as seen in Equation V.17.

$$NE\Delta T = \frac{T_A + T_N}{\sqrt{B\tau}} \tag{V.17}$$

It is also very important to note that an externally calibrated system is able to calibrate all of the systems and optics required to propagate the observed radiation into the radiometers. For an internally calibrated system, it is either assumed that the optics of the radiometer instrument are perfectly reflective, or other mathematical means are needed in order to characterize the effect of the optics on the observed radiation [33].

5.1.3 Direct Detection and Heterodyne Radiometers

It is worth discussing the two most common radiometer types used in practice: direct detection radiometers and heterodyne radiometers. These two types of radiometers come with a specific set of advantages and disadvantages, and are generally different in design. However, both types abide by the aforementioned theory presented in the last two sections. That is to say both a direct detection and a heterodyne radiometer can operate with any one type of calibration method shown in the last sections. For the sake of clarity, all of the block diagrams shown in the previous sections depict a direct detection radiometer. A direct detection radiometer is a type of receiver that directly detects the incoming radiation at the frequency the radiometer channel is designed for. As an example, the TWICE radiometer utilizes a 670 GHz direct detection receiver. The radiance that is detected by the antenna, at approximately 670 GHz, is transferred through the amplifiers and bandpass filters to the detector diode and finally to the integrator. This means that the frequency of the radiance received by the radiometer antenna does not change through the radiometer system, i.e. it directly detects the 670 GHz signal. These types of radiometers are useful for the fact that they are generally low power and can be made relatively small. However, it comes at a price of increased noise temperature, stability, and a degradation of filtering at high frequencies.

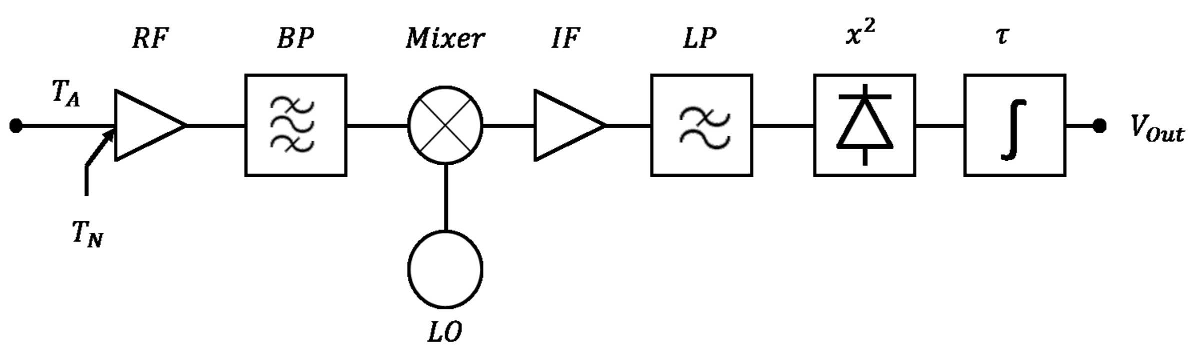

Figure 42: A block diagram of a total power heterodyne radiometer system.

A heterodyne radiometer adds a few extra components to the direct detection system. The term heterodyne means to mix with a lower frequency, thus the inclusion of an local oscillator (LO) and a mixer into a radiometer system is the key characteristic of a heterodyne radiometer. A block diagram of a heterodyne radiometer is scene in Figure 42. The similarity of the heterodyne radiometer to that of the direction detection radiometer should be noted. However, instead of directly detecting the radiation observed, the heterodyne chain will first amplify and filter the directly detected radiation before sending it to a mixer. The mixer, in conjunction with the local oscillator, will down shift the frequency of the observed radiation to an intermediate (IF) frequency, where it will again be amplified and filtered, and then be sent to the detector diode and the integrator. Some of the main advantages of using a heterodyne radiometer system include that it is easier to build components for IF than it is for the directly detected RF. In particular, filtering is easier and more precise at lower frequencies. This is important when considering atmospheric sounding, where a large enough uncertainty in filtering can lead to drastically different atmospheric profiles.

Chapter VI The TWICE Calibration Subsystem

6.1 The TWICE Calibration Strategy

TWICE uses three total power, direct detection radiometers. As was discussed in the previous chapter, the architecture of a total power radiometer requires that TWICE perform external calibration. In the case of TWICE, the two calibration targets used are referred to as the "hot" target, or the ambient calibration target, and the "cold" target, or the CMB reflector, where "hot" and "cold" are defined with respect to each other. The CMB reflector is, as its name suggests, a polished metallic surface that is can reflect electromagnetic radiation, in particular the radiation from the CMB. One can reference Figure 12, in Chapter III for a general diagram of the TWICE system. Because TWICE makes use of external calibration, it has the capability to calibrate all of the components outside of the radiometers themselves. In particular, the external calibration strategy used in TWICE calibrates both of the reflectors used to focus a scene into the radiometers. This type of calibration can be referred to as end-to-end, external calibration, where end-to-end refers to the idea that every optical component used between the scene of interest and the radiometers is accounted for in the calibration process, externally and internally.

The two targets TWICE used for its external calibration are placed so that they maximize the Earth observation arc. The calibration targets are placed to either side of the TWICE spacecraft chassis, where the instrument will periodically scan over the top of each target once every second. At each one second scan TWICE will make a measurement of one calibration target and then continue to move through the rest the scanning arc until it reaches the end of its scan, where it will measure the other calibration target. During a continuous operation mode, both calibration targets will have 8° of scan arc (4° at the beginning of one complete oscillation and 4° and the end of one complete oscillation) to take calibration measurements. During this section of the scan, the radiometer instrument will be accelerating, which will not affect the overall calibration, but will nontrivially affect the number of measurements the instrument can take during the calibration view. The time allocated for view of the calibration targets is determined by the acceleration profile of the scanning system, discussed in Chapter III.

6.2 Radio Absorbing Materials

Radio Absorbing Materials (RAMs) (also called radar absorbing materials) are, in general, any material that can significantly attenuate an incident electromagnetic (EM) wave [34]. The ability of a RAM to attenuate electromagnetic radiation is very important for radiometric calibration. An ideal RAM for radiometric calibration is a perfect absorber, i.e. a material with an emissivity of 1. RAMs used in radiometry can take many different shapes and can be made up of many different materials. RAMs are largely application and frequency dependent, meaning that the material type, geometry, and absorption technique will change depending on the project. Two of the most common absorber types are resonant and free space. Resonant absorbers are often made of a thin plane of lossy material that is highly reactive to a single frequency. These types of RAMs are most useful within circuit board housings or waveguides. Free space absorbers are often used in anechoic chambers and can be utilized with either a narrow or broadband configuration. Single layer reflective type free space absorbers reflect incident radiation at calculated locations to create a reflected ray that completely destructively interferes with itself. As a result, a minimal amount of radiation is reflected from the face of the absorber. However, this often will only work for a single frequency. It possible to create a free space broad band reflective absorber, however, the complexity of such an absorber greatly increases with an increasing number of incident frequencies. To accommodate the absorption of very wide band radiation is with a free space impedance gradient type of absorber. This is the same type of RAM used by the TWICE instrument, however, it is utilized in a slightly different way so to accommodate TWICE frequencies [35].

6.3 TWICE Ambient Calibration Target Geometry and Multiple Reflection Strategy

Given the large range of operational TWICE frequencies, the ambient calibration target used with the TWICE radiometer instrument must implement a free space RAM to effectively minimize any reflections. More specifically, a pyramidal type RAM is used to both provide an impedance gradient for low frequency radiation and provide multiple reflections for high frequency radiation. In general, depending on the size and shape of the pyramids, an impedance gradient is made by creating a gradual transition from the impedance of free space to the impedance of the material. As one can recall, reflections at the interface between two media are relatively large when the impedance of the two media are very different. The impedance of a RAM is generally much different than that of free space, meaning that to ensure proper absorption at low frequencies, i.e. for wavelengths that are electrically big compared to the size of the pyramids, some sort of some transition is required. However, at higher frequencies, one is still able to take advantage of a pyramidal shaped free space absorber.

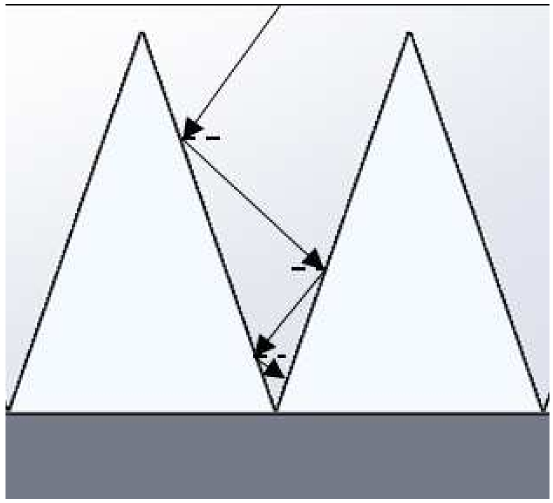

Figure 43: EM radiation with a short enough wavelength will undergo multiple reflections within the cavity between adjacent pyramids.

Consider Figure 43, which shows a ray of EM radiation reflecting multiple times between two pyramids. When a ray of EM radiation enters into the space between adjacent pyramids it will eventually encounter an interface between free space and the RAM. At this interface, the radiation will partly transition into the material, where it will be absorbed, and partly be reflected downward, deeper into the cavity between the two pyramids. The cycle of reflections deeper into the cavity will repeat numerus times, where the reflected ray will carry less and less energy. Eventually the ray will bounce its way back out, but with a greatly attenuated magnitude.

This multiple reflection concept is a large driver for the geometry of the TWICE ambient calibration target in that the pyramids must utilize dimensions that facilitate as many reflections as possible for the frequencies of interest. To meet this condition, one can consider Equation VI.1, which states that the minimum periodicity, or space between adjacent pyramid tips, must be at least twice the wavelength of the lowest frequency in the range of interest [36], [37].

$$D > \frac{\lambda_{118Ghz}}{2} \tag{VI.1}$$

Given the condition that the lowest frequency used by TWICE is 118 GHz, the distance between each pyramid, D, must be larger than 1.27 mm. It is also noted that height and angle of steepness of the pyramidal array will also affect the return loss of the calibration target. In general, taller, sharper pyramids will provide more points of reflection as the EM ray travels into and out of the pyramidal cavity. However, one must also be conscious of size restrictions within the tight 6U CubeSat envelope, as well as the development of large thermal gradients within the pyramids. All of these aspects are considered in the following sections.

6.4 Selection of the TWICE Ambient Calibration Target RAM

The following sections will detail the selection process of the TWICE calibration target. To gain an idea of what kind of calibration target material and geometry should be used a few different options were considered. The final TWICE ambient calibration target material and geometry was selected based on its thermal performance and its return loss performance for the given geometry.

6.4.1 Return Loss Considerations

The selection of an ambient calibration target is highly situational. Restrictions in physical size, environment, and frequency at which the material will be absorbing can all determine what type of material and geometry can be used. For TWICE, the ambient calibration target must be able to absorb EM radiation within a range of frequencies from 118 GHz to 670 GHz, with stand the environmental conditions in low Earth orbit, and fit into a 6U CubeSat envelope. Each of the RAMs considered for preliminary testing and design were selected so that they are able to meet the aforementioned environmental and size requirements. These preliminary RAMs are shown in Figure 44. Note that the pyramidal and grooved shaped absorbers meet the criteria set in Equation VI.1. The materials initially considered for testing included ECCOSORB BSR, TK

RAM, and FIRAM 500. ECCOSORB BSR is a high-loss elastomeric absorber produced by Laird. Its flat and thin geometry, measuring at approximately 0.25 mm thick, helps to minimize thermal gradients and allows for easy storage within the 6U CubeSat envelope. The ECCOSORB BSR datasheet, provided by Laird, describes that the material is sufficient for dampening reflections above 6 GHz and is thermally stable [38]. TK RAM is a polypropylene based, space qualified, pre-fabricated RAM designed for use between 50 to 1000 GHz. This RAM is delivered as a pre-made calibration target in 100 mm x 100 mm interlocking squares. The TK RAM calibration target has an approximately one half centimeter thick base with an approximately one half centimeter tall array of pyramids across its top face. Typical off normal incidence performance across the aforementioned frequency range is quoted to be as low as -40 dB or lower [39]. FIRAM 500 is again a space qualified RAM pre-fabricated into a calibration target. It is made up of rubber-like, iron oxide loaded material with a thick base and an array of either grooves or pyramids across its top face. The base and grooves, or pyramids, of this calibration target are both 3.8 mm in height. This material is quoted as having return loss of at least 60 dB to 80 dB when off from normal incidence [40]. Each of these materials are quoted by their datasheets, or directly checked at MSL, to be able to meet the environmental and size constraints of the TWICE instrument.

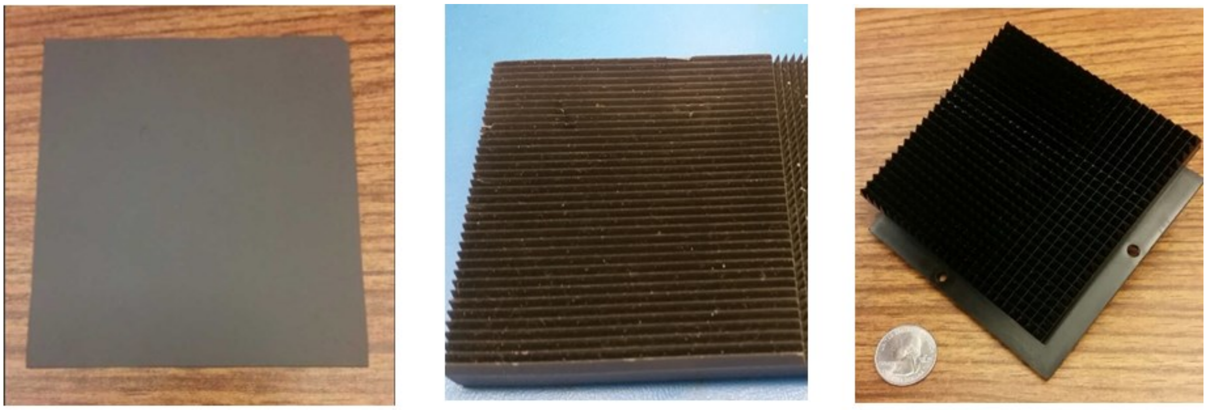

ECCOSORB BSR FIRAM 500 TK RAM

Figure 44: The RAM products selected for preliminary return loss testing include ECCOSORB BSR, FIRAM 500, and TK RAM.

In order to determine the EM absorption of these materials at TWICE frequencies, return loss testing was conducted at the NASA/CalTech Jet Propulsion Laboratory during the weeks of May 22 and May 29, 2017. Each material was tested with a vector network analyzer (VNA) with two integrated extenders, as seen in Figure 46, sweeping in frequency from 325 GHz to 500 GHz. It is important to realize that the frequencies used by the VNA only directly cover 2 of the TWICE frequencies channels. However, the proprietors of both the FIRAM 500 and the TK RAM materials quoted that their materials should have uniform behavior across the GHz spectrum. Therefore, it is expected that the return loss results measured with the 325 GHz to 500 GHz VNA extenders will accurately reflect the EM performance at all of the TWICE radiometer frequency channels.

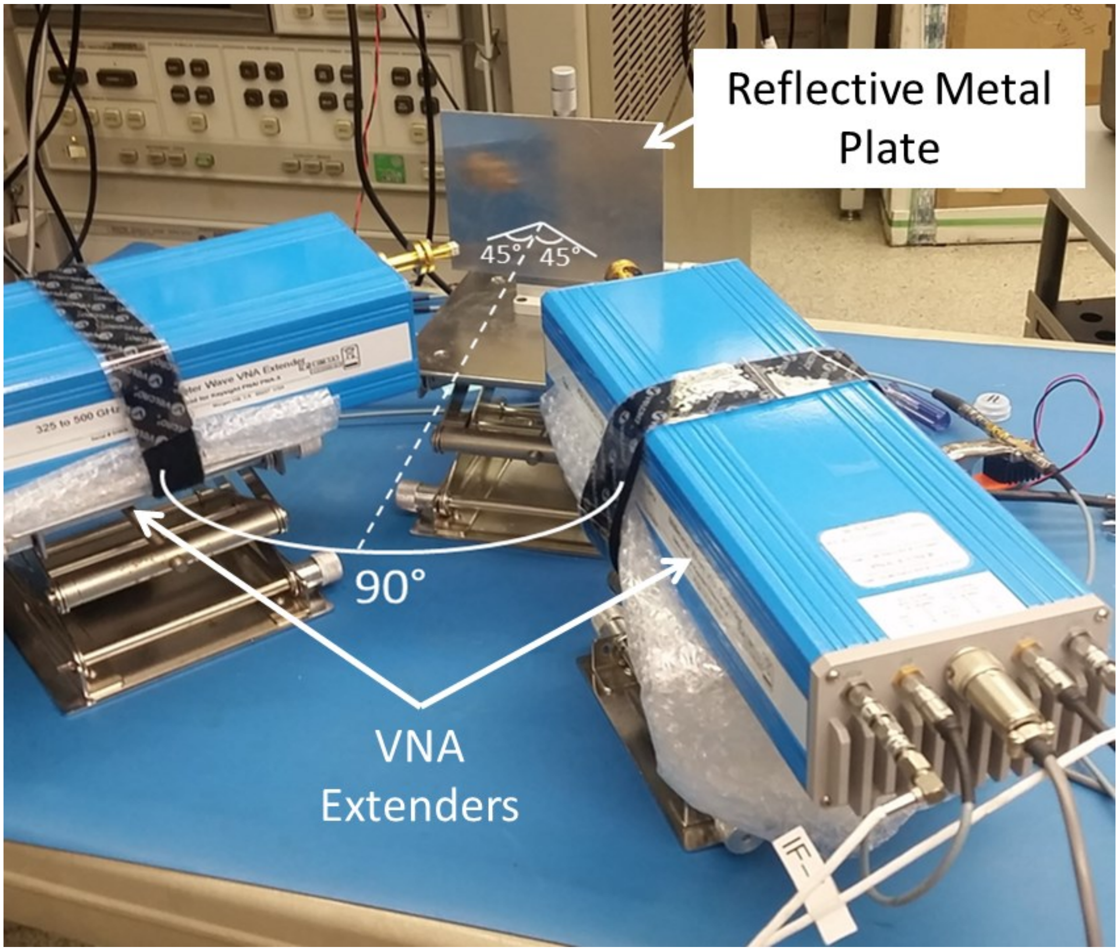

Figure 45: The experimental set up of the return loss testing performed at NASA/Caltech JPL.

Before each material was tested a baseline measurement was performed by way of a reflective metal plate seen in Figure 45. This measurement was done to establish a point of reference to which the return loss of the materials in question would be compared to. In particular, the baseline measurement was assumed to be a perfectly reflective measurement, meaning that the return loss of this measurement was set to zero, shown in Figure 46. The baseline was completed using a flat metal plate, with two VNA extenders pointed at it with an incidence angle of 45 degrees. Recall that the TWICE look angle is set at 45 degrees, motivating the orientation of each LNA extender. Each material was tested under the same configuration as the reference metal plate.

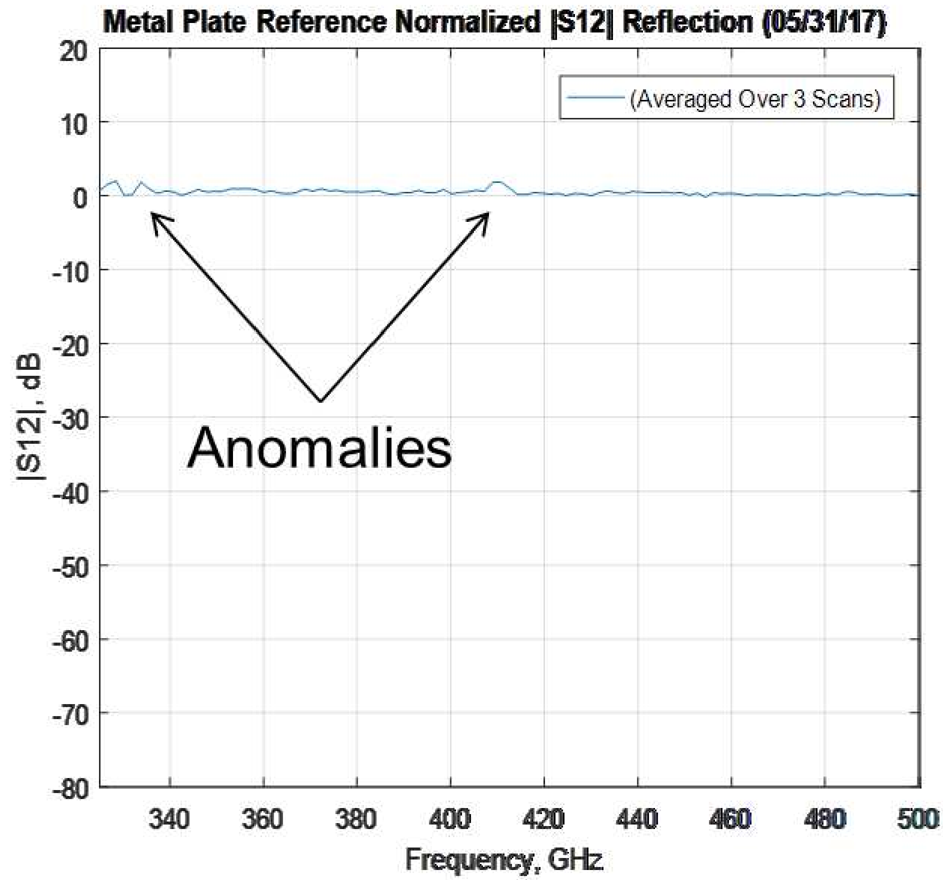

Figure 46: The baseline measurement of the VNA extenders. Note the presence of the anomalies at the beginning and middle of the frequency sweep.

As seen in Figure 46, the frequency sweep is mostly leveled at the 0 dB mark. However, it is noted that there are two unknown anomalies at the beginning and middle of the baseline scan. The origin of these anomalies were not known at the time of testing, however, it is presumed that these anomalies must be the result of other instruments within the testing space interfering with the VNA. These anomalies appear in all but one of the return loss measurements.

The ECCOSORB BSR was tested in a series of different layers ranging from 1 to 5. Based on the datasheet, it was believed that the thickness of the ECCOSORB BSR material strongly affected the return loss performance. The data analysis showed that not only was the ECCOSORB BSR material insufficient at providing a high return loss, there was no measureable dependence on thickness at the VNA frequency range. The results of the ECCOSORB BSR testing can be seen in Figure 47.

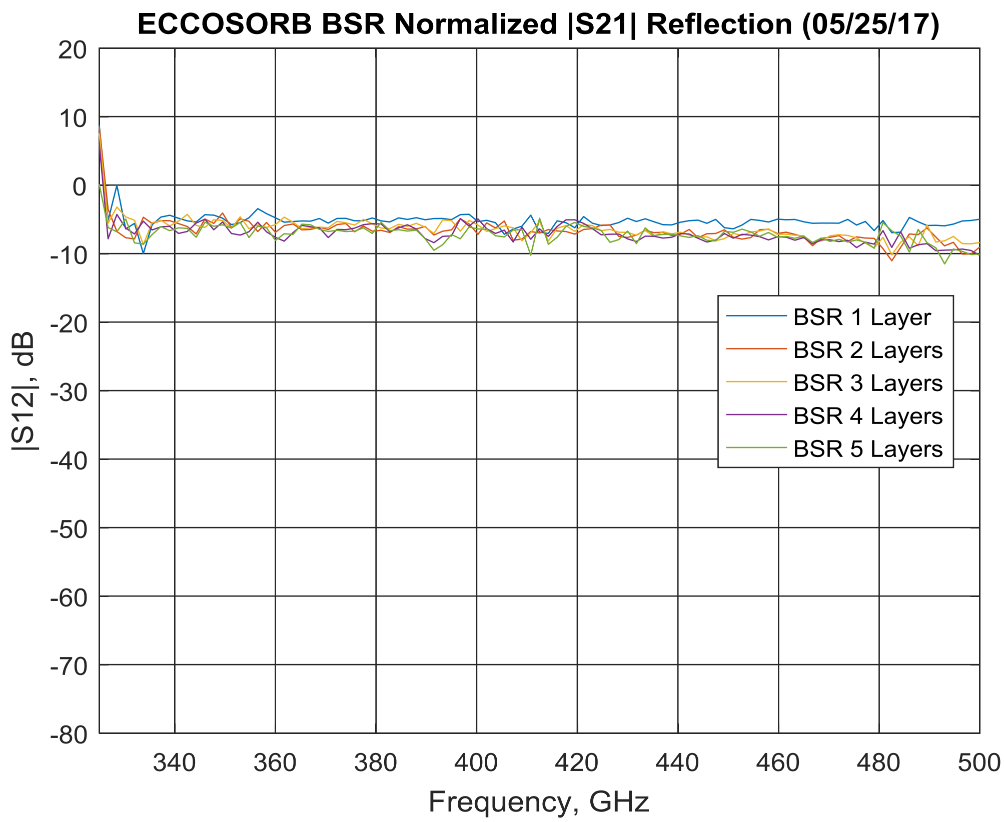

Figure 47: The ECCOSORB BSR was tested across the range of VNA frequencies. This material was only able to provide an average of about – 5 dB of return loss at these frequencies.

The ECCOSORB BSR was only able to provide an average of about -5 dB of return loss. The ECCOSORB BSR test illustrates the difference between resonance absorbers and free space absorbers. Generally, ECCOSORB BSR is used as an absorbing material used within circuit board housings to minimize any EM interference. It has been shown that at millimeter and sub-millimeter frequencies, this type of broad band resonance absorber does not work.

The TK RAM pre-made calibration target was tested in two different configurations, in a front facing configuration and a back facing configuration. The calibration target was first tested with the pyramidal array facing the VNA extenders, and then flipped 180 degrees so that flat back side of the target was facing the VNA extenders.

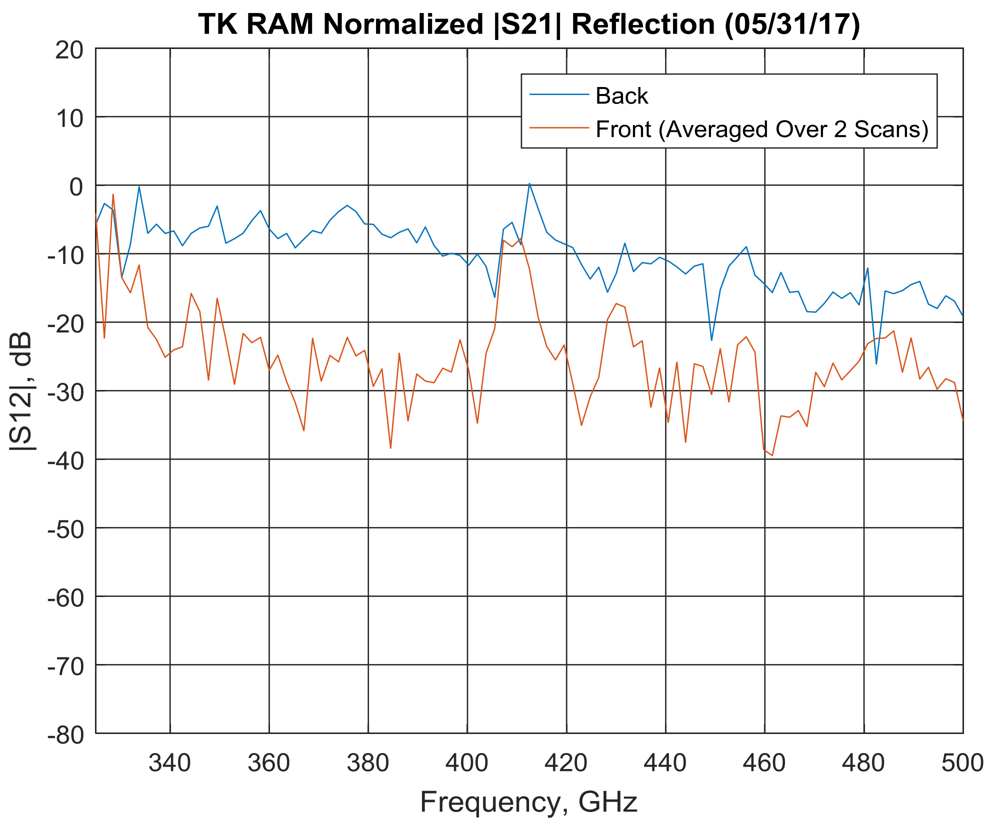

Figure 48: The TK RAM calibration target showed that it is able to provide a return loss of up to an average of about – 25 dB across the VNA frequency range.

The back side of the TK RAM target was tested to explore the possibility of utilizing the same TK RAM material, however, without the pyramidal geometry, in order to save space within the 6U CubeSat frame. This test also helps to illustrate the advantage of using a pyramidal geometry facilitate numerus reflections within the pyramidal channels. The results of the return loss testing for the TK RAM material are seen in Figure 48. The anomalies from the baseline testing are very noticeable in this test around 325 GHz and 415 GHz for both the front and back side measurements. Aside from these regions, the return loss of the pyramidal side of the TK RAM material is on average as low as – 25 dB. Interestingly, the back side of the TK RAM material produces a return loss that increases over the range of the sweep from about – 5 dB at 325 GHz to about – 15 dB at 500 GHz.

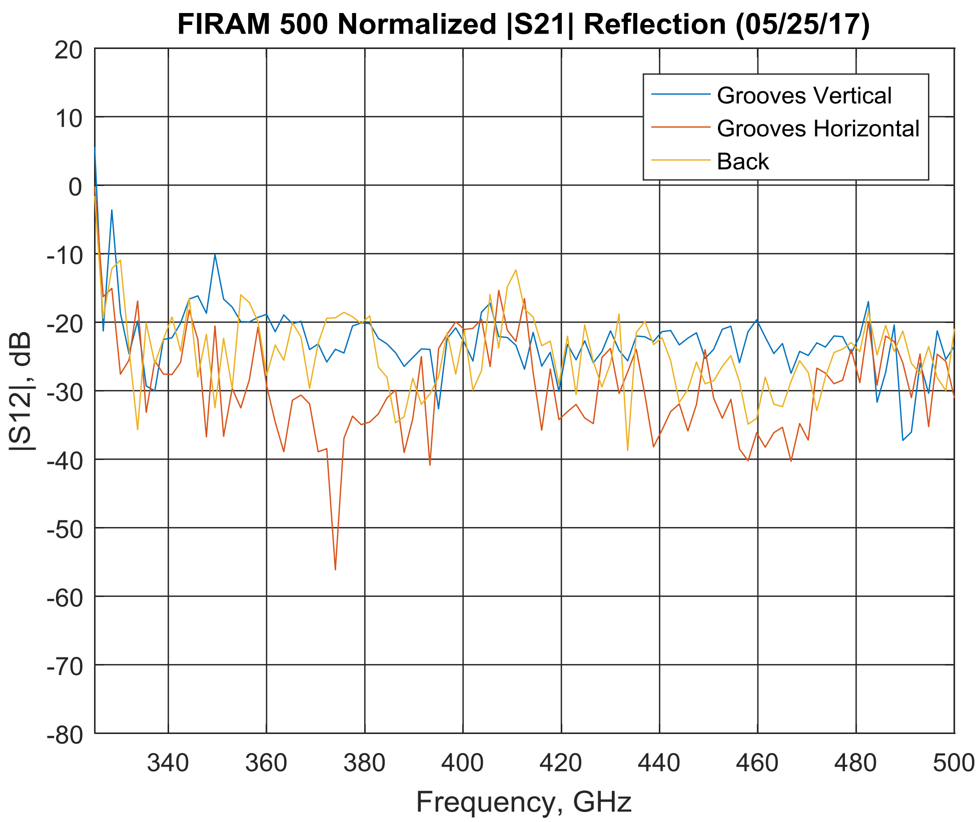

Figure 49: The FIRAM 500 calibration target showed that it is able to provide a return loss of up to an average of about – 25 dB across the VNA frequency range.

The geometry of the FIRAM 500 target allowed for testing in a few different configurations. Because the FIRAM 500 target under test utilizes a grooved geometry instead of a pyramidal geometry, it was tested in a vertical and horizontal configuration. The flat back side of the FIRAM 500 material was also tested. The first set of tests placed the grooves facing the VNA extenders, in both a vertical and horizontal orientation. The return loss the FIRAM 500 target in its front facing configuration for both vertical and horizontal is seen in Figure 49. This orientation provided a return loss that rivaled that of the TK RAM target, at about – 25 dB across the sweep. Surprisingly, the back of the FIRAM 500 target reach similar return loss as the front facing configurations. This is likely due to the loaded nature of the FIRAM 500 material.

The results of the return loss testing provided a way forward to complete the design of the TWICE ambient calibration target. Because of the use of polarized channels on the TWICE instrument, 670 GHz, it was determined that the ideal geometry for the TWICE ambient calibration target would be pyramidal. While both the TK RAM and the FIRAM 500 materials can provide a stable scene for the TWICE radiometers, both of these have serious issues with thermal stability.

6.4.2 Thermal Considerations

Aside from providing sufficient return loss at TWICE frequencies, the material used for the ambient calibration target must also be thermally stable and predictable. Thermal instabilities within the TWICE ambient calibration target will contribute to the uncertainty in the calibration measurement. Materials that can minimize thermal gradients are ideal because they will reduce ambiguity in the physical temperature measurement of the target and ultimately in the data of interest from the Earth scene. The thermal properties of TK RAM and FIRAM 500 materials were studied to help determine the best fit for the TWICE project. Note that because the ECCOSORB BSR material did not provide sufficient return loss measurements, its thermal properties were not considered.

Materials with higher thermal conductivity are more effective at mitigating thermal gradients. For example, copper is a great thermal conductor and is able to let heat flow easily through its body. A material like plastic or silicone, however, tends to be a poor conductor of heat and will allow large thermal gradients to form within their body. This, of course, is problematic considering that the TK RAM target is made of a plastic based material and the FIRAM 500 target is made of a silicone based material. It is understood that plastic and silicone based materials would not be able to sufficiently minimize thermal gradients that might appear during a flight campaign or a space mission. In order to mitigate this problem, a new material would need to be considered.

Cuming Microwave's C-RAM RGD material is an iron filled epoxy resin that offers similar return loss capabilities as the TK RAM or the FIRAM 500 materials while also providing over 5.5 times higher thermal conductivity, 1.21 W/m/K, compared to the 0.22 W/m/K and 0.2 W/m/K of the TK RAM and FIRAM 500, respectively. It is believed that this material will offer increased thermal performance and help establish reliable calibration for the TWICE radiometers. In order to compare the thermal performance between the TK RAM or FIRAM 500 materials and the C-RAM RDG material, ambient temperature simulations were performed. Because the thermal conductivity of the TK RAM and FIRAM 500 materials are relatively the same only the TK RAM material was tested.

The temperature simulation consisted of starting each material at a uniform and predetermined temperature, and then allowing the ambient temperature around the materials to change. Note that at the beginning of the simulation both the material and the ambient environment were at identical temperatures. The ambient temperature was ramped up by 10 °C, over the course of 5 minutes, from its starting point at 40 °C. It is important to recognize that in order to maintain a level of comparability between the two materials; both materials were tested with identical geometries. Because the TK RAM target was selected for testing, its geometry was used. The results of these simulations, Figure 50, show how the calibration material used will behave in a dynamic ambient environment.

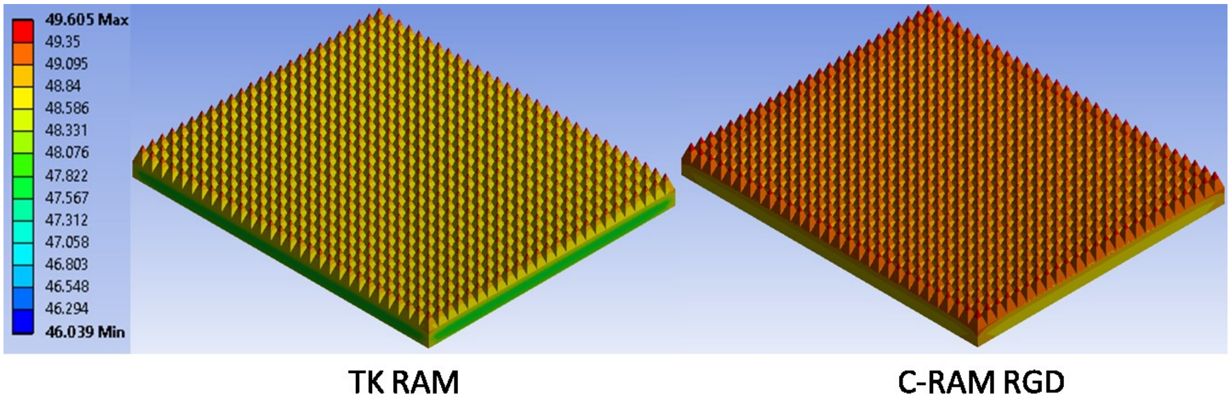

Figure 50: A thermal comparison between the TK RAM plastic based material and the C-RAM RGD epoxy resin material for a variable ambient environment.

It is important to note that these simulations are performed by way of convection, meaning that radiative heating is not considered. Within the simulation, and in practice, predicting and modeling radiative heating across the surface of the target's geometry is very difficult. For use in an environment where radiative heating strongly affects the temperature of the ambient calibration target, the calibration system will need to be redesigned.

As expected, simulations show that the C-RAM material is more thermally stable than the TK RAM material. The largest temperature difference within the TK RAM material is about 3.56 °C, whereas the largest temperature difference within the C-RAM material is about 1.32 °C. It is important to notice the temperature gradients that develop within the pyramidal structure of the calibration target. These structures are what the TWICE radiometers directly observe during calibration. Ideally, the temperature gradient within the pyramids will be as small as possible. From the thermal simulations, it can be seen that the C-RAM material produces smaller temperature gradients within the pyramidal structures than that of the TK RAM material. More specifically the thermal gradient within the C-RAM pyramids is approximately 2.7 times smaller than that of the TK RAM pyramids.

Figure 51 shows a cross sectional view of each target. The cross-sectional view corroborates with expectations that the C-RAM material would have more thermal uniformly in a dynamic ambient environment. It is expected that in low earth orbit like conditions, the thermal behavior of the TWICE ambient calibration target would be much different. Regardless of material, radiative heating from the Sun, Earth, and the TWICE spacecraft bus are expected to create large gradients.

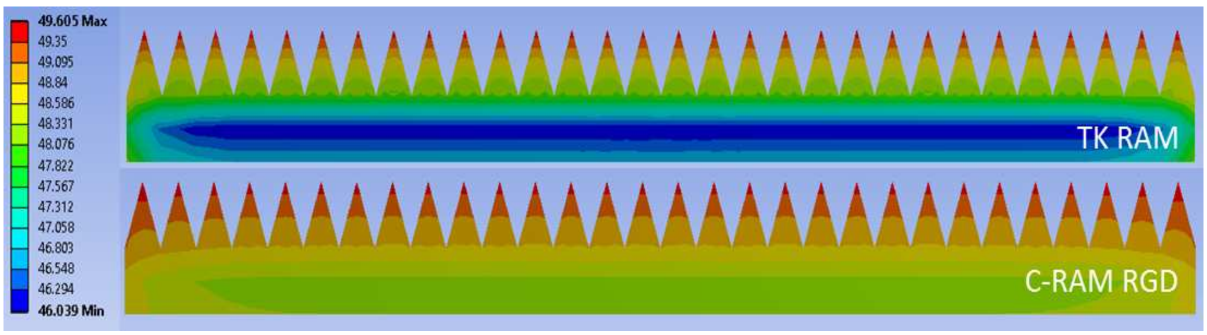

Figure 51: A comparison of vertical thermal gradients between TK RAM and C-RAM RGD.

Over the course of a single orbit, the intensity and incidence angle of the Sun can create quickly changing and unpredictable gradients. This is largely due to the open and isolated placement of the ambient calibration target. In its current incarnation, the TWICE ambient calibration target has no way of blocking sources of radiative heating like the Sun. For the remainder of this work, the TWICE ambient calibration target will only be considered within the thermal environment of the Earth's atmosphere.

6.5 Design and Fabrication of TWICE Ambient Calibration Target

Due to its increased thermal capabilities and expected return loss performance at TWICE frequencies, the C-RAM RGD material was chosen for the TWICE ambient calibration target. Unlike the other materials, C-RAM RGD is not fabricated into a pre-made calibration target. Instead the TWICE ambient calibration target must be created out of a solid slab of the C-RAM

RGD material. The design of the TWICE ambient calibration target is primarily based on target designs that are known to provide high return loss performance at the TWICE frequencies. In particular, the TK RAM calibration target has shown its geometry is capable of providing sufficient return loss at TWICE frequencies. It was decided that the geometry of the TK RAM target will be used based of the expectation that grooved geometries can interfere with or distort the signals being received by the polarized radiometers used by the TWICE instrument. Some of the basic characteristics of the TK RAM target design are shown in Figure 52.

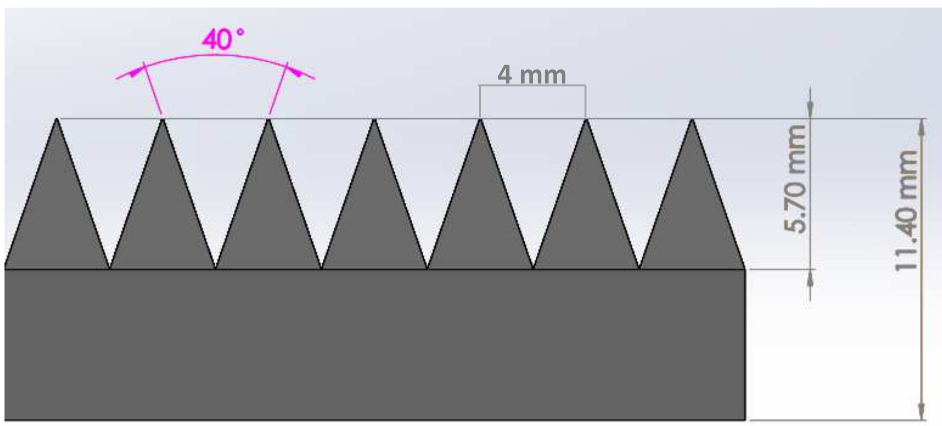

Figure 52: A simplified illustration of the pyramidal geometry used to create the TWICE ambient calibration target.

The height of the pyramidal array, as well as the base that the array sit upon, is 5.70 mm. The angle between adjacent pyramidal faces is approximately 40 degrees, and the space between adjacent pyramids is 4 mm. These dimensions are identical to that of the TK RAM target which is designed for use up to THz frequencies.

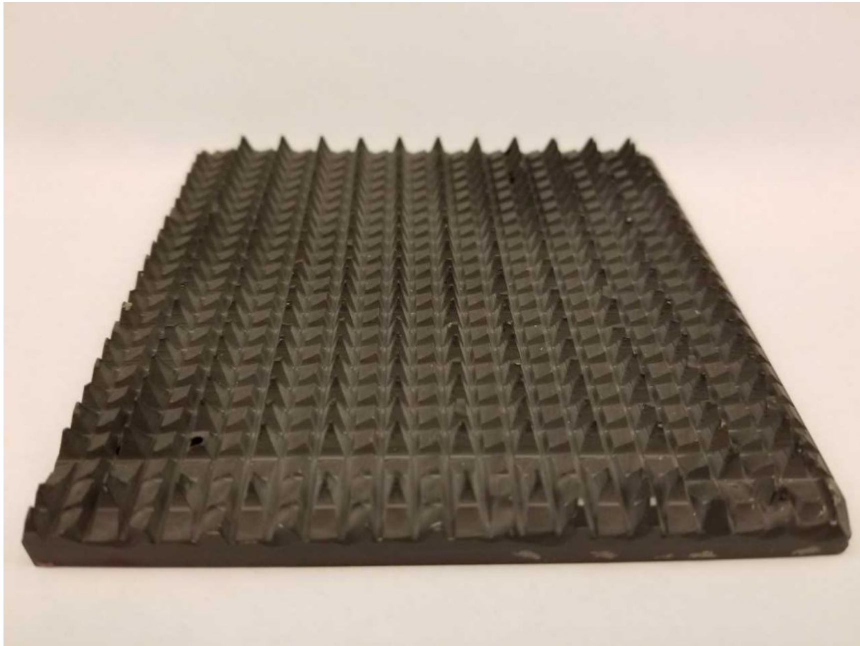

Figure 53: The bit of the milling machine used to fabricate the first iteration of the C-RAM RGD calibration target was not able to reach a high enough RPM to successfully create the desired geometry.

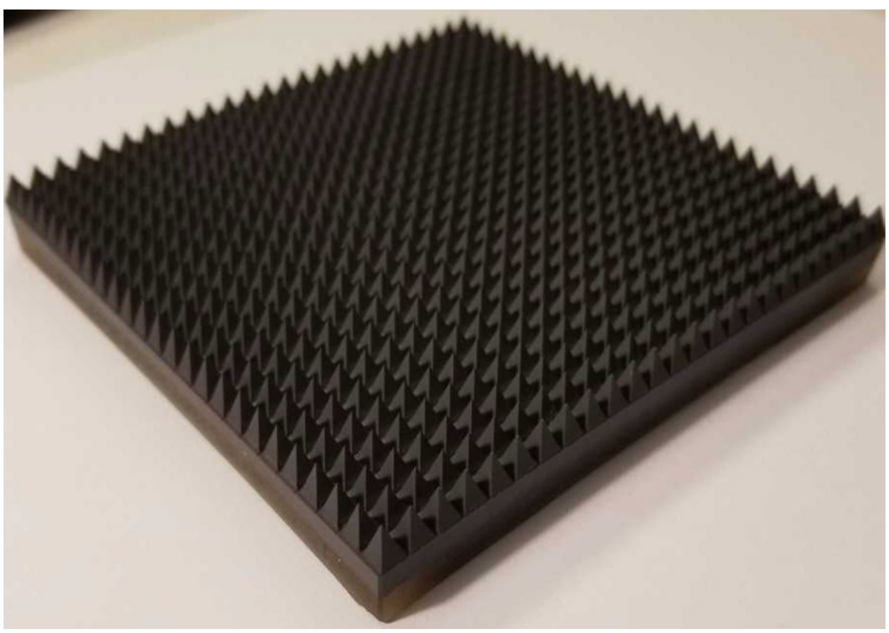

Figure 54: A sample of the C-RAM RGD material fabricated into its desired pyramidal geometry.

Manufacturing the C-RAM RGD material into the dimensions of the TK RAM target is not a straight forward task. The C-RAM RGD material is hard and brittle, making it very easy for the target to break during or after manufacturing. The first several attempts at machining the C-RAM RGD material into the desired geometry resulted in rows of destroyed pyramids and target bases broken in two. Figure 53 shows a prototype example of the C-RAM RGD target destroyed during fabrication. To mitigate this issue, it was determined that the C-RAM RGD material would need to be manufactured at a precision machining shop. A completed prototype is seen in Figure 54.

6.6 Thermal Cycling Test of the C-RAM RGD Calibration Target

To study the behavior of the C-RAM RGD material in real world conditions, an ambient thermal cycling test was performed. The Microwave Systems Laboratory has access to a thermal chamber capable of emulating various atmospheric. For testing of the C-RAM RGD ambient calibration target, the thermal chamber was programed to push the expected temperature limits for atmospheric conditions, for example like during a flight campaign on an ER-2 High-Altitude Airborne Science Aircraft. Such an aircraft can reach an altitude of up to 70,000 feet [41]. At this altitude, which is well above the tropopause, temperatures can dip down to -60 °C [42]. With the aid of the thermal chamber, the C-RAM RGD calibration target can be tested in the most extreme atmospheric thermal environments. To conduct this test a prototype target was fabricated. The prototype target, seen in Figure 55, is designed with specifically placed bore holes used to fit thermistors. As shown in the figure, the 8 bore holes located on the bottom of the prototype target are positioned so that the thermistors placed within them can provide average temperature information of the interior base of the target. Each thermistor bore is 3 mm in diameter and has a depth of approximately 5.7 mm. One will note that the depth of the bores is identical to the thickness of the target base. This depth is chosen so to minimize any measurement differences between the thermistors and the pyramidal array.

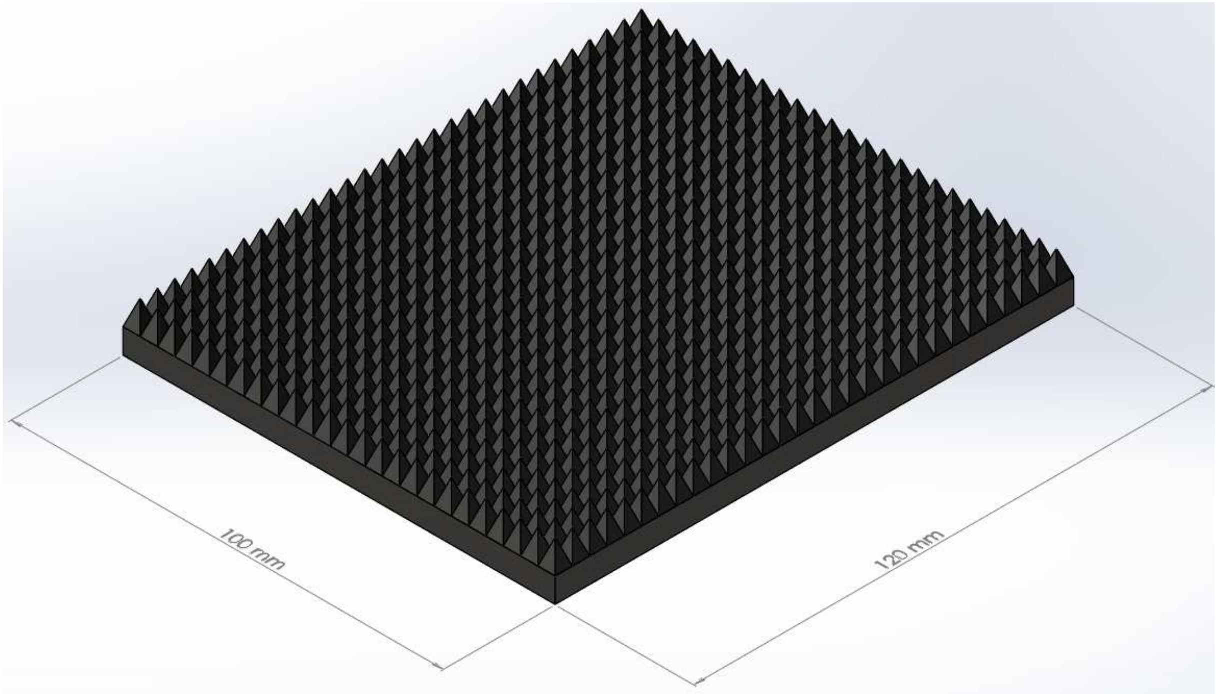

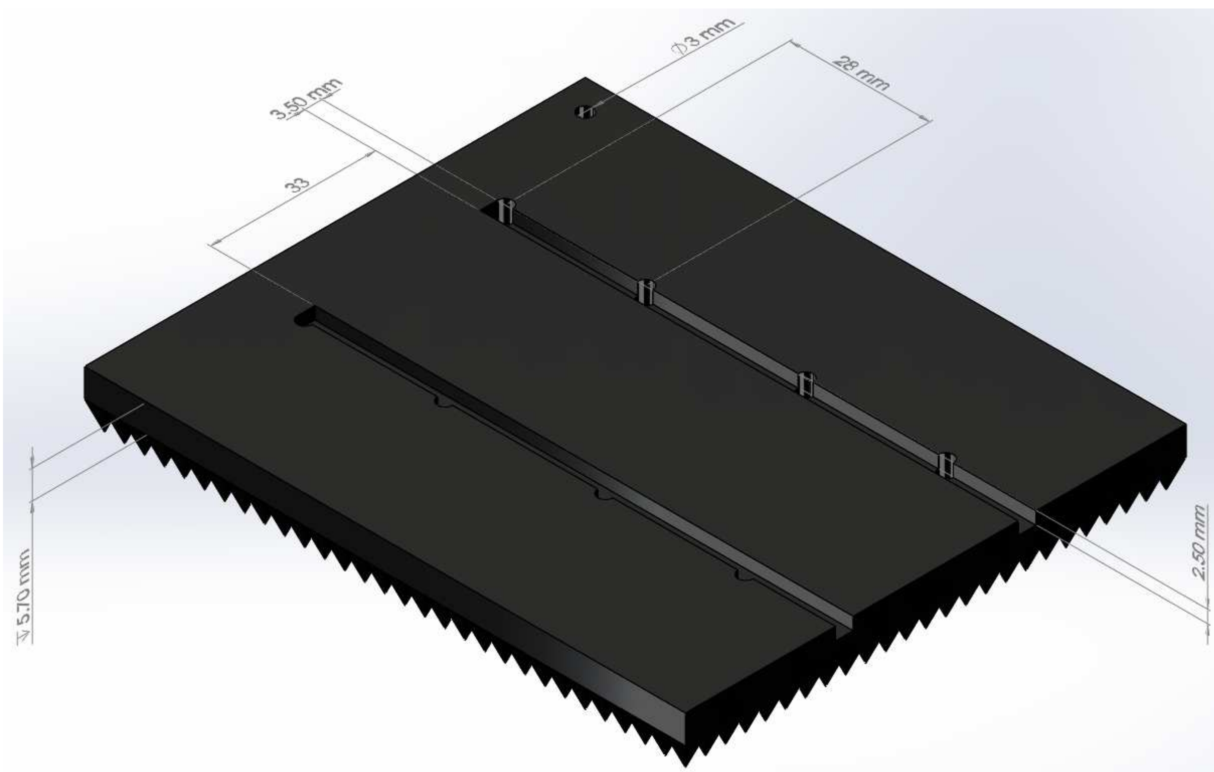

Figure 55: A CAD model of the prototype ambient calibration target used for thermal cycling testing.

Due to the brittleness of the C-RAM RGD material, it was not possible to bore holes into individual pyramids. While this would have provided the best measurement of the physical temperature of the pyramidal array that the TWICE radiometers will be observing during calibration, it is expected that placing the thermistors at the base of the pyramidal array will not contribute any significant measurement differences for ambient conditions.

The spacing of the thermistor bore holes was motivated by the near field footprint coverage of the TWICE radiometers on the ambient calibration target. An illustration of the near field footprint coverage is seen in Figure 56.

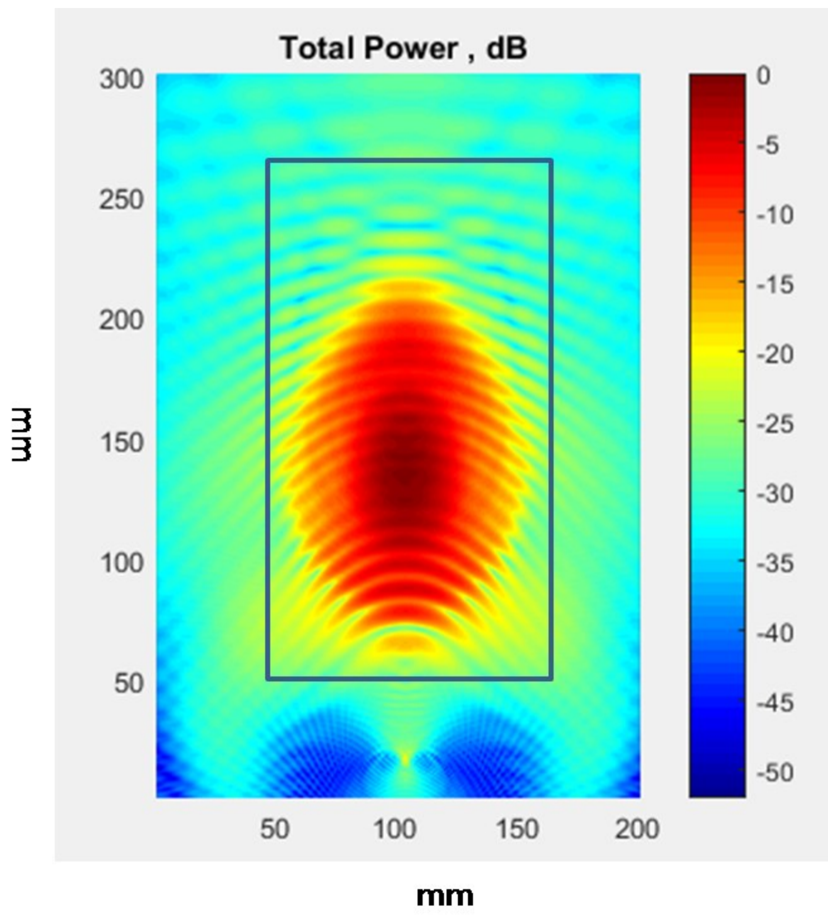

Figure 56: An HFSS simulation of the approximate size and distribution of power for the 118 GHz radiometer channel on the near field plane of calibration.

In Figure 56, the rectangle represents both the boundary within which 98% of all of the power is contained and the approximate amount of two-dimensional space allocated for the final TWICE ambient calibration target. It is seen in the figure that the -3 dB footprint perimeter is generally located at the center of this boundary, therefore, 98% of the signal received by the TWICE radiometers during calibration is from the center of the ambient calibration target, thus prompting the placement of the thermistor bore holes. A better knowledge of the temperature of the calibration target where almost all of the observed energy is coming from will increase reliability in the calibration process.

The thermistors used for the thermal testing are the U.S. Sensor KS502J2 NTC Thermistor [43]. These thermistors are quoted as having a thermal range from -55 °C to +135 °C, with an uncertainty of approximately ± 0.1 °C in the range of -30 °C and 50 °C, and ± 1 °C for temperatures outside that range. One will note that the diameter of the thermistor bores on the C-RAM RGD target prototype is 3 mm, which is selected to accommodate the 2.44 mm diameter of the thermistor tips. This will allow enough room for the thermistors and a fixing adhesive to fit. To account for the circuitry needed to operate the thermistors, two rectangular grooves were cut into the base of the prototype target. These grooves not only help to consolidate the wires attached to the thermistors embedded within the prototype target, but also help store them within the target itself so that it is able to sit flush upon a supporting base.

The testing configuration of the prototype target can be seen in Figure 57. In total 10 thermistors were used to monitor the interior temperature of the prototype target, the surface temperature of the prototype target, and the ambient temperature of the thermal chamber. Each of the thermistors used were connected to the same LTC2439-1 16-bit ADC discussed in the next chapter. The calibration target rested upon a metal base that was tilted away from the light bulb located inside of the thermal chamber. It was expected that the light bulb might contribute some radiative heating during the thermal cycling test, thus skewing the results of the C-RAM RGD material's behavior in ambient conditions. Lastly, thermal paste was used to ensure that there would be no issues with conductive heat transfer between the metal base that the target is resting upon and the bottom face of the target.

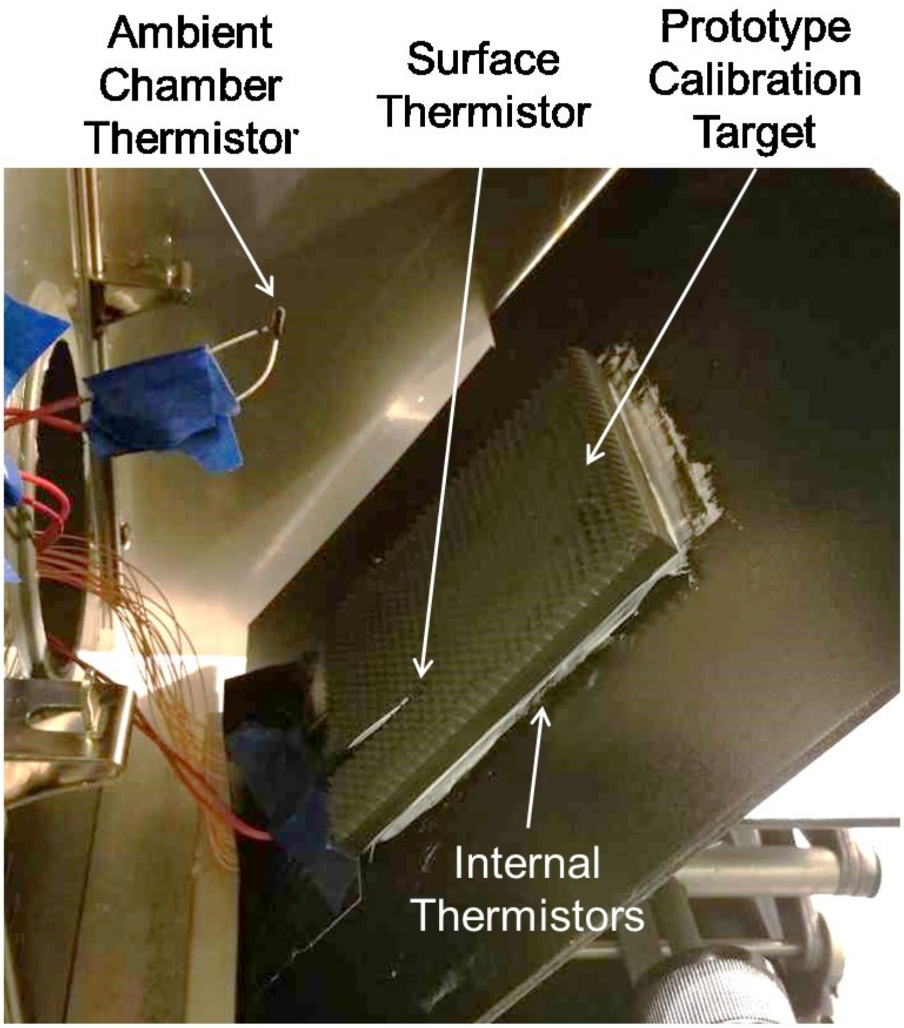

Figure 57: A picture of the prototype calibration target during the thermal cycling test.

The thermal cycling test was designed to function in a stepwise fashion, allowing for moments of ambient stability and ambient change. The ambient temperature of the thermal chamber, and the prototype target, started at approximately room temperature, 30 °C. At the start of the cycle, the ambient temperature began decreasing by approximately 10 °C over the course of 5 minutes. Once the 5 minute temperature change was completed, the thermal chamber would soak at the new temperature for 10 minutes. At the end of the soaking time, the chamber would then again decrease the temperature by 10 °C over a 5 minute period. This cycle repeated until the ambient temperature of the thermal chamber had reached approximately – 65 °C. The results of the cooling regime are seen in Figure 58.

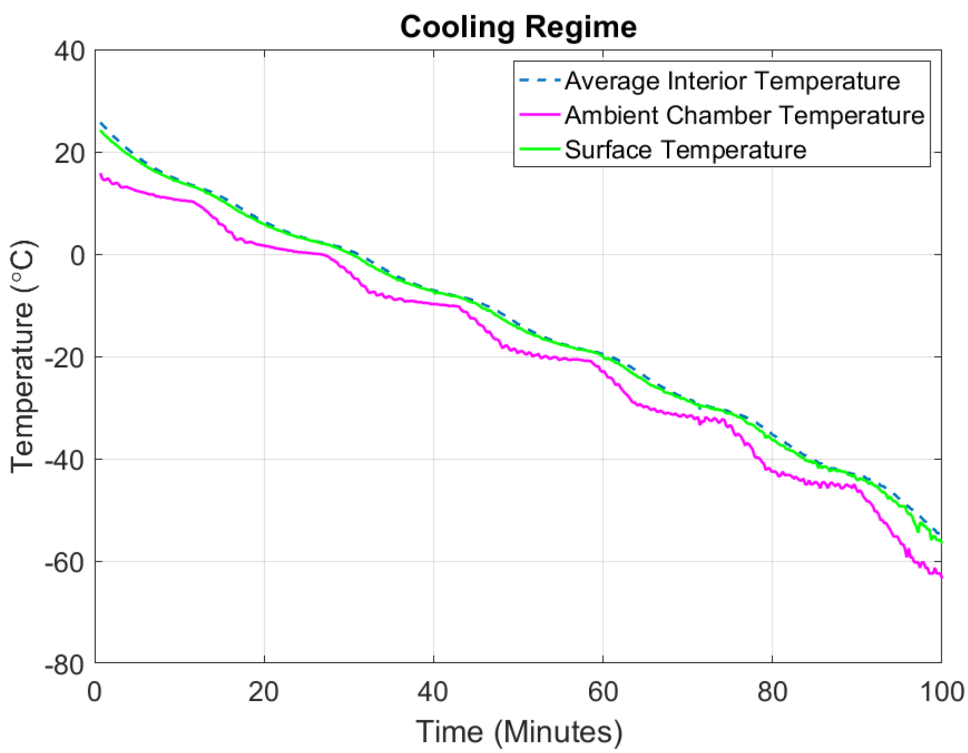

Figure 58: The results of the cooling regime of the thermal cycling test performed on the prototype C-RAM RGD ambient calibration target.

Note that there are 4 distinct lines of data in Figure 58. The blue dotted line represents the averaged interior temperature of the prototype target. That is to say, all of the embedded thermistors were averaged together to determine the average temperature of the interior prototype target. The red line represents the difference between the temperature of the thermistor fixed to the pyramidal array of the target and the averaged interior temperature of the target.

Generally speaking, the temperature difference between the interior of the calibration target and the surface of the calibration target is very small. The average temperature difference between the interior temperature of the calibration target and its pyramidal array is only 0.15 ± 0.10 °C. As one would expect, the temperature difference between the interior and the surface tends to grow during the ramping portions of the cycle, and shrinks during the soaking portions. Note that the aberrations in Figure 58, beginning at about – 30 °C, are the result of a reference voltage saturation within the ADC.

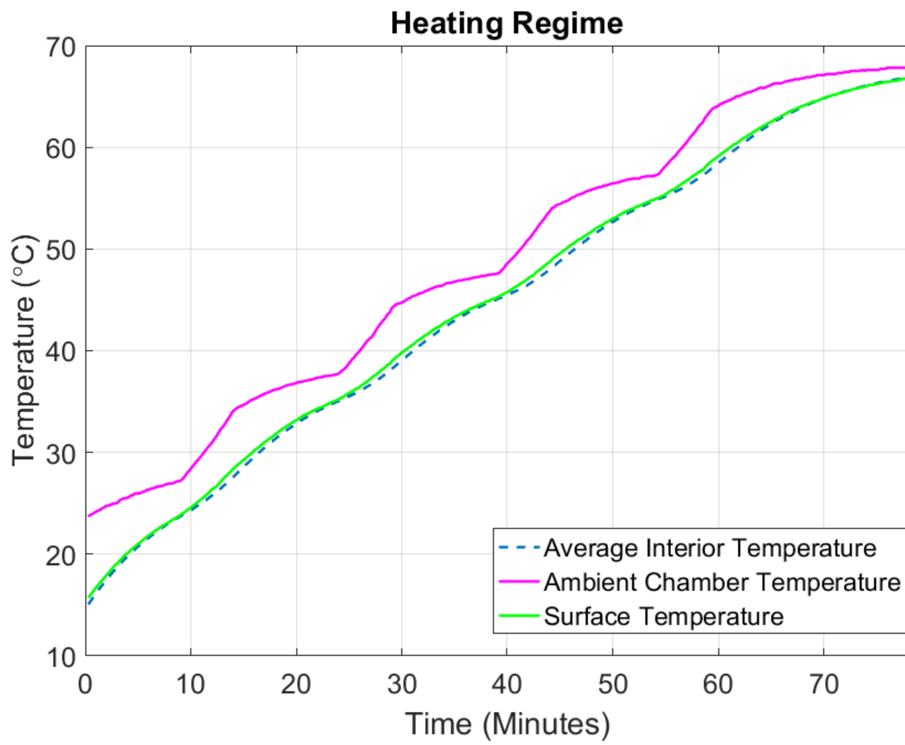

Figure 59: The results of the heating regime of the thermal cycling test performed on the prototype C-RAM RGD ambient calibration target.

Once the thermal chamber reached a temperature of approximately – 65 °C, it began quickly ramping up to room temperature, where the heating regime of the cycle would begin. Similarly to the cooling regime, the heating regime utilized 5 minute ramping times and 10 minute soaking times. However, instead of cooling the ambient temperature by 10 °C per ramp, this regime heated the ambient temperature by 10 °C per ramp. The results of the heating regime are shown in Figure 59.

As seen in the figure, the heating regime mimicked the behavior of the cooling regime, increasing the temperature in a stepwise fashion until it reached an ambient temperature of approximately 70 °C. The temperature difference between the pyramidal array thermistor and the averaged interior thermistor is approximately – 0.09 ± 0.06 °C.

The results of the thermal cycling test lend to the stability and confidence of the C-RAM RGD material and the pyramidal design for use in an ambient environment. The temperature differences measured are on the order of a few tenths of a degree, similar the thermistors overall uncertainty. As a result, the thermal behavior of the calibration target is expected to be well known during flight campaigns or during any operation where the ambient temperature is not known. Note that the uncertainty of the temperature difference was determined by a standard deviation calculation. Recall from the simulated results that the expected temperature difference between the location of the interior thermistors, at the base of the pyramidal array, and the surface of the pyramidal array was expected to be on the order of 1 °C. It is noted here that the measured results show that the maximum temperature difference measured between the interior thermistors and the surface thermistor is approximately 0.5 °C. Thus, it is expected that the actual thermal reliability of the C-RAM RGD calibration target will be about twice that shown in the simulation.

6.7 Final Design of the TWICE Ambient Calibration Target

The final design of the TWICE ambient calibration target is made to meet the footprint spillover specifications of the TWICE radiometer instrument while also adhering to the size constraints of the 6U CubeSat frame. In general, the geometry and shape of the final design match very closely to the prototype target used for thermal cycling testing. The final TWICE ambient calibration target design is seen in Figure 60.

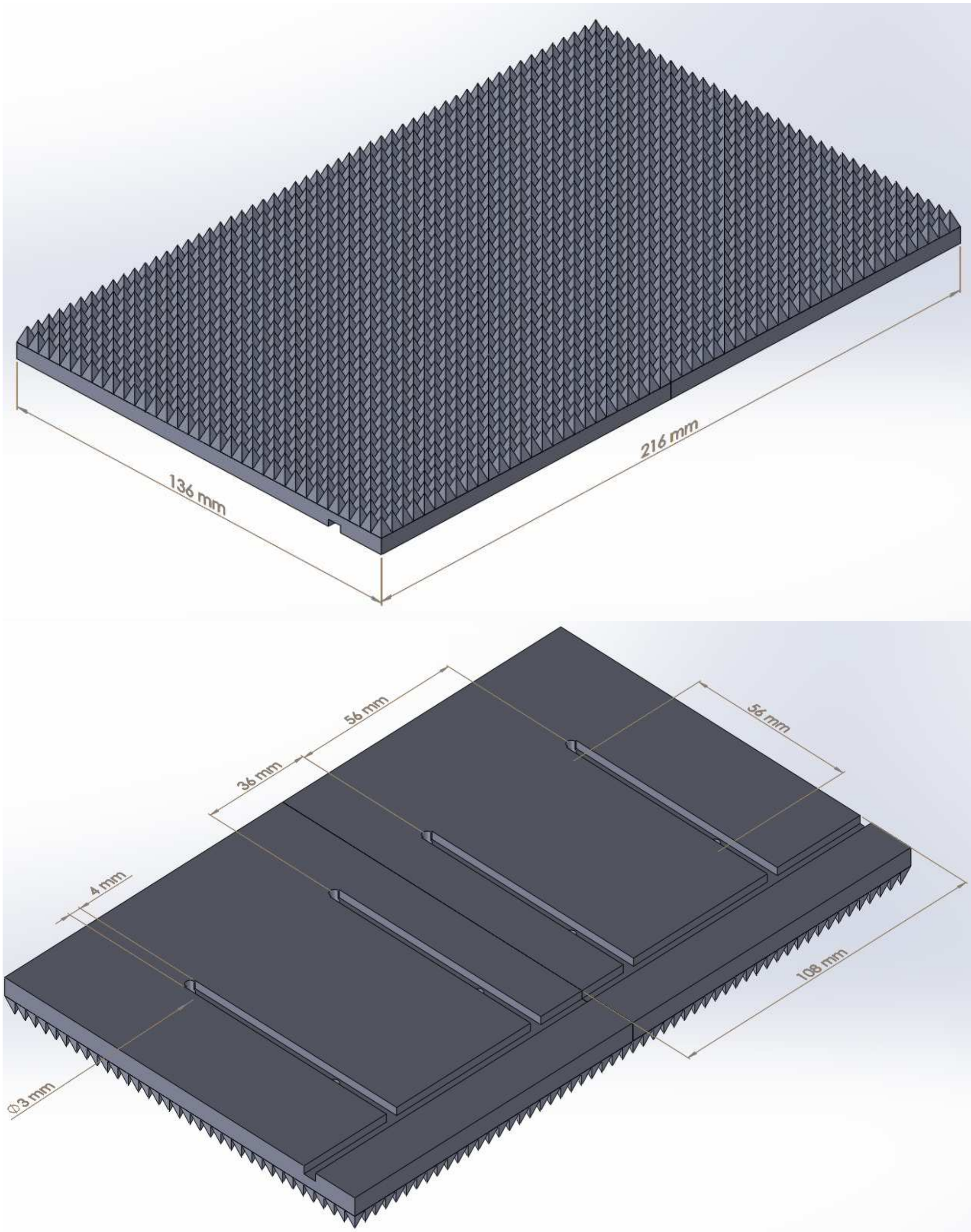

Figure 60: Dimensions of the final ambient calibration target.

Note that channels and bores are again used in the final design to allow for thermistors to be embedded into the base of the calibration target. One will note that this design utilizes only a single output channel instead of two, unlike the prototype target. Using a single output channel for the thermistor wires helps to simplify the design and prevent any extra accommodations needed for the wires to enter the interior of the 6U CubeSat frame. As a result the channel width was slightly increased to help with consolidating all of the thermistor wires into a single channel. Like the prototype target, 8 thermistors will be embedded in the base of the final target. It is expected that for ambient atmospheric conditions the 8 thermistors will provide accurate temperature data of pyramidal surface. Note that the placement of the thermistor bore holes aligns with the expected power distribution of the nearfield radiometer footprint. That is to say, 4 of the 8 thermistors are grouped close to the center of the target so that a higher resolution temperature measurement can be taken for the part of the near field radiometer footprint that contains the highest amount of energy. Spacing between the thermistor bores was adjusted so to provide the most uniform distribution for the new dimension.

The final calibration target is made up of two different pieces. Both pieces are the mirror of the other such that there is only one specific way that they can fit together. Dividing the whole ambient calibration target into two parts helps not only with manufacturing, but also with fixing the target to the mounting plate.

6.8 TWICE Cosmic Microwave Background Reflector

Spaceborne external, two point calibration systems, like that used on the TWICE radiometer instrument, often utilize the Cosmic Microwave Background (CMB) as a cold reference. Some instruments, like TEMPEST-D, directly observe the CMB at specific points in their scan [44]. Other instruments, like the Global Precipitation Mission Microwave Imager (GMI), use a reflector to reflect the view of the CMB into the radiometer instrument during its scan [45]. In any case, the use of the CMB as a cold reference for an external, two point calibration system is common for spaceborne radiometer instruments. TWICE is no exception to this standard and utilizes a CMB reflector for its calibration system, seen in Figure 12.

In general, the TWICE CMB reflector must fulfill the exact opposite role that ambient calibration target fulfills. That is to say, instead of absorbing all incident radiation, the CMB reflector must reflect all incident radiation to towards the radiometer instrument. For microwave frequencies this can be achieved by simply implementing a metal sheet. Specific coatings can be used to increase the reflectivity of the CMB reflector, or to reduce its emissivity. Note that a emissive reflector will appear to be warmer than the CMB due to the emission of the plate itself. However, reflector emissivity can be avoided by utilizing specific coatings on the reflector surface. For instance, the GMI reflector uses a vapor deposited aluminum coating in conjunction with a SiOx coating to maximize reflectivity and minimize any degradation of the reflective surface. It is expected that the TWICE CMB reflector will share the same reflective coatings used on the primary and secondary mirror, this way emissivity will be minimized from an end-to-end perspective.

The TWICE CMB reflector will be same size and shape as the ambient calibration target, seen in Figure 12. The reflector will be made up of a thin, approximately 1 mm, sheet of aluminum that is storable and deployable in the same way that ambient calibration target is.

6.9 TWICE Calibration Target Configuration and Deployment

The TWICE calibration targets are designed to deploy from a stored position, shown in Figure 61, to the open position shown in Figure 12. To achieve deployment, both of the calibration targets are fixed to hinges, circled in red in Figure 61. These hinges are designed to rotate 90 degrees from the stored positon to the open positon. These hinges are seen in Figure 62.

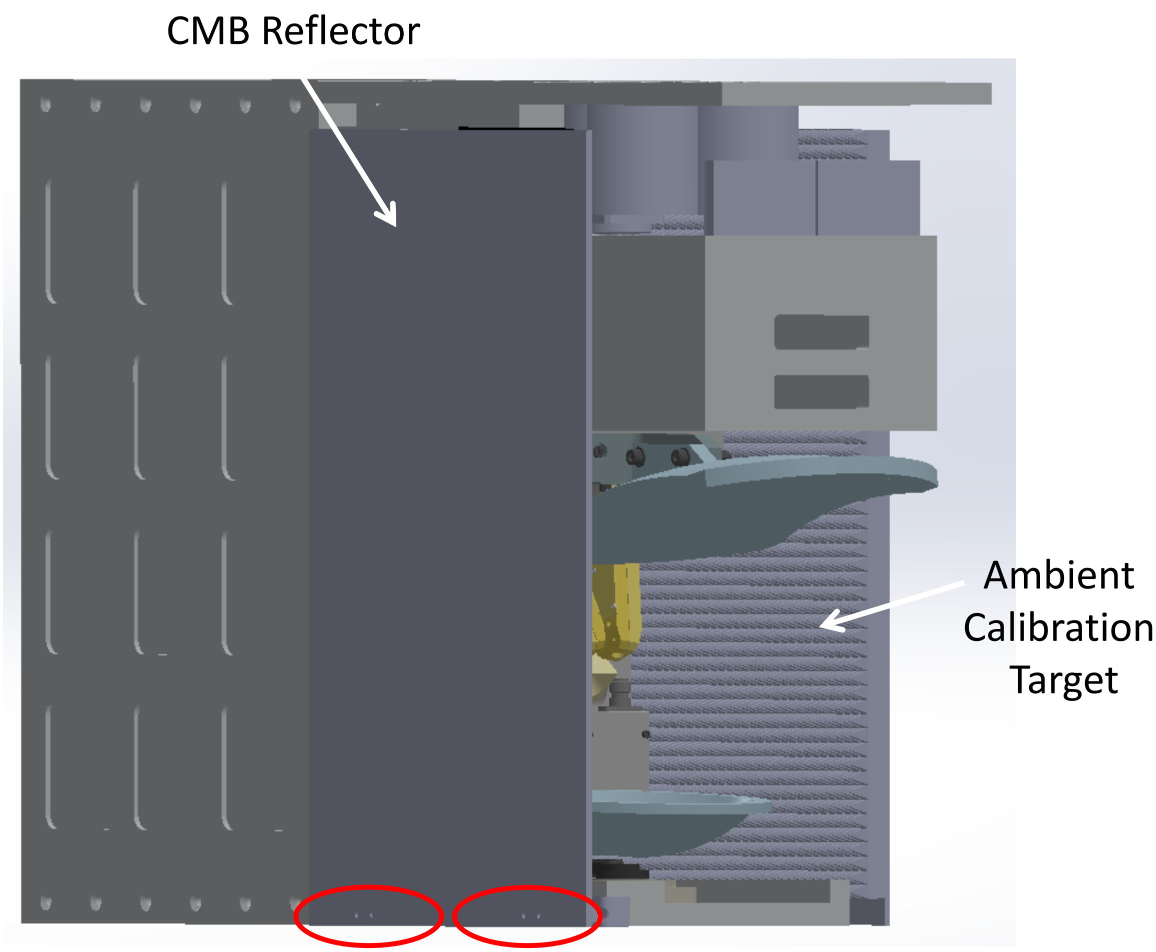

Figure 61: The TWICE 6U CubeSat and radiometer instrument shown it is stored configuration.

Once the both of the calibration targets have been deployed, the TWICE radiometer instrument can begin nominal operation. Note that the hinges are attached directly to the CMB reflector base. However, because of the brittle nature of the ambient calibration target, along with its complex geometry, hinges cannot be directly attached to its base. Instead, hinges will be attached to the plate that the ambient calibration target is mounted upon. Due to the extended height of the ambient calibration target, the deployment hinges will be attached to the mounting plat by way of spacers.

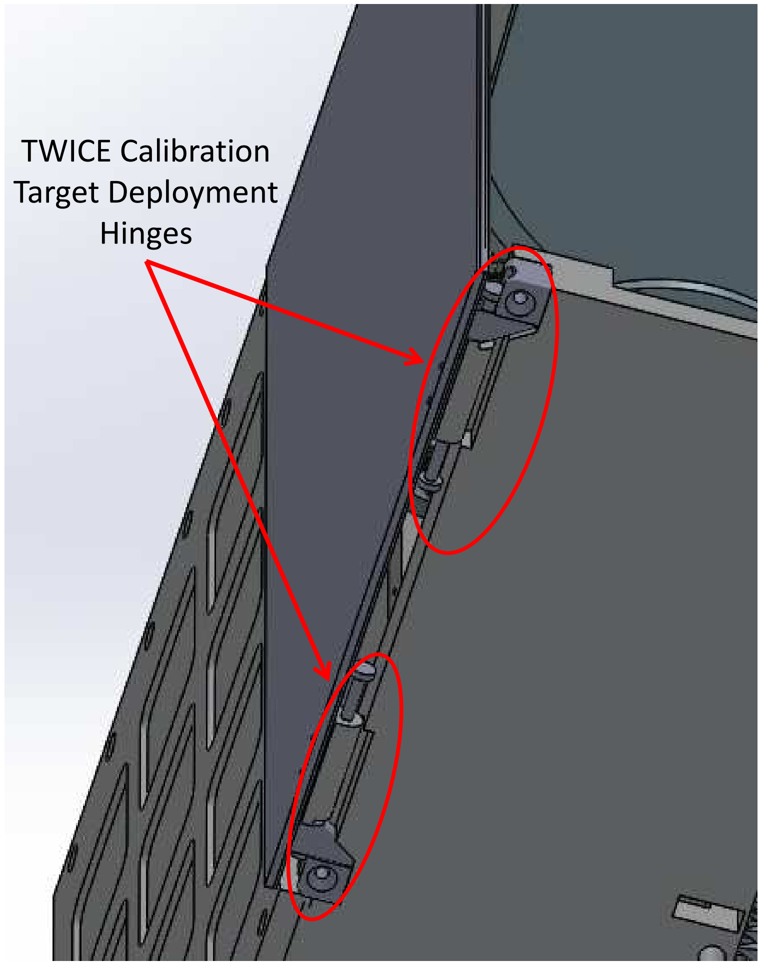

Figure 62: The hinges used to perform deployment of the TWICE calibration targets.

6.10 CMB Calibration Error Correction

The CMB generally provides a uniform source of radiation at a known temperature for which radiometers well within the microwave frequency range can use to characterize their unique radiometer transfer equation. However, upon increasing the frequency of the radiometer into the millimeter- and sub-millimeter-wave region, like that of TWICE, the use of the CMB as a cold reference point for calibration becomes trickier. Approximations that are made with microwave radiometers tend to break down at TWICE frequencies, resulting in errors inherent in the physics of calibration itself.

The radiance that a radiometer receives is dictated by Planck's law, as previously described. Up until recently, microwave radiometers have been able to take advantage of an approximation of Planck's law that has allowed for simpler calculations. Instead of using Plank's law as is, radiometers operating at or below the millimeter-wave region can make use of an approximation known as the Rayleigh-Jeans limit. Recall Planck's law in terms of frequency shown in Equation VI.4.

$$B_\nu(\nu, T) = \frac{2h\nu^3}{c^2} \frac{1}{e^{\frac{h\nu}{k_B T}} - 1} \qquad \text{(VI.4)}$$

The Rayleigh-Jeans limit is reached at comparatively low frequencies, that is to say $h\nu \ll k_B T$. In this region Planck's law is largely linear and can be approximated by performing a Taylor expansion of the exponential term. Taking this expansion out to higher orders will allow one to approximate the shape of Plank's law, however, given the condition stated, the higher orders will tend to zero while the lower orders remain. Thus, the expansion is only carried out to the first order, seen in Equation VI.5.

$$e^{\frac{h\nu}{k_B T}} \approx 1 + \frac{h\nu}{k_B T} \qquad \text{(VI.5)}$$

Substituting this approximation into the original equation will yield Equation VI.6.

$$B_\nu(\nu, T) = \frac{2k_B \nu^2}{c^2} T \qquad \text{(VI.6)}$$

This approximation allows one to quickly make the assertion that the radiance received by a radiometer from a perfect blackbody is linearly dependent on the absolute temperature of the source. This, in turn, helps to provide the basis on which linear radiometer calibration can be approximately determined. This sort of approximation will hold true at TWICE frequencies for terrestrial temperatures, say 70 – 300 K. However, upon observing the CMB (2.7 K) this approximation cannot be used. Instead the entirety of the Planck's equation must be considered. Figure 63 shows Planck's equation and the Rayleigh-Jeans approximation as a function of temperature for two different frequencies. As previously stated, the TWICE radiometer instrument will utilize an on-board ambient calibration target and the CMB as its two calibration targets. Figure 63 mimics this strategy by placing two points of calibration at 300 K and 2.7 K. The figure identifies the point at which both the full Planck's equation and the Rayleigh-Jeans approximation produce the same radiance. Recall that a radiometer measures radiance, i.e. the output of the radiometer is directly related to radiance. Figure 63 shows that the Rayleigh-Jeans approximation can calculate the same radiance as Planck's law, however, at a distinctly different temperature. For 22 GHz, a common frequency for water vapor profiling, the difference is very small, approximately 0.6 K. For 670 GHz the difference greatly grows up to approximately 7 K. When observing the Earth's atmosphere, a difference of 7 K can create large errors and result in very unreliable data. To ensure that final data product is properly calibrated, a correction to the Rayleigh-Jeans approximation should be made.

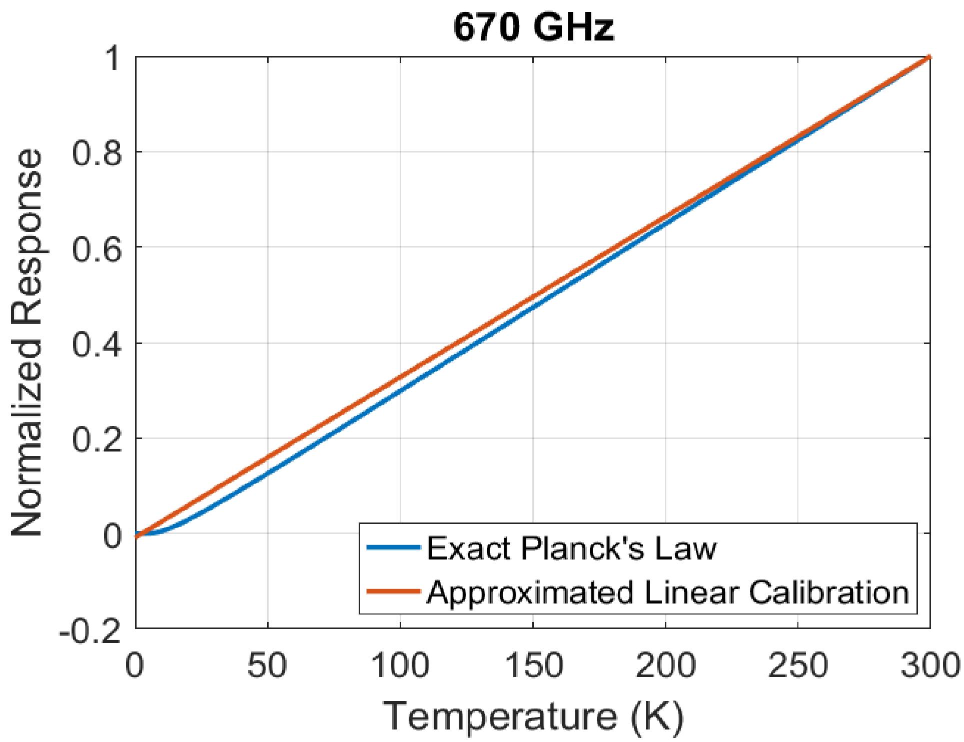

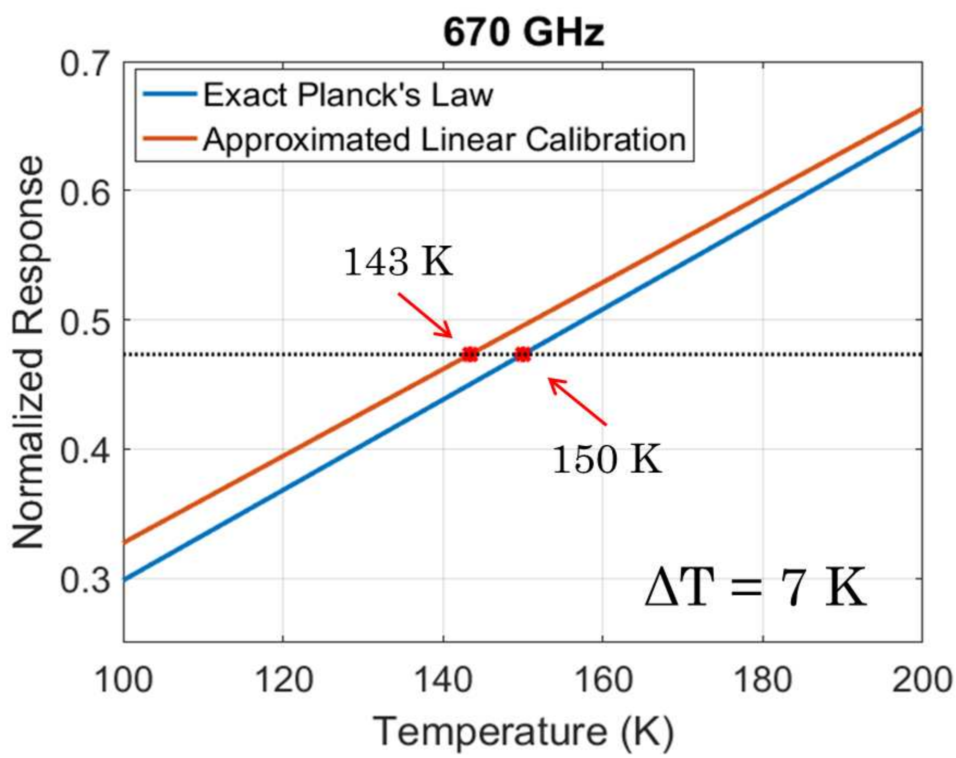

Figure 63: The strategy of utilizing the cosmic microwave background as a cold target for external calibration tends to break the Rayleigh-Jeans approximation for frequencies approaching the THz region.

The errors accrued by the Rayleigh-Jeans approximation can be accounted for by exploring the linear transfer equation used by a total power radiometer, e.g. the radiometers used on the TWICE instrument. The detectable noise power within a total power radiometer system is determined by the temperature of the noise source. The relationship between noise power and temperature naturally follows Planck's law shown in Equation VI.7 [46].

$$P_n(\nu, T) = h\nu B \frac{1}{e^{\frac{h\nu}{k_B T}} - 1} \tag{VI.7}$$

Note that all of the aforementioned variables and constants retain the same meaning and B is the bandwidth of the radiometer system. It is understood that the output of a total power radiometer is a function of the power observed by the system and the overall gain of the system. This relationship is seen in Equation VI.8.

$$V_o = G(P_A + P_R) \tag{VI.8}$$

Where V_o is the output voltage of the radiometer, G is the overall gain of the radiometer system, P_A is the power of the signal received by the radiometer antenna from the observed scene, and P_R is the power induced by the radiometer system itself. Because a total power radiometer is a linear system, as shown in Equation VI.8, plugging Equation VI.7 in for P_A will allow V_o to follow the same curve as the non-approximated Planck equation. One can then perform two-point calibration as normal.

As side note, for radiometers operating in a relatively low frequency domain, Equation VI.7 can also be approximated by way of Taylor series. This allows Equation VI.7 and Equation VI.8 to be reduced to Equation VI.9 and Equation VI.10, respectively.

$$P_n(T) = k_B T B \tag{VI.9}$$

$$V_o = G(T_B + T_R)k_B B \tag{VI.10}$$

Where T_B is the brightness temperature of the observed scene, T_R is the receiver noise temperature, and the other terms are as previously defined. Note that Equation V.10 is the equation most commonly used for the two-point calibration strategy. However, this equation will only produce valid calibration results give that the Rayleigh-Jeans limit is satisfied. Note that Equation VI.9 and VI.10 are used to determine perform all of the analysis shown in Chapter V. Another way of avoiding the errors incurred by the Rayleigh-Jeans approximation is the Janssen correction, shown in Equation VI.11 [47].

$$T_c = \frac{h\nu}{2k_B} \frac{e^{\frac{h\nu}{k_B(2.7)}} + 1}{e^{\frac{h\nu}{k_B(2.7)}} - 1} \tag{VI.11}$$

In Equation VI.11 T_c CMB temperature and all of the other variables and constants are as previously defined. The Janssen correction is a mathematical trick that adjusts the value of the CMB so that the Rayleigh-Jeans approximation can still be used. An example of this correction is seen in Figure 64. For the example of the 670 GHz radiometer, Janssen's equation gives a value of approximately 16 K as the "corrected" CMB temperature. With this corrected temperature, one can then perform a linear two-point calibration, however, when measuring the CMB one will replace the temperature of 2.7 K with corrected temperature. Ultimately, the radiometer is receiving the actual radiance from the CMB, however, that actual radiance is assigned to the corrected temperature, not to 2.7 K. By using this correction, one is still able to use the simplified version of the Planck equation while also reducing the errors produced by the approximation at higher frequencies. As a comparison, the difference between the Janssen corrected Rayleigh-Jeans approximation and Planck's equation at 670 GHz is 0.4 K, about 6.3 K less than using the Rayleigh-Jeans approximation without any corrections.

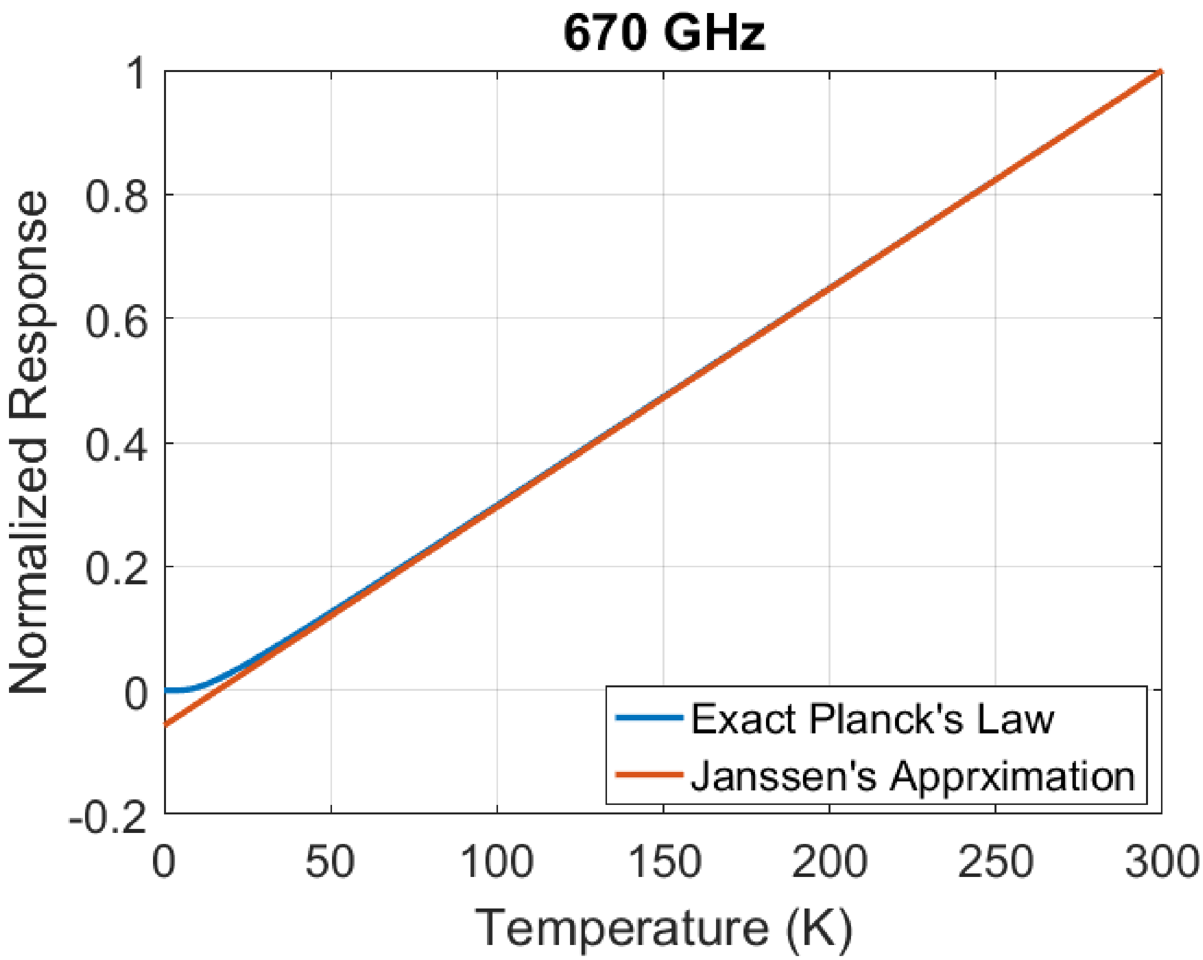

Figure 64: The Janssen correction helps to minimize temperature error when using the Rayleigh-Jeans approximation.

Chapter VII The TWICE Interface Board

7.1 Context and Purpose

The TWICE instrument is made up of several different components and systems. Namely, systems like control and data handling (C&DH), two-point calibration, instrument scanning, and on-board computer data storage require layers of intercommunication for nominal operation. For example, time stamped radiometer data from the C&DH subsystem and position data from the scanning subsystem must be combined to ensure that each pixel of data is properly assigned to a correct location along the scan [48]. Furthermore, an ADC must be able to collect thermistor data on both the moving and stationary parts of the TWICE instrument, and then transfer that data for storage in the on-board computer. In general, the interface board was designed to easily integrate each of the overlapping subsystems that make up the TWICE instrument.

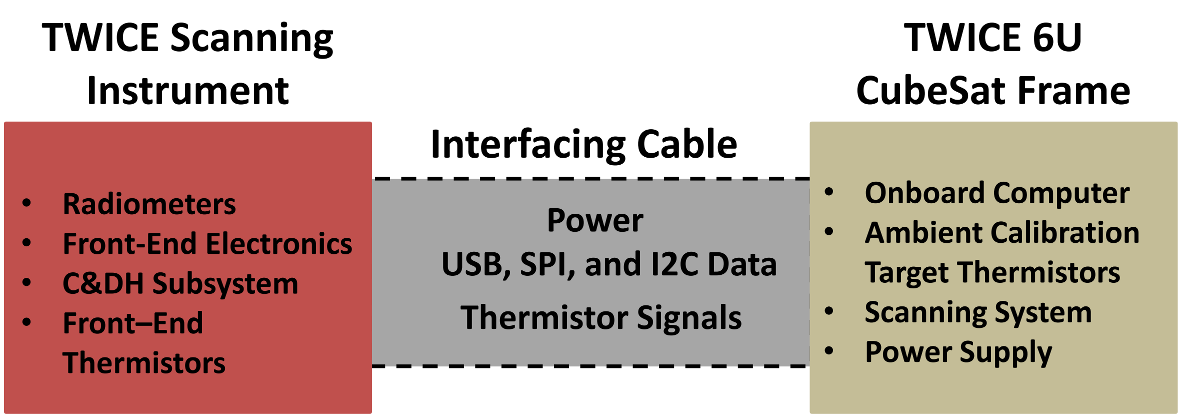

Figure 65: All of the TWICE subsystems must utilize an interfacing scheme to ensure proper communication and operation.

Consider Figure 65, which illustrates the general location and interface between each of the TWICE subsystems. Power and data storage must be provided from components within the TWICE 6U CubeSat frame, as well as the ADC. The C&DH subsystem must be able to send both SPI and USB signals to the on-board computer for storage, and the microcontroller which controls the scanning system must maintain a stream of communication with the C&DH to ensure that each radiometer pixel is correctly stamped with a known scan position.

Much of the interfacing required to operate the TWICE scanning instrument is contained within the C&DH electronics. This includes front-end electronics interfacing with the radiometers, and power regulation system. A detailed account of the design of the C&DH subsystem can be found in [49]. With the aid of a simple adapter attached to the C&DH electronics, needed data can be transferred to and from the stationary part of the TWICE instrument by way of an interfacing cable.

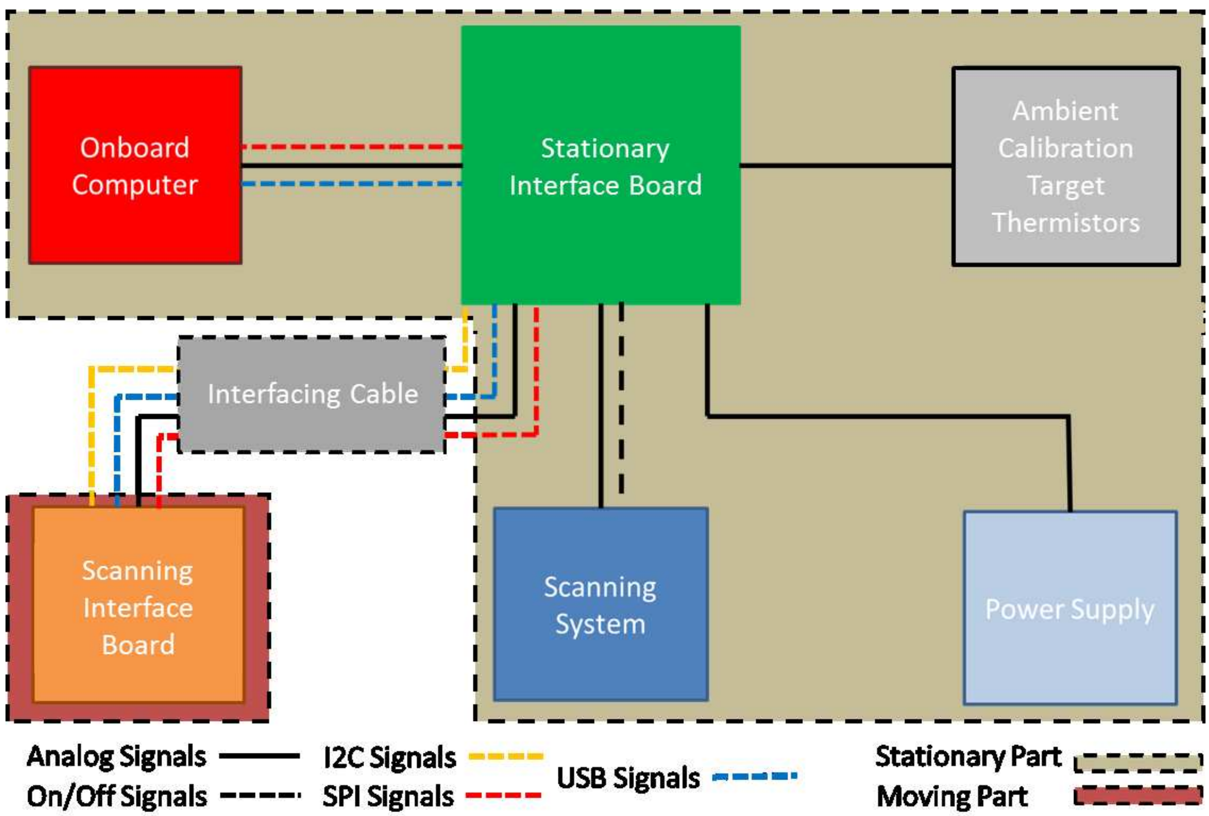

Figure 66: A simple diagram showing each of the different TWICE subsystems and how they are interfaced at the interface board.

The interface board will be responsible for routing signals, conditioning signals, power regulation, and providing a platform for the scanning system electronics and the thermistor ADC.

It will also be responsible for sending and receiving signals to and from the C&DH subsystem. A diagram of the different subsystems the interface board will be connected to is shown in Figure 66. In this figure the scanning system block encompasses the microcontroller, motor driver, position sensors, and stepper motor. It is obvious from the diagram that the interface board will need to utilize a somewhat complex mixed analog/digital circuit design.

The solid analog signal lines can represent power signals routed to the on board computer, analog thermistor signals, or driving signals sent to the stepper motor. In the context of the diagram, the on/off signals represent the signals coming from the scanning systems position sensors that produce logic high or logic low signals. With Figure 66 in mind, it is understood that the most basic components to be included on the interface board are an ADC for the thermistors in the ambient calibration target and on the scanning radiometer instrument, a microcontroller and motor driver to operate the scanning system. Cable assemblies will also be included to enable communication with the various difference subsystems shown in Figure 66.

The interfacing cable needed between the interface board and the C&DH requires an extra amount of structural integrity. With the TWICE scanning radiometer instrument completing a full scan in one direction once ever second, and with an expected operational life time on the order of a full year, the number of bends that the interfacing cable would need to endure is on the order of 30 million. This means a standard cable assembly would not suffice, and a ribbon like cable with a high bending tolerance would need to be used.

7.2 Design of the Stationary Interface Board

The TWICE interface board is designed to include as many needed components as possible while also remaining within the volume restrictions laid out by the TWICE 6U CubeSat frame. There are 5 fundamental components needed to allow proper interfacing between each of the TWICE subsystems. These include a motor driver, a microcontroller, circuitry for power regulation and signal conditioning, an ADC for thermistor acquisition, and cabling for routing signals to their intended locations.

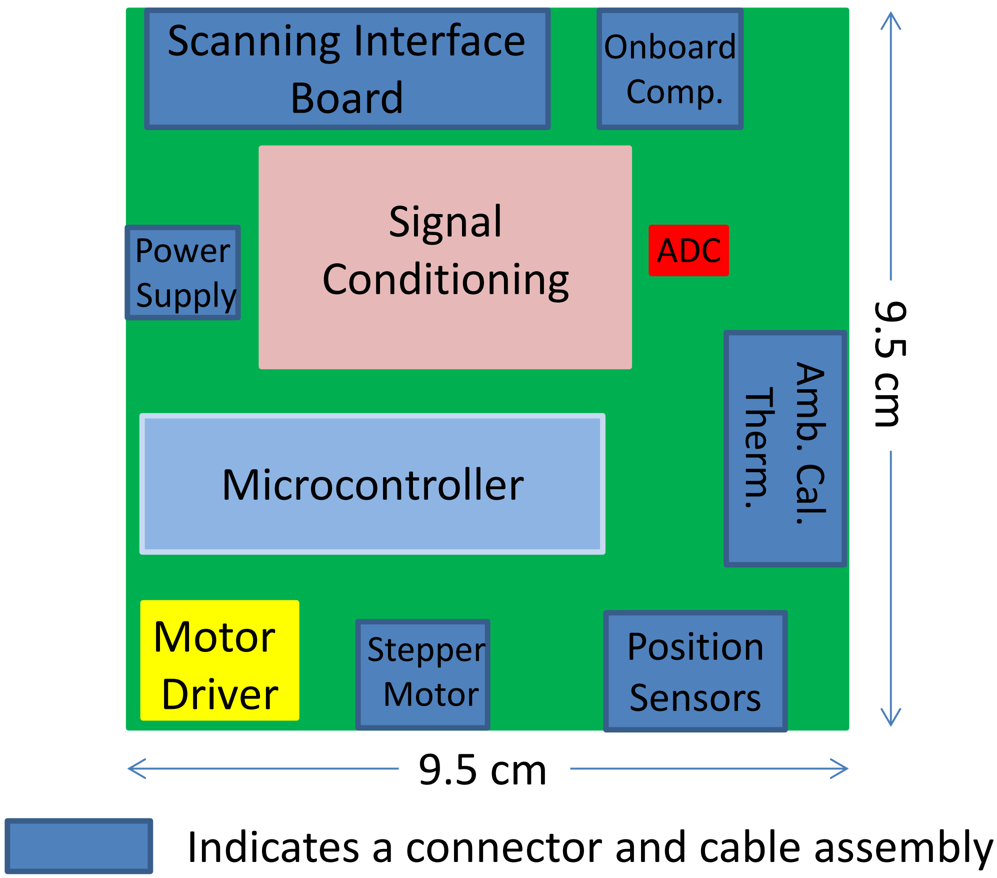

Figure 67: A simplified layout showing each of the required components for the TWICE stationary interface board.

Figure 67 shows a simple diagram of the stationary interface board. Note that in this picture, each of the component blocks are represented approximately to scale with the size of the board itself. Although the board will include a mixed analog/digital design, any sort of interference between components is not expected. It is recognized that the motor driver will produce several Watts of power at a relatively high frequency, on the order of KHz, however, given that the wavelength of any possibly interfering EM signals is much, much larger than any connecting line or component on the board, its placement can be arbitrary and EM interference can be ignored. The size of the TWICE stationary interface board was selected to meet the size restrictions of a 6U CubeSat while also providing enough space for each of the components to fit comfortably.

7.3 Selection of TWICE Stationary Interface Board Components.

As mentioned, each of the stationary interface board components has been selected with the purpose of meeting the needs of the subsystems they will interface with. That is to say, board size and spacing were only taken into consideration after all of the components were selected. This section will be divided into 5 parts, to match the 5 fundamental components needed for the stationary interface board. Each part will briefly describe the selected components used to fulfill the needs of the 5 fundamental components.

7.3.1 The TWICE Microcontroller

During discussion of the TWICE scanning system, it was determined that the TWICE stepper motor would require a microcontroller. Fundamentally, this microcontroller is responsible for controlling the movement and direction of the stepper motor during nominal operation. However, other functionalities can be included in the microcontroller design to meet the needs of other systems. For instance, the microcontroller can send microstepping commands to the motor driver, monitor the position sensor system, and even establish I2C and SPI communication with the C&DH subsystem and the on-board computer, respectively. Each of these functionalities was taken into account when selecting the Teensy 3.6 development board. This board includes a 180 MHz ARM Cortex-M4 core processor inside a MK66FX1M0VMD18 Microcontroller IC. The Teensy 3.6, shown in Figure 68, provides the capability to quickly test and program each of the TWICE subsystems that interface with the microcontroller. In addition to programmability, the Teensy is also capable of storing data via an SD card port. This provides an alternative for the collection of position data in the event that the C&DH subsystem is not able to communicate with the microcontroller. The Teesey 3.6 is compatible with both C languages and the Arduino IDE, allowing for quick debugging and programming changes [50].

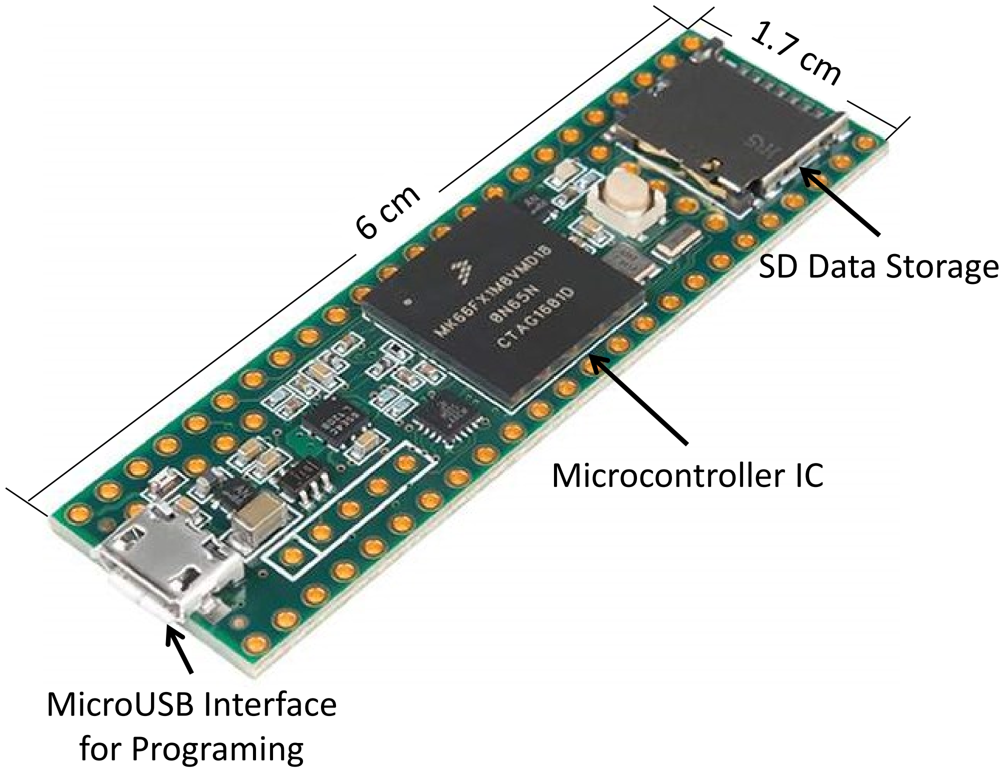

Figure 68: A picture of the Teensy microcontroller development board [51].

The schematic pinout for the Teensy 3.6 is shown in Figure 69. Pins are assigned to meet the needs of not only the stepper motor, but also to communicate with the C&DH subsystem and the on-board computer. As shown in the figure, the Teensy 3.6 operates on a 5 V power supply and can produce regulated 3.3 V outputs.

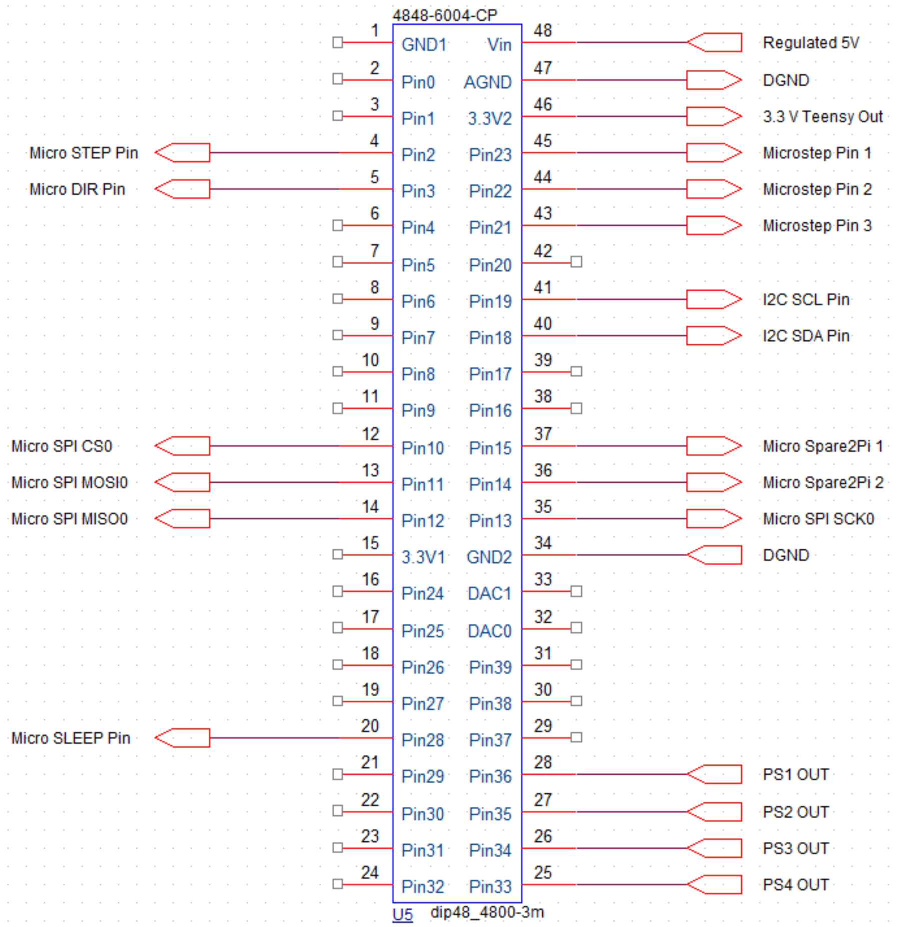

Figure 69: The schematic pinout of the Teensy 3.6 on the TWICE stationary interface board.

The 3.3 V output seen at position 46 is used to provide a digital reference to the motor driver. All of the position sensors are connected to the Teensy 3.6 where their signals will be used to correct the calculated position of the TWICE scanning radiometer instrument. Two spare pins are also included and routed to the on-board computer for extra flexibility. The Teensy 3.6 will be attached to the TWICE stationary interface board via a dip socket.

7.2.2 The TWICE Stepper Motor Driver

Working in conjunction with the microcontroller is the stepper motor driver that is used to drive the movement of the scanning system. The Pololu A4988 Stepper Motor Driver Carrier was selected for the interface board and utilizes a driver IC (A4988) integrated with a premade development board. Again, the use of a predesigned development board allows for ease of design and ensures functionality of the driver system. A picture of the Pololu A4988 is seen in Figure 70.

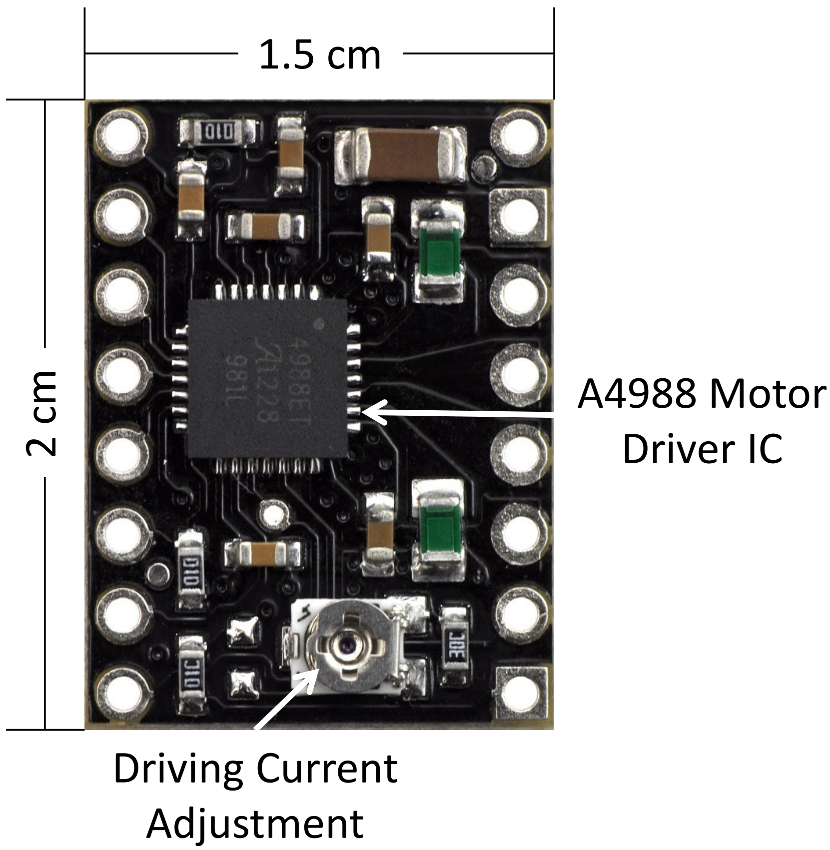

Figure 70: A picture of the Pololu A4988 motor driver development board [52].

In addition to is basic driving capabilities, the Pololu A4988 motor driver includes an adjustable current control that allows a maximum current value to be set during operation. This feature can be very useful in power saving situations where the stepper motor can be programmed for minimal power consumption. The A4988 also includes 5 different microstepping options from full stepping down to one-sixteenth step stepping. Each of the microstepping options can be controlled by sending a set of logic highs or lows to specific pins on the driver development board [53]. The microcontroller has been designed to enable the microstepping functionality. The schematic pinout of the motor driver is shown in Figure 71.

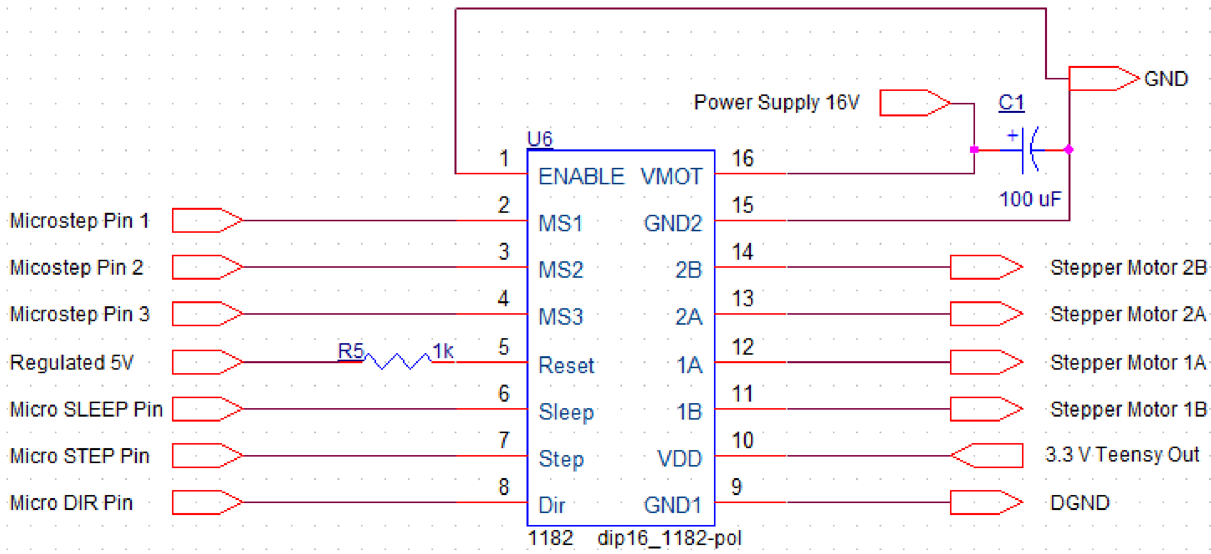

Figure 71: The schematic pinout of the Teensy 3.6 on the TWICE stationary interface board.

Note in this schematic that 3.3 V digital logic signal is provided by the Teensy 3.6 microcontroller. A the sleep pin on the motor driver is also connected to Teensy 3.6 and can be activated in the event that the motor driver, and therefore the scanning system, should be shut down.

7.2.3 The TWICE Thermistor ADC

The temperature monitoring system used with the TWICE instrument gathers temperature data of various front end systems, including radiometer receiver blocks and electronics, as well as the ambient calibration target. As seen in a previous section, it was decided that the average ambient calibration target temperature can be reliably measured using only 8 thermistors. It has been determined that temperature data of each radiometer receiver block, 4 in total, should be collected during operation.

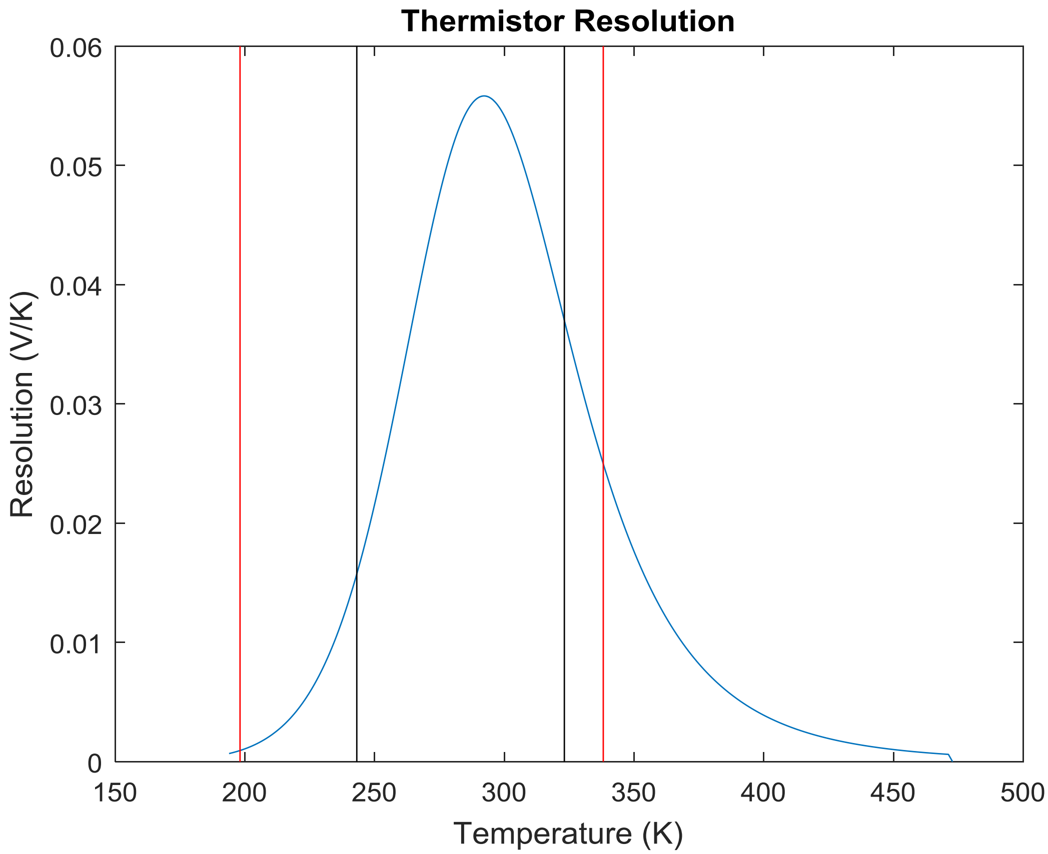

Figure 72: A plot showing the thermistor resolution over it rated operation temperature range.

In addition, 4 extra thermistors will be used to monitor temperature data of backend electronics. In total, the number of thermistors required for nominal operation of the TWICE radiometer instrument is 16. The number of needed thermistors is important when determining an appropriate ADC system to digitize and collect temperature data, for it determines the number of ADC channels and the circuitry required for operation. Lastly, minimum resolution determination must be considered, which makes the selection of an ADC more complex compared to the selection of the previous components.

Figure 72 shows a plot of the temperature resolution for the U.S. Sensor KS502J2 NTC over its operation temperature range. In Figure 72, black lines show the temperature range where the thermistor uncertainty is rated as ± 0.1 °C. Red lines show the temperature range where the thermistor uncertainty is rated as ± 1 °C. Recall that thermistors will be sending voltage signals to the ADC for digitization. Utilizing the Steinhart-Hart equation, and a voltage divider, one is able to convert voltage from the thermistor into a temperature measurement [54]. The black and red vertical lines in Figure 72 show the temperature ranges where each of the rated thermistor uncertainties lies. The smaller of the temperature ranges, black lines, represents the range where the thermistor uncertainty is rated to be ± 0.1 °C. The larger of the two temperature ranges, red lines, represents the range where the thermistor uncertainty is rated to be ± 1.0 °C. Seen in the previous chapter, it is known that the expected lower temperature limit that the ambient calibration target will experience during an airborne campaign is around -60 °C, which means that the selected ADC must have an effective temperature resolution of approximately ± 1.0 °C. The ADC used on the stationary interface board will be powered with a 5 V supply, and utilized a 5 V reference signal. This means that over a reference range of 5 V, the ADC must be able to detect a voltage difference as small as 0.001 V, where this change of voltage is equivalent to a 1 K change in temperature at this limit, shown in Figure 72. Evoking Equation VII.1 will determine the number of bits needed to achieve this resolution.

$$R_A = \frac{V_{Ref+}}{2^n R_T} \tag{VII.1}$$

Where R_A is the minimum acquired thermistor resolution, V_{Ref} is the reference voltage of the ADC, n is the number of ADC precision bits, and R_T is the thermistor resolution at a particular point within the thermistors operation temperature range. It was determined that the number of ADC precision bits required to accurately temperature data is n = 14, where R_A = 0.305 K. Appling some overhead to account for ADC processes and noise, it is determined that the minimum number of bits needed is 16.

To meet the need of the TWICE temperature monitoring system, the LTC2439-1 16-bit sigma-delta ADC was selected. The LTC2439-1 is an ultra-low power ADC which also provides the flexibility to operate either in an 8 channel differential mode or a 16 single ended mode. Communication and data transfer from the ADC is established with an SPI interface [55]. Figure 73 shows the schematic pinout of the LTC2439-1 ADC. Note that in Figure 72 the ADC is configured to operate in the 16 channel single ended mode, accommodating each of the 16 thermistors used in the TWICE temperature monitoring system. In this mode the ADC will take measurements in the order that is requested by the on-board computer. This means that care must be taken to monitor each of the thermistors in the correct order. The ADC also requires up to a few tenths of a second to take individual measurements, meaning that the acquisition code on the on-board computer must properly time measurements.

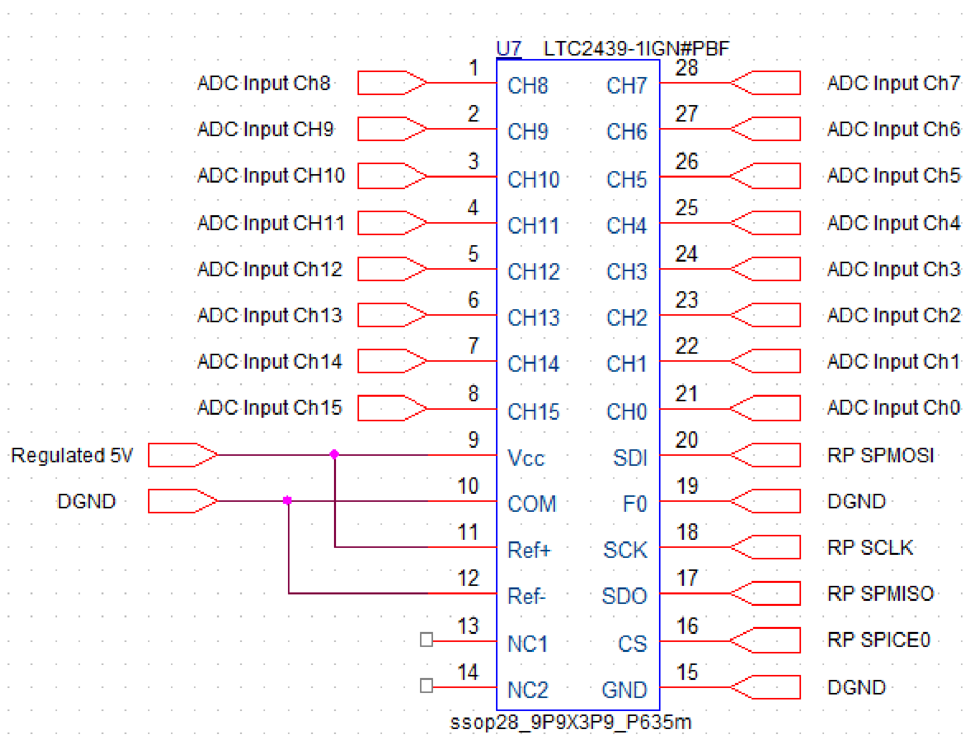

Figure 73: The schematic pinout of the LTC2439-1 ADC.

7.2.4 TWICE Interface Board Signal Conditioning and Power Regulation Subsection

The last of the major sections of the TWICE stationary interface board is the signal conditioning subsection. Each of the components used on the stationary interface board require some sort of input power, and other components require conditioned analog and digital signals to ensure nominal operation. Generally speaking, this subsection makes up all of the circuity needed to operate the interfacing components. However, for items like the ADC specific reference voltages and voltage dividers are required.

It should be noted that each of the previously discussed components utilize a regulated 5 V supply. In particular, the ADC and the microcontroller use the regulated 5 V as a power supply. The motor driver utilizes a 5 V signal to pull up its RESET pin, and receives a 3.3 V signal from the Teensy microcontroller, which is powered by the 5 V signal. In addition, the 5 V signal is routed to the on-board computer where it also provides power to the data storage subsystem, and routs power to each of the position sensors to enable motor position monitoring. The reason 5 V was selected to power so many different systems, simply has to do with the power rating of each of the aforementioned components and systems, all of which are designed to operate with a 5 V power supply.

The outlier in the chain of 5 V devices is the motor driver. As shown in Figure 71, the motor driver is actually powered by a 16 V power supply. Due to the large amount of current delivered to the stepper motor, the motor driver must utilize a relatively high power source. This power source ultimate comes from some sort of external power supply. In the case of benchtop testing, this power can come from a simple power supply box. For an aircraft campaign, the power would most likely be provided from the aircraft. Ultimately, needing a 16 V power supply means that the 5 V tolerant components and subsystem need some sort of power regulation.

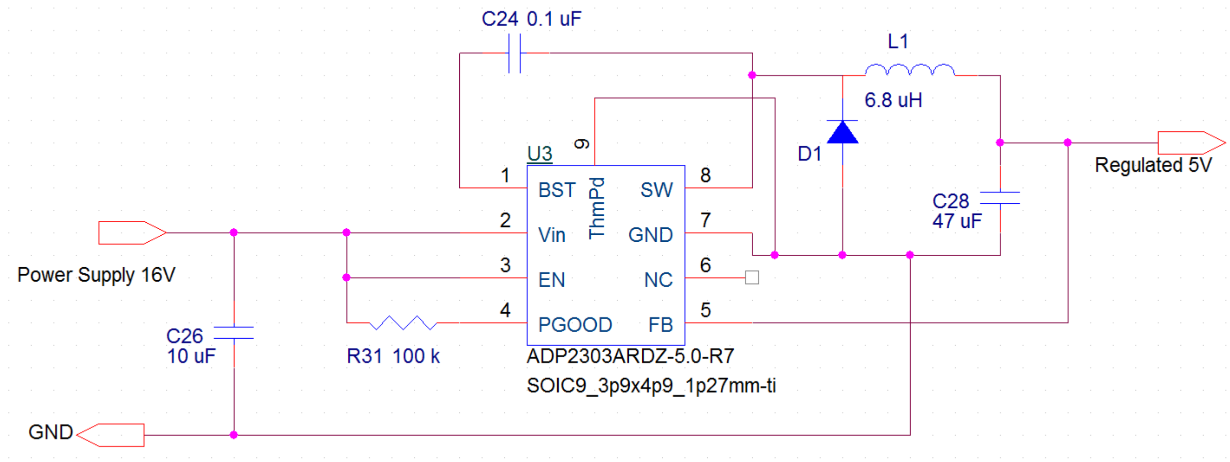

Figure 74: The schematic pinout of the Analog Devices ADP2303ARDZ-5.0 voltage regulation IC.

The Analog Devices ADP2303ARDZ-5.0 power regulation IC was selected to provide a 5 V regulated power supply to each of the required components and subsystems. The 5 V regular operates on a 700 kHz switching frequency and can provide up to 3 A of output current [56]. The schematic pinout of the 5 V regulator is shown in Figure 74. Note that the IC is powered by the external 16 V power supply.

As previously mentioned, the 5 V regulator also provides power to the scanning systems position sensors. These sensors, connected to the interface board with a cable assembly, are powered on by the regulated voltage signal, and produce logic high or logic low signals when sitting idle or when tripped. These signals are then transferred to the Teensy 3.6 micro controller, where the motor stepping calculation is corrected.

Nominal operation of the TWICE temperature monitoring system requires the use of voltage dividers. The ADC does not have the capability to directly digitize anything other than a voltage signal, meaning that in order to collect temperature data, a voltage divider must be used in conjunction with each of the 16 thermistors. At the same time, the ADC has a positive saturation voltage limit for data digitization at $\frac{V_{Ref+}}{2}$. Recall that V_{Ref+} is supplied by the 5 V voltage regulator shown in Figure 74. As a result, the maximum amount of voltage that can be digitized by the ADC on any given channel is only 2.5 V.

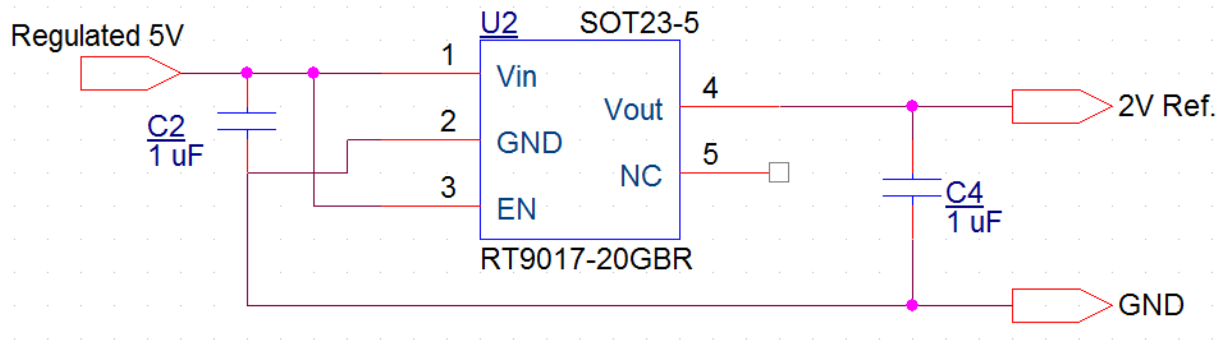

Figure 75: The schematic pinout of the Richtek RT9017 voltage regulation IC.

Note that the thermistors used in the TWICE system increase their resistance, and therefore voltage, as the ambient temperature becomes colder. For very cold environments, like at the altitude of an ER-2 aircraft, the ADC digitization can become saturated. This phenomenon is seen during the thermal cycling test of the prototype ambient calibration target, shown in Figure 58. To mitigate this issue, a 2 V regulator was added to the stationary interface board. The pinout schematic is shown in Figure 75.

The Richtek RT9017 voltage regulator was chosen to provide the driving voltage to each of the thermistor voltage dividers. Using the 2 V regulator limits the maximum voltage experienced across any one thermistor to only 2 V, well below the ADC positive saturation limit. As shown in Figure 75, the 2 V regulator is powered by the 5 V regulator. A schematic of a single thermistor voltage divider is shown in Figure 76. Note that the divider makes use of capacitor to ensure that there is no pickup from the thermistor connections.

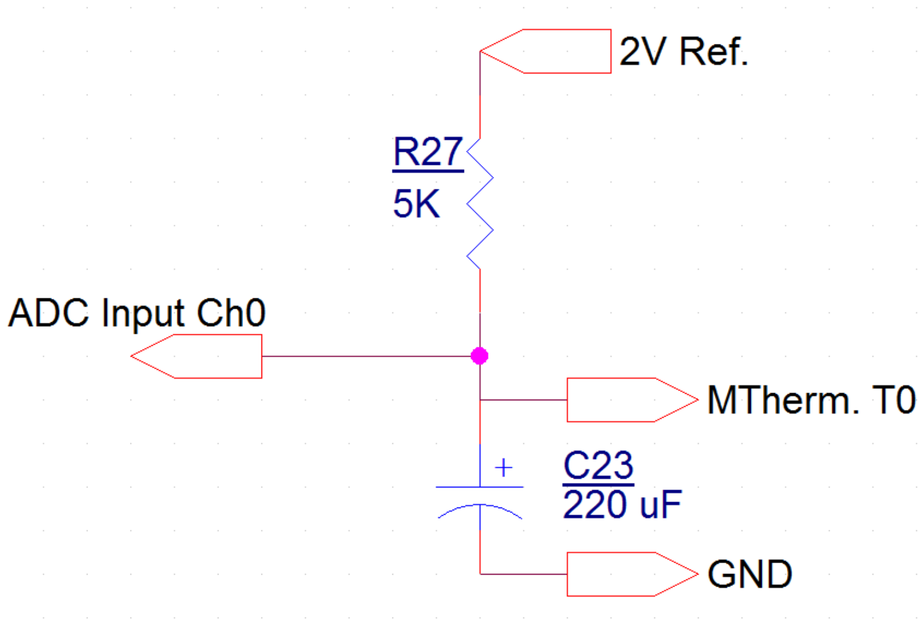

Figure 76: The schematic of a single voltage divider used for thermistor data acquisition.

7.2.5 TWICE Interface Board Cabling Assemblies

The TWICE interface board utilizes six different cabling assemblies. Each of the assemblies either routs power to its respective subsystem, or routs signals needed for nominal operation. The most important assembly is the power assembly, for it provides power not only to the interface board, but to the C&DH and on-board computer subsystems as well. The power cable assembly is simply made up of a 2 pin connector, one for a 16 V DC signal and the other for ground, both of which are tied to the external power supply. Aside from the power connector, the other cabling assemblies include the C&DH and on-board computer subsystems, the stepper motor and position sensor subsystems, and the thermistors in the ambient calibration target.

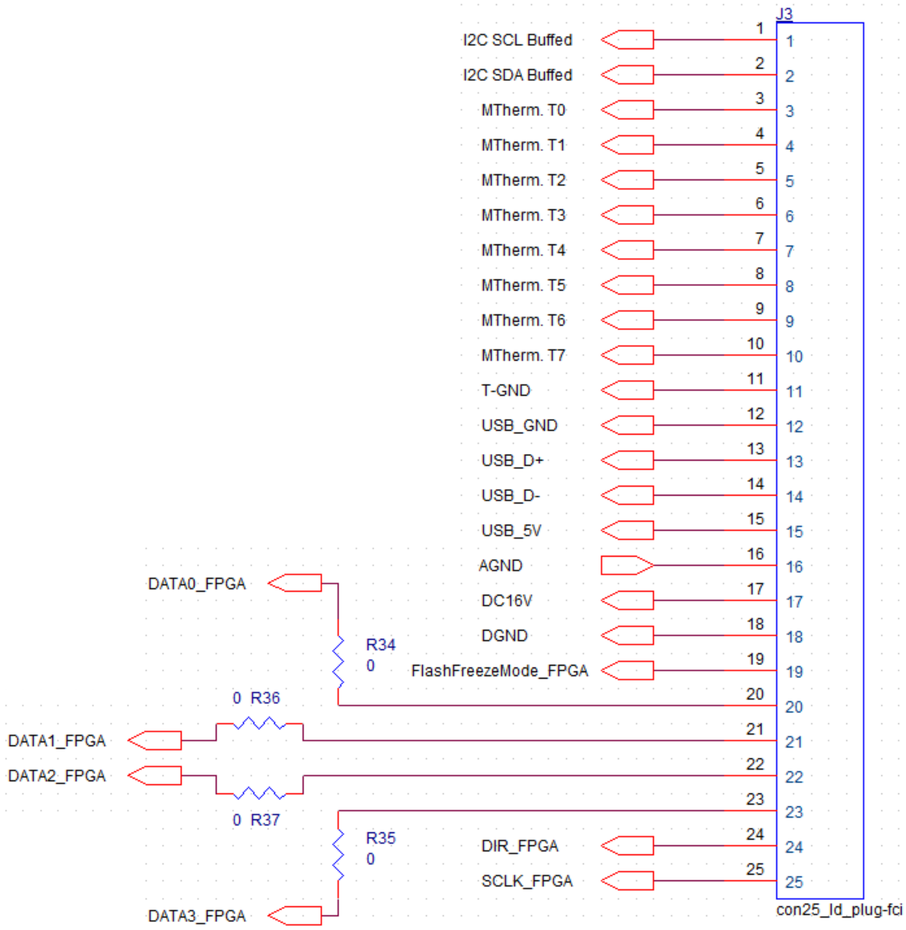

Figure 77: The schematic pinout of the C&DH cabling assembly.

The schematic pinout of the Amphenol ICC D25P24A4GV00LF D-Sub C&DH cabling assembly is shown in Figure 77. Seen in the figure is the 16 V DC power signal and ground routed from the external power supply. Included in the figure are pins for the eight thermistors used on the scanning radiometer instrument, pins for I2C communication with the microcontroller, and pins for four SPI data lines. The radiometer SPI data will be transferred to a FTDI SPI-USB conversion IC, which will be connected to the on-board computer by way of the USB pins shown in the figure.

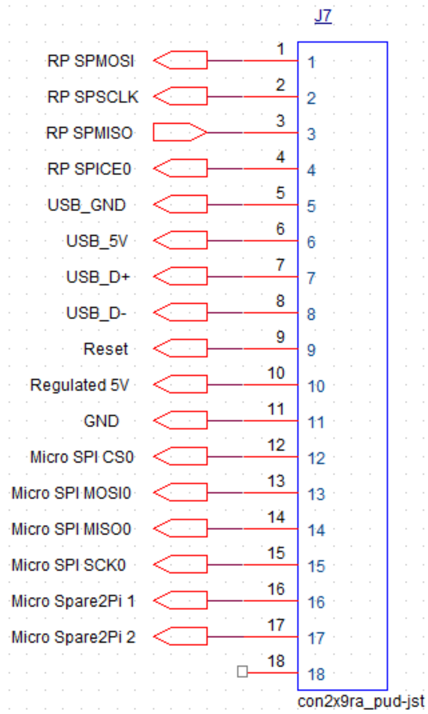

Figure 78: The schematic pinout of the on-board computer cabling assembly.

The on-board computer cabling assembly includes a 5 V input and ground pins from the 5 V power regulator and pins for SPI communication with the thermistor ADC and the microcontroller. This cabling assembly will ensure communication between each of the active parts on the interface board, the C&DH subsystem, and the on-board computer. The schematic pinout of the JST Sales America S18-PUDSS-1(LF)(SN) cabling assembly for the on-board computer is shown in Figure 78.

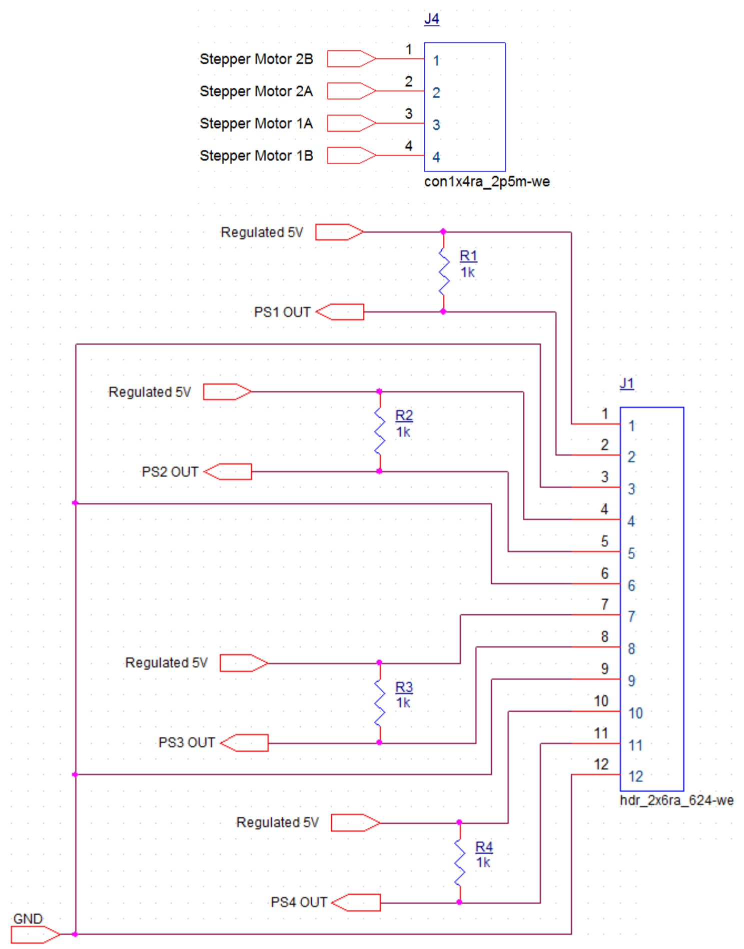

Figure 79: The schematic pinout of the stepper motor and position system cabling assembly.

Note that the same USB pins on the C&DH cabling assembly are also present on the on-board computer cabling assembly. There are also two spare pins included on this assemble, two connected directly to microcontroller and one left floating. These extra pins are included to add extra flexibility to the interface board.

The cabling assemblies used for the stepper motor and position sensor subsystems are shown in Figure 79. As seen in the figure the position sensors are also powered by the 5 V regulator. Each of the position sensors will then send their on/off signals to the microcontroller where that data will be used to correct the calculated stepper motor positon.

Last is the cabling assembly for the thermistors used in the ambient calibration target. This cabling assembly will need to be particularly long considering that it must reach to the exterior of the 6U CubeSat chassis. There is also a need for some flexibility when deploying the cabling assembly for the calibration target's thermistors. As the target moves from a stored positon to a deployed position, or from stored to deployed, the cabling assembly which interfaces its embedded thermistors will need to adjust with the movement of the target. This assembly is shown in Figure 80.

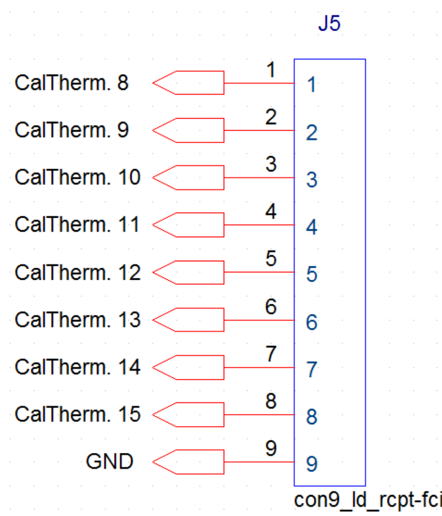

Figure 80: Cabling assembly for ambient calibration target thermistors.

7.3 Manufactured Interface Board and Resolved Issues

After the schematic design of the interface boards was completed, an outside company was hired to design the layout of and manufacture the board. The company, Digital Group Circuit Design (DGCD), located in Fort Collins, CO, produced the final interface board shown in Figure 81. The final product shown in Figure 81 required a few small fixes before the board became fully functional. For instance, the link for the SPI clock from the thermistor ADC to the on-board computer cable assembly was not created in board originally received from DGCD. This error was caused in the schematic design process where a label connecting the two pins was misspelled. As a result, the manufacturing process missed this link. This was easily fixed by simply soldering a small wire between the SPI clock pin on the ADC and its accompanying pin the on on-board computer cable assembly.

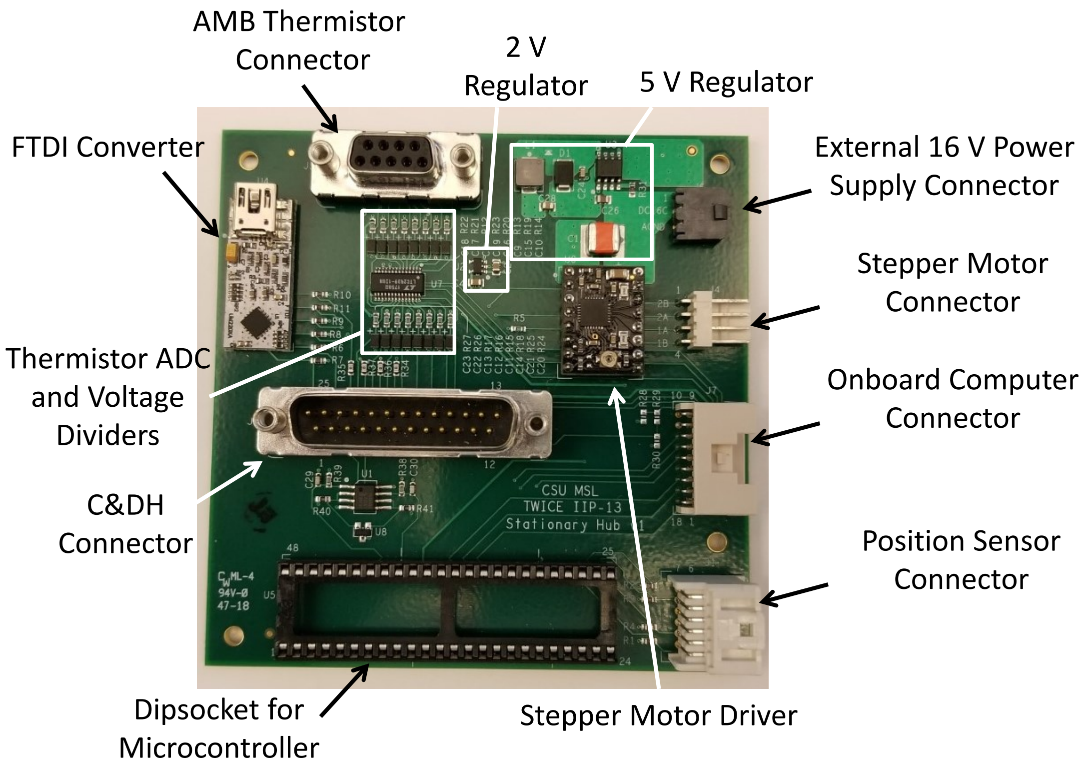

Figure 81: The final TWICE interface board.

Another error was due to the motor driver being placed upside down from its intended orientation. This caused the motor driver to be incorrectly powered and burned the drivers as a result. Once this error was identified, DGCD replaced the each of the motor drivers and placed them in their intended orientation shown in Figure 81. After these errors were fixed, each of the interface board's systems was individually tested. Each test was shown to be successful allowing for a successful communication between each of the intended subsystems.

Chapter VIII Conclusions and Future Work

8.1 Conclusions

High-altitude ice clouds, covering more than 50% of the Earth's surface, are often produced from deep convection events that strongly affect Earth's weather and climate. They play a significant role in Earth's energy balance and hydrologic cycle through their radiative feedback and precipitation effects, and therefore are crucial for life on Earth. However, our knowledge of ice cloud particle sizes is currently limited. No global satellite measurements of ice particle size in weather systems are available to observe variations in terms of season or climate environment. However, measurements at the MSMW band, from approximately 200 GHz to 900 GHz, provide sensitivity to cloud ice particles in the range of a few tens to hundreds of micrometers.

CubeSats provide platforms for the proliferation of miniaturized radiometer technology and allow opportunity to provide spaceborne observations of the Earth's atmosphere at drastically lower costs and timelines than traditional missions. The Tropospheric Water and Cloud ICE (TWICE) 6U CubeSat radiometer instrument utilizes recent technological advances to develop direct detection radiometer technology for millimeter and sub-millimeter ice particle sizing. The TWICE instrument is being developed through a collaboration led by Colorado State University in partnership with the NASA/Caltech Jet Propulsion Laboratory and Northrop Grumman Corporation. TWICE is designed to provide global measurements of ice particle size based on radiometric measurements performed at 240 GHz, 310 GHz, 670 GHz, and 850 GHz, as well as provide temperature and humidity profiles using 118 GHz, 183 GHz, and 380 GHz sounding channels.

TWICE is designed to operate with an oscillatory, conical scanning strategy. A scanning mechanism was designed and assembled that meets the inertial requirements of the scanning system and allow for contiguous footprint coverage. To meet constraints of a 6U CubeSat, a stepper motor, in conjunction with specifically placed position sensors was used instead of a traditional encoder to provide angular position data of the TWICE scanning instrument.

Proper calibration of the TWICE radiometers is vital for taking accurate measurements of an observed scene. The TWICE radiometer instrument performs end to end, two point calibration that references a “hot” and “cold” at every one second interval. The “hot” load is an ambient calibration target, which is designed to provide no less than – 25 dB of return loss at all TWICE frequencies. The material used for the TWICE ambient calibration target maintains small vertical and horizontal temperature gradients for ambient conditions. A temperature monitoring system is used within the ambient calibration target to accurately map thermal gradients and determine the radiation characteristics of the target. The temperature monitoring system is made up of eight thermistors embedded in the base of the target. The thermistors have been placed to allow for increased temperature gradient resolution in areas where the most power is received by the TWICE radiometers. Experiments and simulations have shown that for atmospheric conditions the temperature of the pyramidal surface of the ambient calibration target is predictable to within a degree of the average temperature of the embedded thermistors. The “cold” target is a CMB reflector that is designed to reflect energy radiated at approximately 2.7 K directly into the TWICE radiometers. The CMB reflector is made of a coated thin metallic sheet that can prevent corrosion and maintain reflectivity.

Finally, an interface board was designed to integrate the different subsystems that make up the TWICE radiometer instrument. Aside from the radiometers and the C&DH subsystem, the

TWICE instruments consists of several different systems to achieve nominal operation. Systems like temperature acquisition, on board data storage, and instrument scanning all must be operated synchronously to allow for proper data acquisition. The TWICE interface board integrates all of the previous systems as well as provides power to the entire radiometer instrument.

8.2 Future Work

Each of the developed systems presented in this work still need to be integrated with the TWICE radiometer instrument. This includes integration of the scanning system with the front end radiometers and the frame on which they are mounted. The ambient calibration target and CMB reflector will be mounted to the bottom panel of the TWICE 6U CubeSat chassis where the stored and deployed configurations will be tested. Work is ongoing to integrate and test the interface board with the C&DH electronics. Upon its full integration the TWICE instrument will undergo benchtop testing in a laboratory environment.

Furthermore, an aircraft campaign can be performed for the TWICE instrument and its subsystems. An aircraft campaign on a high altitude aircraft, like the ER-2, will allow the TWICE radiometer instrument to make observations of the Earth’s atmosphere. Data analysis of the observations can then be performed. Before an aircraft campaign can be performed, a modified, two point calibration systems must be designed to operate without the use of a CMB reflector.

Further testing of components designed for use during a spaceborne mission, e.g. the scanning system and ambient calibration target, can be carried out. Slight modifications can be made to both the scanning system and calibration target, e.g. replacing position sensors with space grade sensors or injection molding of the ambient calibration target materials, to allow for environmental TVAC testing. Once fully integrated, vibration testing can be performed to determine the structural integrity of the TWICE 6U CubeSat for either an airborne campaign or spaceborne mission.

Bibliography

[1] S. C. Reising, P. Kangaslahti, J. Jiang, E. Schlecht, M. Ogut , X. Bosch-Lluis, Y. Goncharenko, B. Kilmer, R. Cofield, Chahat, N. Chahat, S. T. Brown, W. Deal, A. Zamora, K. Leong, S. Shih and G. Mei, "Tropospheric Water and Cloud Ice (TWICE) Millimeter and Sub-millimeter Wavelength Radiometer for 6U-Class Satellites: Enabling Global Observations of Ice Cloud Particle Size and Humidity in the Upper Troposphere/Lower Stratosphere," in *2nd URSI Atlantic Radio Science Conference* , Gran Canaria, Spain, 2018.

[2] J. Wang, A. Dai and C. Mears, "Global Water Vapor Trend from 1988 to 2011 and Its Diurnal Asymmetry," *Journal of Climate,* vol. 5222, p. 5205, July 2016.

[3] Y. Hong, G. Liu and J.-L. F. Li, "Assessing the Radiative Effects of Global Ice Clouds Based on CloudSat," *Journal of Climate,* pp. 7651-7674, November 2016.

[4] J. H. Jiang, Q. Yue, H. Su, S. C. Reising, P. P. Kangaslahti, W. R. Deal, E. T. Schlecht, L. Wu and K. F. Evans, "A Simulation of Ice Cloud Particle Size, Humidity, and Temperature Measurements fro the TWICE CubeSat," *Earth and Space Science,* vol. 4, pp. 574-587, 2017.

[5] G. Chattopadhyay, "Technology, Capabilities, and Performance of Low Power Terahertz Sources," *IEEE TRANSACTIONS ON TERAHERTZ SCIENCE AND TECHNOLOGY,* vol. 1, pp. 33-53, September 2011.

[6] A. Zamora, K. M. K. H. Leong, G. Mei, M. Lange, W. Yoshida, K. T. Nguyen, B. S. Gorospe and W. R. Deal, "A High Efficiency 670 GHz x36 InP HEMT," in *2017 IEEE*

MTT-S International Microwave Symposium (IMS), Honololu, HI, USA, 2017.

[7] W. R. Deal, K. Leong, A. Zamora, W. Yoshida, M. Lange, B. Gorospe, K. Nguyen and G. X. B. Mei, "A Low-Power 670-GhZ InP HEMT Receiver," *IEEE Transactions on Terahertz Science and Technology,* vol. 6, no. 6, pp. 862-864, 2016.

[8] National Aeronautics and Space Administration, CubeSat 101: Basic Concepts and Processes for First-Time CubeSat Developers, 2017.

[9] M. Swartwout, "The First One Hundred CubeSats: A Statistical Look," *Journal of Small Satellites,* vol. 2, no. 2, pp. 213-233, 2013.

[10] J. Puig-Suari, C. Turner and R. J. Twiggs, "CubeSat: The Development and Launch Support Infrastructure for Eighteen Different Satellite," in *15TH Annual/USU Conference on Small Satellites*, Logan, Utah, US, 2001.

[11] Blue Canyon Technologies, "XB3 Spacecraft," 2017. [Online]. Available: http://bluecanyontech.com/xb3-spacecraft/. [Accessed 19 February 2019].

[12] S. C. Reising, T. C. Gaier, C. D. Kummerow, S. Padmanabhan, B. H. Lim, C. Heneghan, V. Chandrasekar, W. Berg, S. T. Brown, R. Schulte, J. Carvo and M. Pallas, "Enabling Time-Resolved Observations of Clouds and Precipitation on a Global Basis: Temporal Experiment for Storms and Tropical Systems Technology Demonstration (TEMPEST-D) Mission," in *CubeSat-Enabled Science and Engineering at the National Science Foundation*, Washington, DC, USA, 2017.

[13] S. Spremo, "EcAMSat Spacecraft Mission: The Success Story of NASA's First 6U

CubeSat," in *15th Anuual Cubesat Developers Workshop*, San Luis Obispo, CA, 2018.

[14] NanoRacks, July 2018. [Online]. Available: http://nanoracks.com/14th-cubesat-deployment-from-iss/.

[15] "CubeRRT: The CubeSat Radiometer Radiometer Radio Frequency Interference Technology Validation Mission," The Ohio State University, 16 July 2018. [Online]. Available: https://u.osu.edu/cuberrt/. [Accessed 2 April 2019].

[16] S. C. Reising, P. Kangaslahti, E. Schlect, J. Jiang, X. Bosch-Lluis, M. Ogut, Y. Goncharenko, S. Padmanabhan, R. Cofield, N. Chahat, S. T. Brown, W. Deal, A. Zamora, K. Leong, S. Shih and G. Mei, "Tropospheric Water and Cloud ICE (TWICE) Millimeter and Submillimeter-wave Radiometer Instrument for 6U-Class Nanosatellites," in *41st International Conference on Infrared, Millimeter, and Terahertz waves (IRMMW-THz)*, Copenhagen, Denmark, 2016.

[17] H. Zhu and P. Blackborow, "Understanding Radiance (Brightness), Irradiance and Radiant Flux," Woburn, MA, 2011.

[18] M. Planck, "On the Theory of the Energy Distribution Law of the Normal Spectrum," *Negotiations of the German Physical Society,* vol. 2, pp. 1-8, 1900.

[19] R. Bennartz, "Weighting Functions and Atmospheric Soundings: Part I," September 2011. [Online]. Available: https://www.eumetsat.int/website/home/Data/Training/TrainingLibrary/DAT_2042679.html .

[20] G. A. Siles, J. M. Riera and P. Garcia-del-Pino, "Atmospheric Attenuation in Wireless Communication Systems at Millimeter and THz Frequencies [Wireless Corner]," *IEEE Antennas and Propagation Magazine,* vol. 57, pp. 41-68, 2015.

[21] C. D. Kummerow, "AT622 Section 14: Particle Scattering," Fort Collins, CO, 2016.

[22] J. A. Dutton, "6.12 What about Scattering?," [Online]. Available: https://www.e-education.psu.edu/meteo300/node/785. [Accessed 19 March 2019].

[23] L. Lelli, "Aerosol and Clouds WS2014," Bremen, Germany, 2014.

[24] G. Bothun, University of Oregon, [Online]. Available: http://homework.uoregon.edu/pub/class/atm/scatter.html. [Accessed 2 April 2019].

[25] W. M. O. Secretariat, "Updating the Guide on Instruments and Methods of Observations Part IV: Satellite Observations," in *Guide on Instruments and Methods of Observations, Part IV: Satellite Observations*, Geneva, 2012.

[26] S. Derammelaere, M. Haemers, J. De Viaene, F. Verbelen and K. Stockman, "A quantitative comparison between BLDC, PMSM, Brushed DC and Stepping Motor Technologies," in *2016 19th International Conference on Electrical Machines and Systems (ICEMS)*, Chiba, Japan, 2016.

[27] S. Murugesan, "An Overview of Electric Motors for Space Applications," *IEEE Transactions on Industrial Electronics and Control Instrumentation,* Vols. IECI-28, no. 4, pp. 260-265, 1981.

[28] M. Grant, "Quick Start for Beginners to Drive a Stepper Motor," Freescale Semiconductor,

Chandler, AZ, 2005.

[29] P. Millett, "Improving Current Control for Better Stepper Motor Motion Quality," eeNews Analog, 22 February 2016. [Online]. Available: https://www.eenewsanalog.com/content/improving-current-control-better-stepper-motor-motion-quality. [Accessed 29 January 2019].

[30] Lin Engineering, "3709 Series," Lin Engineering, 2019. [Online]. Available: https://www.linengineering.com/products/stepper-motors/3709-series/#fndtn-standard_motor. [Accessed 29 January 2019].

[31] Harmonic Drive, "Harmonic Drive: Strain Wave Principle," Harmonic Drive, 2018. [Online]. Available: http://www.harmonicdrive.net/technology. [Accessed 29 January 2019].

[32] S. C. Reising, X. Bosch-Lluis, K. Ng, V. D. Hadel, T. P. Johnson, S. P. Nelson, K. L. Gilliam, S. Sahoo, P. Kangaslahti, S. T. Brown, A. B. Tanner, S. Padmanabhan, C. Parashare, O. Montes, D. E. Dawson, T. C. Gaier, S. J. Dinardo and B. Razavi, "Development of an Internally-Calibrated Wide-Band Airborne Microwave Radiometer to Provide High-Resolution Wet-Tropospheric Path Delay Measurements for SWOT," Fort Collins, CO, 2015.

[33] N. Skou and D. Le Vine, "Radiometer Pinciples," in *Microwave Radiometer Systems: Design and Analysis*, Norwood, Artech House, Inc., 2006, pp. 13-23.

[34] K. Gaylor, "Radar Absorbing Materials - Mechanisms and Materials," Maribyrnong, Victoria, Australia, 1989.

[35] Emerson & Cuming Microwave Products, "Theory and Application of RF/Microwave Absorbers".

[36] T. Johnson, "INTEGRATION, CHARACTERIZATION, AND CALIBRATION OF THE HIGH-FREQUENCY AIRBORNE MICROWAVE AND MILLIMETER-WAVE RADIOMETER (HAMMR) INSTRUMENT," Fort Collins, CO, 2014.

[37] C. L. Holloway and E. F. Kuester, "A Low-Frequency Model for Wedge or Pyramid Absorber Arrays-II: Computer and Measured Results," *IEEE TRANSACTIONS ON ELECTROMAGNETIC COMPATIBILITY,* vol. 36, no. 4, pp. 307-313, 1994.

[38] Laird, 2015. [Online]. Available: http://www.eccosorb.com/Collateral/Documents/English-US/RFP-DS-BSR%20093015.pdf.

[39] *Meeting with Richard Wylde.* [Interview]. 2017.

[40] University of Massachusetts Lowell, "FIRAM & TERASORB Absorbing Materials from the Submillimeter-Wave Technology Laboratory (STL)," Lowell, MA, 2011.

[41] National Aeronautics and Space Administration, "NASA Armstrong Fact Sheet: ER-2 High-Altitude Airborne Science Aircraft," 17 September 2014. [Online]. Available: https://www.nasa.gov/centers/armstrong/news/FactSheets/FS-046-DFRC.html. [Accessed 16 January 2019].

[42] National Oceanic Atmospheric Administration, "Layers of the Atmosphere," [Online]. Available: https://www.weather.gov/jetstream/layers. [Accessed 16 January 2019].

[43] D. Dankert, "U.S. Sensor Corp. NTC Thermistor P/N KS502J2," 1 May 2003. [Online].

Available:
https://www.littelfuse.com/~/media/electronics/engineering_drawings/leaded_thermistors/littelfuse_leaded_thermistors_interchangeable_thermistors_ks502j2_engineering_drawing.pdf.pdf. [Accessed 17 January 2019].

[44] W. Berg, C. Kummerow, S. Reising, V. Chandrasekar, R. Schulte, Y. Goncharenko, B. Kilmer, S. Brown, B. Lim, S. Padmanabhan and T. Gaier, "Demonstrating the Viability of the TEMPEST-D CubeSat Radiometer for Science Applications," in *International Geoscience and Remote Sensing Symposium*, Yokohama, Japan, 2019.

[45] T. Meissner, F. Wentz and D. Draper, "GMI Calibration Algorithm and Analysis Theoretical Basis Document," Remote Sensing Systems, Santa Rosa, CA, 2011.

[46] D. M. Pozar, "Active Microwave Circuits," in *Microwave Engineering*, John Wiley & Sons, Inc., 1998, pp. 547-599.

[47] M. Janssen, "Microwave Radiative Transfer Equation," in *Atmospheric Remote Sensing by Microwave Radiometry*, New York, NY, John Wiley & Sons, Inc., 1993, pp. 3-11.

[48] M. Ogut, S. C. Reising, X. Bosch-Lluis, Y. V. Goncharenko, B. Kilmer, P. Kangaslahti, E. Schlecht, R. Cofield, A. Skalare, S. Padmanabhan, J. Jiang, S. Brown, W. Deal and A. Zamora, "Design, Testing and Reliability Analysis of Command and Data Handling Subsystem for the Tropospheric Water and Cloud ICE (TWICE) Instrument for a 6U-Class Small Satellite," in *International Geoscience and Remote Sensing Symposium*, Valencia, Spain, 2018.

[49] M. Ogut, "Millimeter and Sub-Millimeter Wave Radiometers for Atmospheric Remote

Sensing from CubeSat Platforms," Colorado State University, Fort Collins, Co, 2018.

[50] Sparkfun Electronics, "Teensy 3.6 DEV-14057 ROHS," Sparkfun Electronics, Niwot, CO.

[51] S. Electronics, "Teensy 3.6," SparkFun Electronics, [Online]. Available: https://www.sparkfun.com/products/14057. [Accessed 2 April 2019].

[52] Pololu, "A4988 Stepper Motor Driver Carrier, Black Edition," Pololu, [Online]. Available: https://www.pololu.com/product/2128. [Accessed 2 April 2019].

[53] Allegro MicroSystems, "A4988 DMOS Microstepping Driver with Translator And Overcurrent Protection," Allegro MicroSystems, Worcester, MA, 2014.

[54] BetaTHERM Sensors, "NTC Thermistor Theory," Arrow Electronics, Centennial, CO.

[55] Linear Technology Corporation, "LTC2439-1 8-/16-Channel 16-Bit No Latency ΔΣ™ ADC," Linear Technology Corporation, Milpitas, CA, 2005.

[56] Analog Devices, "2 A/3 A, 20 V, 700 kHz, Nonsynchronous Step-Down Regulators ADP2302/ADP2303," Analog Devices, Norwood, MA, 2012.